UNIVERSITY OF OKLAHOMA

GRADUATE COLLEGE

NATURE AND CATALYTIC ROLE OF EXTRA-FRAMEWORK ALUMINUM AND PARTIALLY COORDINATED ALUMINUM IN MFI ZEOLITE

A DISSERTATION

SUBMITTED TO THE GRADUATE FACULTY

in partial fulfillment of the requirements for the

Degree of

DOCTOR OF PHILOSOPHY

By

VY NGUYEN
Norman, Oklahoma
2023

Downloaded from SHAREOK. Persistent Handle URL: https://hdl.handle.net/11244/337805

NATURE AND CATALYTIC ROLES OF EXTRA-FRAMEWORK ALUMINUM AND PARTIALLY

COORDINATED FRAMEWORK ALUMINUM IN MFI ZEOLITE

A DISSERATION APPROVED FOR THE
SCHOOL OF CHEMICAL, BIOLOGICAL AND MATERIALS ENGINEERING

BY THE COMMITTEE CONSISTING OF

Dr. Bin Wang, Chair

Dr. Daniel Resasco

Dr. Steven Crossley

Dr. Dimitrios Papavassiliou

Dr. Wai Tak Yip

© Copyright by VY NGUYEN 2023
All Rights Reserved.

This dissertation is dedicated to my loving parents and sister

For their endless love, support and encouragement

Acknowledgments

First and foremost, I am extremely grateful to my supervisor, Prof. Bin Wang for his invaluable advice, unwavering support, patience, and kindness during my Ph.D. study. After completing my five-year program, I have gained extensive knowledge and feel more assured in my comprehension of chemistry and theoretical calculations. Your immense knowledge and plentiful experience have encouraged me in all the time of my academic research and daily life. I am grateful to have the pleasure of working with you.

Special thanks to my committee members and professors, Dr. Daniel Resasco and Dr. Steven Crossley. Your classes and weekly catalysis group meetings have been significant sources of knowledge reinforcement and deepening throughout my research and thesis. I am grateful for the time you dedicated to questioning and supporting my research. I am also grateful to Dr. Lance Lobban for your fruitful discussions you gave me in our catalyst group meetings. Thank should also go to Dr. Jeffery White and your group for your collaboration on this project, your work not only gave me valuable ideas but also helped me to make my research more comprehensive.

Many thanks to my other committee members, Dr. Dimitrios Papavassiliou and Dr. Wai Tak Yip, for your valuable suggestions that have helped shape and guide this project.

I want to also acknowledge my funding source, the National Science Foundation under Grant Nos. CHE-1764116, CHE-1764130 and 2129982 for supporting my work, and the University of Oklahoma and OSCER supercomputer for providing me the resources to perform my calculations.

I would like to extend my appreciation to Tram Pham for providing me with an experimental perspective on my project and highlighting crucial aspects that I may have missed otherwise.

Being part of Dr. Wang's group and sharing a big office with great people has been a delightful experience. I wish to thank current and former members of the group, Dr. Tong Mou, Dr. Reda Bababrik, Yu, Isaac, Tien, Quy, Jacob, Dr. Taha Salavati-fard, Dr. Zaheer Masood and Thy for the fun times we had working and socializing together. Special thanks to Dr. Reda Bababrik, Dr. Tong Mou, and Dr. Taha Salavati-fard for their guidance and assistance from my first calculations.

Words cannot express my gratitude to my family for their unconditional love and countless sacrifices which have been instrumental in shaping who I am today. I am immensely grateful to my second family in Norman, Thao, Vi, Thy, Oanh, and Thanh who have been constantly caring, cooking for me, and cheering me in every situation, and I am forever grateful for their presence in my life.

Lastly, I would like to express my thanks to all the friends I made at OU for making the journey enjoyable and memorable.

Table of Contents

CHAPTER 1: Introduction ***1***

1.1 Theory background **1**

1.1.1 Zeolites 1

1.1.2 ZSM-5 zeolite 2

1.1.3 Distribution of aluminum in zeolites 5

1.1.4 Extra-framework aluminum (EFAL) and partially coordinated aluminum (PFAL) in zeolites. 6

1.2 Density Functional Theory (DFT) **8**

1.2.1 Hohenberg-Kohn theorems 8

1.2.2 The Kohn-Sham equation: DFT in practice 12

CHAPTER 2: Identify different protonic and aluminum species in H-ZSM5 zeolite ***15***

2.1 Abstract **15**

2.2 Introduction **16**

2.2.1 NMR Chemical Shift 20

2.3 Computational methods **21**

2.4 Results and discussions **22**

2.4.1 ^{1}H NMR and ^{27}Al NMR of isolated Brønsted acid sites at different locations 22

2.4.2 ^{1}H NMR and ^{27}Al NMR of different EFAL species stabilized at the intersection. 27

2.4.3 ^{1}H NMR and ^{27}Al NMR of synergistic site BAS/EFAL species 29

2.4.4 ^{1}H NMR and ^{27}Al NMR of synergistic site BAS/EFAL species 33

2.4 Conclusions **35**

CHAPTER 3: Dynamical behaviors of aluminum species in H-ZSM-5 zeolite ***39***

3.1 Abstract **39**

3.2 Introduction **40**

3.1.1 Nudged Elastic Band (NEB) Method 45

3.1.2 Climbing Image Nudged Elastic Band (CI-NEB) Method 48

3.1.3 Dimer method 49

3.1.4 Thermodynamic Quantities and Frequencies 50

3.1.5 Quasi-rigid rotor harmonic oscillator approximation (q-RRHO) method 53

3.3 Computational details **55**

3.4 Results and discussions **57**

3.4.1 The formation of BAS/PFAL from a site pair via incomplete hydrolysis 57

3.4.2 The formation of BAS/FAL from via migration of EFAL 60

3.4.3 Energy for sodium exchange 64

3.4.4 Interconversion of different EFAL species in ZSM-5 68

CHATER 4: Catalytic Role of EFAL and PFAL species in Alkane Reaction ***70***

4.1 Abstract **70**

4.2 Introduction **72**

4.3 Computational details **74**
4.4 Results and discussions **76**
4.4.1 Effect of EFAL and PFAL to intrinsic acid strength of ZSM-5 zeolite 76
3.4.2 Propane cracking reaction 80
3.4.3 Propane dehydrogenation reaction 95
3.4.4 Hexane cracking and dehydrogenation reactions 107
3.4.5 Acylation reaction of 2-methylfuran (2-MF) with acetic acid 113
3.5 Conclusions **115**
CHAPTER 5: Concluding Remarks and Future Work ***118***
5.1 Dissertation summary **118**
5.2 Future directions **119**
References ***121***

List of Tables

Table 1. Assignments for protonic species in H-ZSM zeolite by combining experimental spectroscopy and DFT calculations. 36
Table 2. Assignments for aluminum species in H-ZSM zeolite by combining experimental spectroscopy and DFT calculations 38
Table 3. Reaction Energies for Cation Exchange of Different Active Sites and Their Corresponding Locations. [40] 64
Table 4. The DPE values of the proposed active site in H-ZSM5 zeolite 79
Table 5. Adsorption, and activation energy of propane cracking reactions on different active sites. The calculation of energy utilized a gas phase propane reference. 83
Table 6. Charge transfers from adsorption states to zeolite framework. 84
Table 7. Charge resides on TS of propane cracking reactions on various active sites. 84
Table 8. Atomic distances of transition states on different site, with C1: terminal C, C2: middle C, H: BAS, and O: the protonated oxygen. 85
Table 9. Polarizability of propane in the gas phase and carbonium cation on different active sites. 89

Table 10. Polarizability of zeolite unit SiO_4, EFALs and PFAL species. 90
Table 11. The change of entropy along the reaction coordinate of propane cracking reactions on different active sites. 90
Table 12. Adsorption, and activation free energy of propane cracking reactions on different active sites, calculated at 773 K. The calculation of free energy utilized a gas phase propane reference. 92
Table 13. Adsorption, and activation energy of propane dehydrogenation reactions on different active sites. The calculation of energy utilized a gas phase propane reference. 95
Table 14. Charge resides on TSs of propane dehydrogenation reactions on various active sites. 97
Table 15. Polarizability of propane in the gas phase and carbonium cation on different active sites. 100
Table 16. The change of entropy along the reaction coordinate of propane cracking on different active sites. 101
Table 17. Adsorption, and activation free energy of propane dehydrogenation reactions on different active sites, calculated at 773 K. The calculation of free energy utilized a gas phase propane reference. 102
Table 18. Polarizability of hexane in the gas phase, and its TSs in cracking and dehydrogenation reactions. 110
Table 19. Estimated Activation Enthalpy and Entropy of n-hexane Cracking on Different MFI Zeolites, taking from ref. [40] 112

List of Figures

Figure 1. The configuration of four chosen zeolites along with their respective micro-pore system and measurements. [5] 2
Figure 2. Overview of H-ZSM5 at various dimensional scale. a) a micro-sized coffin-shaped H-ZSM-5 crystal. b) straight pores [001] [100] planes. c) three-dimensional channel system. d) MFI framework comprises of silica and aluminum tetrahedra. e) BAS. f) extra-framework aluminum from dealumination. g) terminal silanol group. [12] 4
Figure 3. This process allows for the iterative determination of the ground state density of a given system, by utilizing the principle outlined in the Hohenberg-Kohn theorems. 12
Figure 4. Through the use of the Kohn-Sham ansatz, it becomes possible to determine the ground state properties of a many-body system in a self-consistent manner. 14
Figure 5. A) Calculated H-ZSM5 zeolite structure; B) Schematic diagram of three-dimensional channel system of H-ZSM5 zeolite morphology comprising of the straight and the sinusoidal channel. 25
Figure 6. DFT-calculated proton and aluminum chemical shift of BAS at different locations in H-ZSM5 zeolite: a, b, c) intersection; d, e, f) straight channel; j, h i) sinusoidal channel; j, k, l) small void; m, n, o) 5-member ring (5-MR); p, q, r) 6-member-ring (6-MR). Back numbers: ^{1}H NMR, and blue numbers: ^{27}Al NMR. 26
Figure 7. Optimized structures of various EFAl species stabilized at the intersection and their DFT-calculated ^{1}H NMR and ^{2}7Al NMR. 28
Figure 8. Optimized structures of a variety of synergistic sites BAS/EFAL species stabilized at the intersection and their DFT-calculated ^{1}H NMR and ^{2}7Al NMR. In these synergistic sites, EFAL and BAS do not form hydrogen bonds. Black numbers: ^{1}H NMR and blue numbers: ^{27}Al NMR. 30
Figure 9. Optimized structures of a variety of synergistic sites BAS/EFAL species stabilized at the intersection and their DFT-calculated ^{1}H NMR and ^{2}7Al NMR. In these synergistic sites, BASs form hydrogen bonds with EFAL. Black numbers: ^{1}H NMR and blue numbers: ^{27}Al NMR. 31
Figure 10. Optimized structures of synergistic sites BAS/$Al(OH)_2^+$ and their DFT-calculated ^{1}H NMR and ^{2}7Al NMR stabilized at 8c) sinusoidal channel; 8d) straight channel. 32

Figure 11. Linear relationship between the O-H bond distance and ^{1}H NMR of proton in synergistic sites. 33
Figure 12. Optimized structures of synergistic sites BAS/PFAL species stabilized at the intersection and their DFT-calculated ^{1}H NMR and ^{2}7Al NMR. 34
Figure 13. The free energy profiles for the favored dealumination route of T3O4, T10O2, and T11O3 sites in H-MFI, which involved four water molecules and resulted in the formation of EFAL $Al(OH)_3H_2O$, were analyzed at a temperature of 450 K. The calculation of free energy utilized a physisorbed water reference. [23] 42
Figure 14 44
Figure 15. This figure from Jonsson et. al. illustrates an example NEB simulation that shows the creation of initial images (represented by a line with white circles) along a direct reaction path from the initial state to the final state, and the optimized final path (represented by a line with gray circles) passing through the MEP of that specific reaction..... 47
Figure 16. DFT calculations for model hydrolysis of (a) an Al(IV)-1/Al(IV)-1 pair, resulting in (b) an Al(IV)-1/Al(IV)-2 framework pair. Possible structures resulting from additional hydrolysis are shown in (c−e). Total energies and free energies are calculated with an ideal gas reference for water. The Al−Al internuclear distances (in Å) are shown in bold text above or below each structure, and H−H distances are shown in blue within each figure. [45] 57
Figure 17. Total energies and Gibbs free energies (gas phase water as reference) for the hydrolysis of isolated BAS at T12. [45] 58
Figure 18. DFT calculation of migration of $Al(OH)_2^+$ at the intersection. The colors blue, yallo, red, and white represent Al, Si, O, and H atoms, respectively. The energy units are given in kJ/mol. [31] 60
Figure 19. The role of BAS in stabilizing the EFAL species. 62
Figure 20. Calculated structures of Na+ titrated to (a) IBAS at the intersection, (b) IBAS in the straight channel, (c) IBAS in the sinusoidal channel, (d) BAS/EFAL at the intersection, (e) BAS/EFAL at the straight channel, and (f) BAS/EFAL in the sinusoidal channel; calculated structures of Na+ titrated to (g) paired BAS at the intersection (h) paired BAS in the straight channel and (k) paired BAS at the sinusoidal channel. Na, Al, O, Si, and H atoms are colored purple, cyan, red, yellow, and white, respectively. [40] 66

Figure 21. The optimized structures of paired BAS at a) intersection, b) straight channel, c) sinusoidal channel. [40] 67
Figure 22. Transformation of EFAL species in ZSM-5..... 68
Figure 23. Calculated structures used in polarizability calculations..... 75
Figure 24. Calculated structures of proposed active sites in H-ZSM5 zeolite..... 77
Figure 25. The numbers present the DPE of hydroxyl group in each structure..... 77
Figure 26. DPE for various possible active site in HZSM-5 zeolite..... 79
Figure 27. Enthalpy profiles of propane cracking on different active sites. 82
Figure 28. Electron density difference charge of propane at adsorption state on various active sites, the value of isosurface is 0.002 au. The blue color represents accumulation of charge and the green color represents depletion of charge. 83
Figure 29. Electron density difference charge of TS of propane cracking reactions on various active sites, the value of isosurface is 0.002 au. The blue color represents accumulation of charge and the green color represents depletion of charge. 86
Figure 30. Electrostatic interaction between carbonium C3H9+ and different EFAL and PFAL species. 88
Figure 31. Free energy profiles of propane cracking on different active sites, calculated at 773 K. 94
Figure 32. Energy profiles of propane dehydrogenation reaction on different active sites. 98
Figure 33. Density of state at the TSs of hydrogenation reactions. 99
Figure 34. Electron density difference charge of TS of propane dehydrogenation reactions on various active sites, the value of isosurface is 0.002 au. The blue color represents accumulation of charge and the green color represents depletion of charge. 100
Figure 35. Free energy profiles of propane dehydrogenation reaction on different active sites, calculated at 775 K..... 103
Figure 36. Activity per site of propane conversion in HZSM5-X zeolites, X is Si/Al ratio. 500 µl pulses of pure propane (>99%) are injected at temperature as 823 K. The BAS densities of HZSM5-15_AHFS, HZSM5-15 and HZSM5-11.5 are 0.45, 0.73 and 1.08 mmol/g, respectively. 105
Figure 37. Estimation of the order of propane cracking on HZSM5-15-AHFS. In which x is the reaction conversion, a is the mole percent of propane in the loop..... 106

Figure 38. Estimation of apparent activation enthalpy of propane reactions on MFI zeolites. .. 106
Figure 39. Reaction energy diagram of n-hexane (a) central cracking and (b) dehydrogenation of the methylene group. This figure was taken from ref. [40] 107
Figure 40. Electron density difference charge of TS of hexane cracking reactions on various active sites, the value of isosurface is 0.002 au. The blue color represents accumulation of charge and the green color represents depletion of charge. 108
Figure 41. Electron density difference charge of TS of hexane dehydrogenation reactions on various active sites, the value of isosurface is 0.002 au. The blue color represents accumulation of charge and the green color represents depletion of charge. 109
Figure 42. Determination of order of n-hexane cracking reaction, where a is the mole percent of n-hexane in the loop and X is the conversion of the reaction, taking from ref. [31] 111
Figure 43. Energy profile of acylation of 2-MF with acetic acid on BAS with the presence of EFAL $Al(OH)_2^+$ in proximity. 113
Figure 44. Energy profile of acylation of 2-MF with acetic acid on BAS with the presence of EFAL $Al(OH)^{2+}$ in proximity. The solid line represents reaction pathway 1 and dash line represents reaction pathway 2. 114

List of Schemes

Scheme 1. Mechanism of framework atoms' hydrolysis. [23] 7
Scheme 2. Conversion of different EFAL species in Faujasite zeolite. The energy is reported in kJ/mol..... 41
Scheme 3. Reaction mechanism of propane a) cracking and b) dehydrogenation of methylene group. 80
Scheme 4. Reaction pathways of acylation reaction of 2-Methylfuran with acetic acid a) on IBAS b) on BAS/$Al(OH)^{2+}$ synergistic sites..... 115

Abstract

Zeolites are extensively employed in the chemical and petroleum industries as an acid catalyst for cracking, isomerization, and alkylation reactions. Recently, they have also gained attention as potential catalysts for biomass conversion. The activity of Brønsted acid sites (BAS) contained within the microporous zeolite channels is known to be affected by the location and local environment that stabilizes reaction intermediates and transition states. Additionally, it has been reported that presence of extra-framework Al (EFAL) and partially coordinated Al (PFAL) species can significantly alter reaction rates. However, the mechanism behind these enhancements and the catalytic roles of individual EFAL and PFAL species are yet to be fully understood. In this project, we utilized Density Functional Theory (DFT) to elucidate the locations and local environments of active sites in H-ZSM-5. We also propose the mechanisms behind the synergistic effects generated by the BAS and EFAL/PFAL in proximity. Moreover, the individual catalytic effects of different EFAL and PFAL on alkane cracking reactions were investigated.

The theoretical calculations provide precise assignments of NMR spectra for acid sites and their surrounding in zeolites. The well-known signal 4.2 - 4.5 ppm is attributed from BAS at the intersection and main channels (straight and sinusoidal channels). The broad signal 5-9 ppm is assigned for framework BAS at 5-MR/6-MR or silanol groups in silanol nests for the first time. It is noteworthy that the broad signal 11-18 ppm rise from BAS forming hydrogen bonds with adjacent EFAL/PFAL species. Additionally, for different EFAL and PFAL species, the ^{27}Al NMR chemical shift values are in the broad range of 55-85 ppm, which is rational to the expansion of aluminum peak up to 85 ppm for steamed samples.

The synergistic sites are formed via the hydrolysis of Al framework atoms and migration of EFAL in the presence of water. During the initial stages of hydrolysis, incomplete hydrolysis

of BAS site pairs creates BAS/PFAL synergistic sites. The formation of synergistic sites in pulsed water treatment is not related to dealumination but rather involves the migration of EFAL to BAS to generate synergistic effect. In both propane and hexane conversions, the cracking reactions are more influenced by EFAL and PFAL species than the dehydrogenation reaction. The charge distributions reveal that EFAL and PFAL interact with transition states, resulting in lower activation barriers.

This work elucidated the underlying mechanism of EFAL and PFAL for enhancing alkane conversion and pave the way to investigate the function of broader extra-lattice species such as rare earth and phosphorous in zeolite.

CHAPTER 1: Introduction

1.1 Theory background

1.1.1 Zeolites

Zeolites are crystalline, microporous materials that possess regular pores or cavities connected through narrow channels in an ordered pattern. Zeolites are often referred to as "molecular sieves" because their pore and channel sizes (around 3-15 Å) are uniform and similar in size to small molecules such as cations, water, or appropriately sized molecules. Zeolites are composed of aluminosilicates, and their structures are based on tetrahedral silica (SiO_4) and tetrahedral aluminum (AlO_4^-), as depicted in **Figure 1**. The tetrahedrons are connected at their corners through shared oxygen atoms, forming a 3D network with different structures. To balance the charge imbalance caused by the difference in valency between Al and Si, and the number of SiO_4 and AlO_4^- present in the framework, protons, alkalis, or alkaline earth metals are filled into the lattice.

In nature, zeolites are formed when volcanic ashes interact with alkaline groundwater. Currently, there are 40 known natural zeolites that have a wide range of applications, including wastewater treatment to remove heavy metals and delivering agricultural compounds to fishponds and soil. [1] However, the inconsistent composition and impurities present in natural zeolites limit their industrial use. The first synthetic zeolite was discovered by Richard Barrer[2] in the late 1940s, and by 1953, Robert Milton[3] had successfully synthesized 20 different zeolites using different starting materials. Most of the zeolites utilized in industries are synthetic, with structures and

compositions specially designed to meet specific requirements such as catalysis, ion exchange, and separations.[4] Research into novel zeolite and synthesis methods will continue to be an essential field in the future as the demand for zeolites with precise physical and chemical properties continues to rise.

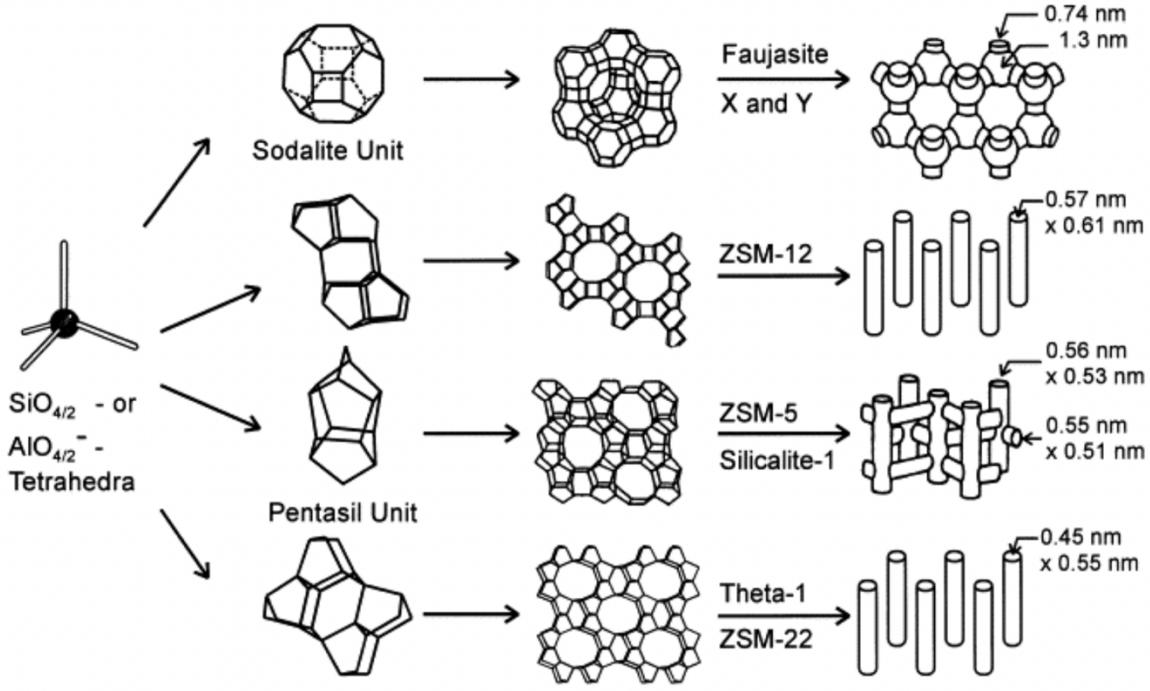


Figure 1. The configuration of four chosen zeolites along with their respective micro-pore system and measurements. This figure is taken from ref. [5]

1.1.2 ZSM-5 zeolite

This project is centered around ZSM5, a zeolite extensively employed in the petrochemical industry for hydrocarbon conversion. ZSM-5 (Zeolite Socony Mobile-5), a notable zeolite in the pentasil and "high silica" zeolite family with a Si/Al ratio greater than 10, was invented by R.J. Argauer and G.R. Landolt[6] of Socony Mobile in 1972.

ZSM-5 crystals typically have a coffin- or parallelepiped-like shape, with dimensions ranging from 100 nm to 100 mm. [7] Inside these crystals, there is a three-dimensional microporous channel system, as depicted in **Figure 2**, which serves as a transport mechanism for molecules. The channel system consists of straight and sinusoidal pores that align with the [010] and [100] crystallographic planes, respectively. As the two pore types intersect at regular intervals, molecules can diffuse in the [0] direction. The average pore size of these channels is approximately 5.5 x 5.5 Å, [8] and the channel intersections create cavities that are 6.36 Å in diameter, [9] preventing the entry or exit of molecules that exceed these dimensions. However, larger molecules can fit into the cavities at the channel intersections. These unique shape-selective properties allow ZSM5 and other zeolites to function effectively as molecular sieves.

ZSM-5 displays strong acidic properties upon occupation of its cation exchange centers with protons (H^+) resulting in the formation of BAS, shown in **Figure 3**. The degree of acidity is influenced by the silica to aluminum ratio (SAR) within the framework, with a higher SAR leading to reduced acidity. The crystallographic formula for the unit cell of ZSM-5 is provided as:

$$Na_nAl_nSi_{96-n}O_{192}$$

The value of the variable "n" in the unit cell formula of ZSM-5 can vary from 0 to 27. In a unit cell, the total number of silica and aluminum atoms is 96. Therefore, the ratio of silicon to aluminum atoms within the ZSM-5 lattice can differ widely. Usually, ZSM-5 zeolites have a SAR of greater than 10. A higher SAR results in ZSM-5 zeolite being hydrophobic and thermally stable, which is advantageous for several applications.

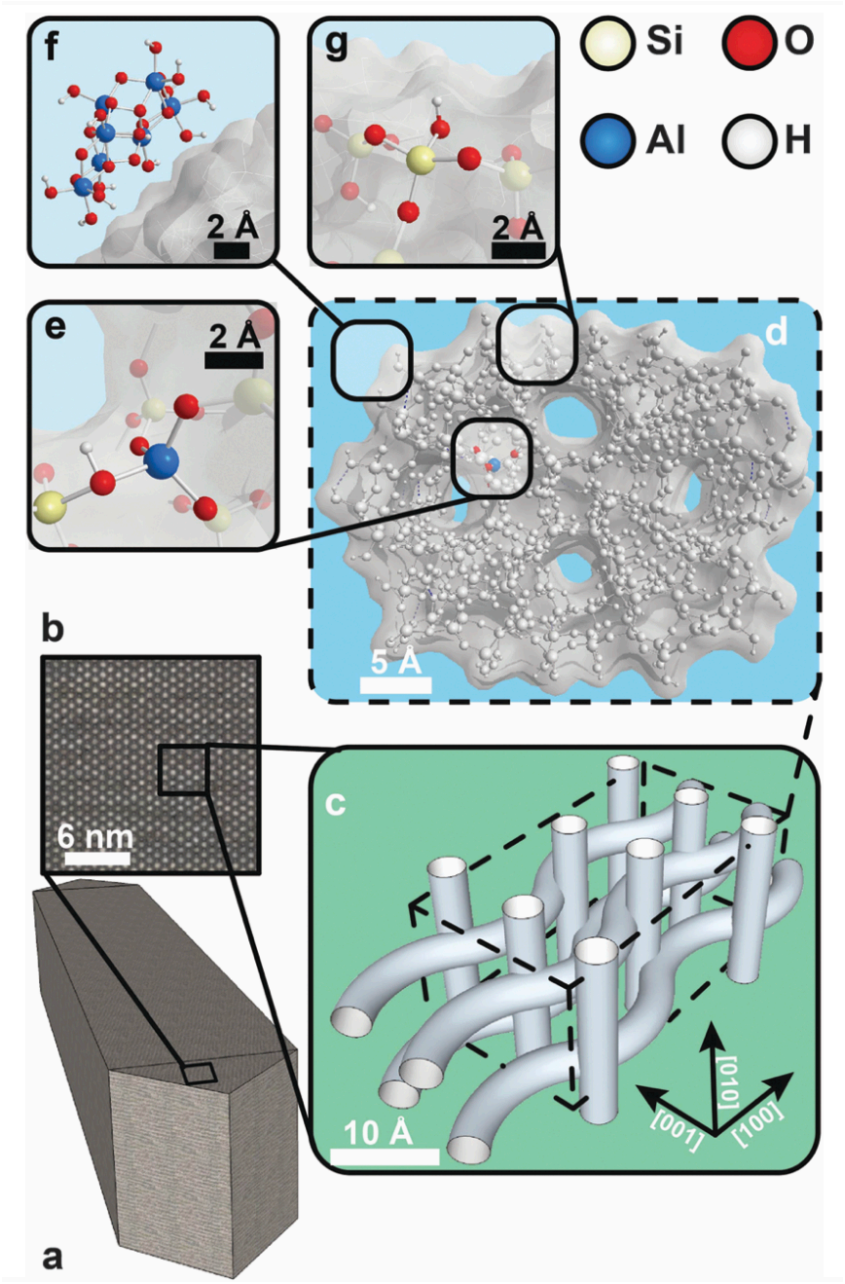


Figure 2. Overview of H-ZSM5 at various dimensional scale. a) a micro-sized coffin-shaped H-ZSM-5 crystal. b) straight pores [001] [100] planes. c) three-dimensional channel system. d) MFI framework comprises of silica and aluminum tetrahedra. e) BAS. f) extra-framework aluminum from dealumination. g) terminal silanol group. This figure is taken from ref. [9]

Due to its acidity, shape selectivity, and thermal stability, ZSM-5 is an essential heterogeneous catalyst in the petrochemical industry. The BASs demonstrate significant catalytic activity in the hydrocarbon cracking process. Additionally, the unique pore structure within the ZSM-5 framework provides shape-selectivity effects that lead to the production of valuable commercial products, including alkenes, light alkenes, and aromatic molecules in the gasoline range. [10] ZSM-5 is used in various applications, such as cracking of heavy hydrocarbons, methanol to gasoline conversion, and biomass conversion. [9]

1.1.3 Distribution of aluminum in zeolites

Our understanding of how aluminum atoms are arranged in zeolite frameworks is limited. Although X-ray diffraction can determine the basic structure and chemical composition of the framework, aluminum distribution cannot be determined due to the nearly identical behavior of Si and Al under X-ray spectroscopy, making it challenging to differentiate between them. Previous studies showed that the sitting of Al is not arbitrary and depends on the synthesis parameters and Si/Al ratio. [11, 12] These dependences of activity and selectivity on the site location could result from different sub-nanometer confinement environments. That is, the transition states are more stabilized in tighter confinement due to enhanced van der Waals interactions between the transition states and the zeolite frameworks.[12-15] As illustration, Li et al.[12] have synthesized H-ZSM5 zeolite enriched with Al locating in 10-member ring (MR) channels by using B and observed higher selectivity to propene and less to butene and pentene in cracking reactions of 1-hexene over these samples than on conventionally prepared H-ZSM5. This less selectivity to large olefins was attributed to the reduced preference of formation of bulky cationic intermediates in 10-MR channels due to the small confinement. Similarly, oligomerization, cyclization and hydrogen

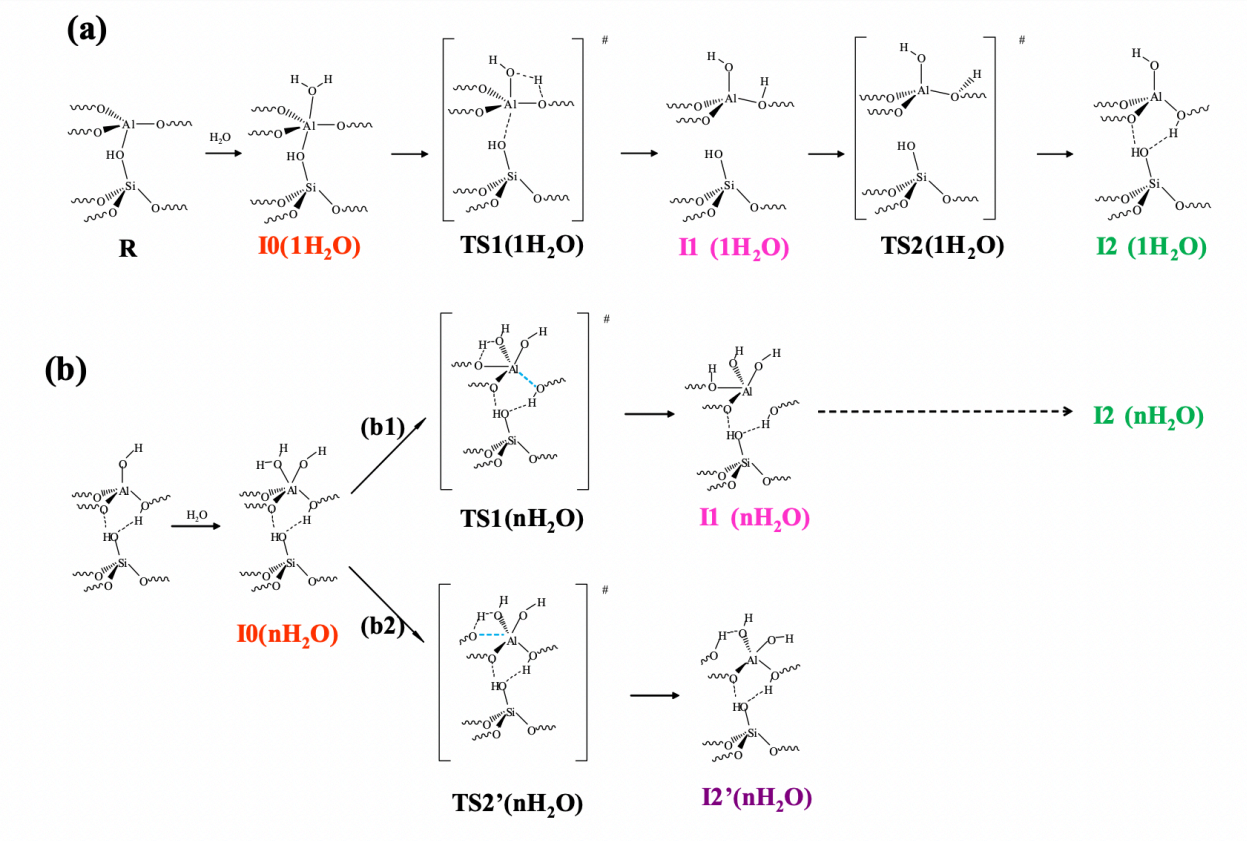
transfer reactions producing aromatics and alkanes were proposed to happen preferably at intersections. According to Janda et al. [14], the dehydrogenation and terminal cracking of n-butene were found to occur preferentially at the intersection due to larger intrinsic entropies that result in lower Gibbs free energies at sites with smaller confinement. Through the use of density functional theory (DFT) calculations, Boronat et al. [16] examined the mechanism of carbonylation of methanol and dimethyl ether (DME) at different sites in H-MOR zeolites. They discovered that the selectivity of methanol carbonylation was greater in the 8-MR location due to the restricted pore size, which prevented the reaction of methanol from forming DME.

As aluminum atoms are responsible for desirable properties, considerable research has been undertaken in this field. The most referenced rule for Al occupation in zeolite is Löwenstein's rule, which states that two aluminum atoms cannot share the same oxygen atom in their tetrahedra. Although experimental evidence for this rule is lacking, it is frequently used to explain data, including computational results.

1.1.4 Extra-framework aluminum (EFAL) and partially coordinated aluminum (PFAL) in zeolites.

The literature indicates that the nature of acid sites could be more intricate, as some Al framework atoms are removed from the framework and form EFAL or PFAL species. Furthermore, it is widely recognized that exposure of zeolite to moisture can accentuate the concentration of EFAL species. According to the dealumination mechanism proposed by Silaghi, [17] each hydrolysis step leads to one Al-O bond breaking, shown in **Scheme 1**. The partial hydrolysis of framework aluminum generates tetrahedral PFAL species, which can be the precursors of EFAL. The PFAL species partially coordinate to the zeolite framework through lattice oxygen atoms and hydroxyl groups being other coordination. [18, 19] After reacting with four

H_2O molecules, the Al framework will be extracted from the framework to become EFAL. The most preferred EFAL species are oxoaluminum ions, such as AlO^+, $Al(OH)^{2+}$, $Al(OH)^{2+}$ and Al^{3+}, and some neutral species including $Al(OH)_3$ and AlOOH.[20, 21] These EFAL species can transform into each other in the presence of water. [22]



Scheme 1. Mechanism of framework atoms' hydrolysis, taken from ref. [17]

EFALs are positioned in close proximity to traditional BAS, producing synergistic sites that are deemed responsible for the enhanced catalytic activity observed in several hydrocarbon conversion reactions. With the growing interest in employing zeolites as catalysts for the solid-liquid and solid-gas interface, comprehending the microstructure's response to activity become increasingly crucial. Despite the reported positive impact of EFAL and PFAL, the mechanism underlying their activity enhancement remains relatively obscure.

1.2 Density Functional Theory (DFT)

DFT is a widely used theory in computational physics that aims to describe every property of a material through its ground-state electron density. The Hohenberg-Kohn theorems form the basis of DFT and offer a simple explanation of its underlying principles. However, these theorems alone do not provide a practical way to apply DFT in real applications. Kohn and Sham proposed an approach for calculating the properties of many-electron systems, which paved the way for further developments. The theorems and derivations used in this context are presented according to R. Martin's work. [23]

1.2.1 Hohenberg-Kohn theorems

Hohenberg and Kohn's theorems offer a method for determining the ground state electron density in a system with many particles. The Hamiltonian of such a system can be expressed as:

$$\hat{\mathrm{H}} = -\frac{\hbar^2}{2\mathrm{m_e}}\sum_{\mathrm{i}}\nabla_{\mathrm{i}}^2 + \sum_{\mathrm{i}}\mathrm{V_{ext}}(\mathbf{r}) + \frac{1}{2}\sum_{\mathrm{i}\neq\mathrm{j}}\frac{\mathrm{e}^2}{|\mathbf{r_i}-\mathbf{r_j}|} \tag{1.1}$$

where the first component represents the system's kinetic energy, the second factor corresponds to the impact of an external potential, and the final term denotes the interaction among electrons.

Theorem 1: The ground state density of particles, $n_0(r)$, uniquely determines the external potential V_{ext}, that acts on system of interacting particles.

To prove this theorem, two external potentials that differ by more than a constant are considered. Despite producing the exact same ground state energy, these potentials give rise to distinct Hamiltonian, $\widehat{\boldsymbol{H}}^{(\mathbf{1})}$ and $\widehat{\boldsymbol{H}}^{(\mathbf{2})}$, and ground state wavefunctions, $\Psi^{(1)}$ and $\Psi^{(2)}$. Assuming that the ground state is non-degenerate, the following equation can be derived by noting that $\Psi^{(2)}$ is not the ground state of $\widehat{\boldsymbol{H}}^{(\mathbf{1})}$.

$$\mathrm{E}^{(1)} = \left\langle \Psi^{(1)} \middle| \widehat{\mathrm{H}^{(1)}} \middle| \Psi^{(1)} \right\rangle < \left\langle \Psi^{(2)} \middle| \widehat{\mathrm{H}^{(1)}} \middle| \Psi^{(2)} \right\rangle \tag{1.2}$$

The following expression is obtained by reworking the final term in equation (2.2) and employing the Hamiltonian from equation (2.1):

$$\left\langle \boldsymbol{\Psi}^{(\mathbf{2})} \middle| \widehat{\mathbf{H}^{(\mathbf{1})}} \middle| \boldsymbol{\Psi}^{(\mathbf{2})} \right\rangle = \left\langle \boldsymbol{\Psi}^{(\mathbf{2})} \middle| \widehat{\mathbf{H}^{(\mathbf{2})}} \middle| \boldsymbol{\Psi}^{(\mathbf{2})} \right\rangle - \left\langle \boldsymbol{\Psi}^{(\mathbf{2})} \middle| \widehat{\mathbf{H}^{(\mathbf{1})}} - \widehat{\mathbf{H}^{(\mathbf{2})}} \middle| \boldsymbol{\Psi}^{(\mathbf{2})} \right\rangle \tag{1.3}$$

$$= \mathrm{E}^{(2)} + \int \mathrm{r}\mathrm{d}^3\mathrm{r} \left[\mathrm{V}_{\mathrm{ext}}^{(1)} - \mathrm{V}_{\mathrm{ext}}^{(2)} \right] \mathrm{n}_0(\mathbf{r}) \tag{1.4}$$

Therefore, the inequality can be expressed as:

$$\mathrm{E}^{(1)} < \mathrm{E}^{(2)} + \int \mathrm{r}\mathrm{d}^3\mathrm{r} \left[\mathrm{V}_{\mathrm{ext}}^{(1)} - \mathrm{V}_{\mathrm{ext}}^{(2)} \right] \mathrm{n}_0(\mathbf{r}) \tag{1.5}$$

Applying the same approach for $\mathrm{E}^{(2)}$, we find that:

$$\mathrm{E}^{(2)} < \mathrm{E}^{(1)} + \int \mathrm{r}\mathrm{d}^3\mathrm{r} \left[\mathrm{V}_{\mathrm{ext}}^{(2)} - \mathrm{V}_{\mathrm{ext}}^{(1)} \right] \mathrm{n}_0(\mathbf{r}) \tag{1.6}$$

The resulting inequality obtained by adding the two inequalities in Eq. (2.5) and Eq. (2.6) is $E^{(1)} + E^{(2)} < E^{(1)} + E^{(2)}$, which is self-contradictory. This contradiction serves as proof of the theorem, which states that the electron density of a non-degenerate system cannot be identical for two external potentials that differ by more than a constant. However, the potential can be uniquely determined by the electron density, up a constant. A corollary of this theorem is that since the Hamiltonian is determined solely by the ground state density but for a constant energy shift, the many-body wavefunctions for all states can be determined.

The ground state energy of a system can be represented by a universal energy functional E[n], which is independent of the external potential V_{ext}. The global minimum of this functional corresponds to the ground state energy, and the density n(r) that corresponds to this minimum value is the ground state density of the system for any external potential V_{ext}.

To prove this theorem, one must consider that the electron density n(r) governs all characteristics of a system. These characteristics can be regarded as a functional form of n(r). The total energy functional of such a system can be defined in the following manner:

$$E_{HK} = T[n] + E_{int}[n] + \int r d^3 r\, V_{ext}(\mathbf{r}) n(\mathbf{r}) + E_{II} \tag{1.7}$$

where the first two expressions in the equation refer to the kinetic and potential energies, while the third term accounts for the effect of the external potential and the final term denotes the interaction energy of the nuclei. Furthermore, it should be noted that the first two terms are universal in nature, as they solely rely on density.

Examine two distinct densities denoted as $n^{(1)}(\mathbf{r})$ and $n^{(2)}(\mathbf{r})$. The external potential $\boldsymbol{V_{ext}^{(1)}}$ is associated with n(1), and the ground state expectation value of the Hamiltonian with wavefunction $\Psi^{(1)}$ can be expressed as:

$$E^{(1)} = \left\langle \Psi^{(1)} \middle| \widehat{H^{(1)}} \middle| \Psi^{(1)} \right\rangle < \left\langle \Psi^{(2)} \middle| \widehat{H^{(1)}} \middle| \Psi^{(2)} \right\rangle = E^{(2)} \tag{1.8}$$

As expected, the corresponding density $n^{(2)}$ with wavefunction $\Psi^{(2)}$ exhibits a higher energy level under the same external potential:

$$E^{(1)} = \left\langle \Psi^{(1)} \middle| \widehat{H^{(1)}} \middle| \Psi^{(1)} \right\rangle < \left\langle \Psi^{(2)} \middle| \widehat{H^{(1)}} \middle| \Psi^{(2)} \right\rangle = E^{(2)} \tag{1.9}$$

This implies that the Hohenberg-Kohn functional yields a lower energy value for the appropriate ground state density $n_0(r)$ compared to any other density n(r). One implication of this theorem is that if the internal energy section of the functional is identified, the precise ground state density can be determined by minimizing the total system energy. By utilizing both theorems, a self- consistent loop can be established to identify the ground state density of the system, as illustrated in **Figure 3**. However, it is important to note that these theorems do not offer any practical methods for solving many-body wavefunctions.

$$F_{HK} = T[n] + E_{int}[n] \tag{1.10}$$

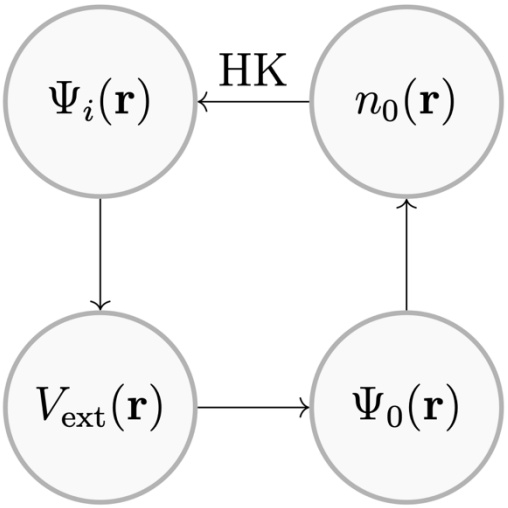


Figure 3. This process allows for the iterative determination of the ground state density of a given system, by utilizing the principle outlined in the Hohenberg-Kohn theorems, taken from ref. [23]

1.2.2 The Kohn-Sham equation: DFT in practice

The Hohenberg-Kohn theorems offer an accurate theory, but the challenge arises when attempting to solve the equations for systems composed of numerous particles due to the interaction between the particles. To overcome this hurdle, the Kohn-Sham approach proposes replacing the interacting system with an auxiliary system that incorporates all the dynamics of the original system. This is achieved by making an assumption based on the two factors. Firstly, it is assumed that the ground state density for the non-interacting system is identical to that of the interacting one. Secondly, it is assumed that the auxiliary Hamiltonian includes the conventional operator for the kinetic energy portion of the energy along with an effective local potential V_{eff}^{σ}(r). The energy functional for such a system is derived from this.

$$E_{KS} = T_s[n] + \int r d\,\mathbf{r} V_{ext}(\mathbf{r}) n(\mathbf{r}) + E_{Hartree}[n] + E_{xc}[n] \tag{1.11}$$

The representation presented in Eq.(2.7) bears some resemblance to the Hohenberg-Kohn functional, albeit with certain modifications. The first term in Eq.(2.11) corresponds to the kinetic energy of the system, the second term arises from the nuclei's potential and other external fields, the third term is the Hartree term originating from the Coulomb interaction energy, the fourth term represents the nucleic interactions, the final term is due to exchange-correlation. The key innovation in the ansatz lies in segregating the independent kinetic energies of the particles and the long-range interactions in the Hartree terms, which allows the exchange-correlation term to be approximated as a local functional. The form of the exchange-correlation functional is expressed as follows:

$$E_{xc}[n] = \frac{1}{2} \int r d^3 r\, n(\mathbf{r}) \int r d^3 r' \frac{\overline{n_{xc}}(\mathbf{r}, \mathbf{r}')}{|\mathbf{r} - \mathbf{r}'|} \tag{1.12}$$

The exchange-correlation hole is denoted by $\bar{n}_{xc}$, and there exists no exact solution for its actual appearance. Regarding the precision of real DFT calculations, the choice of exchange-correlation functional plays a crucial role in the accuracy of the results. The Kohn-Sham ansatz offers a practical approach to utilizing DFT. While Hohenberg and Kohn established a self-consistency loop to iteratively determine the electron density of the ground state of an interacting many-body system, the ansatz proposed by Kohn and Sham provides a practical way of using DFT. Figure 4 illustrates the self-consistency loop in conjunction with the ansatz.

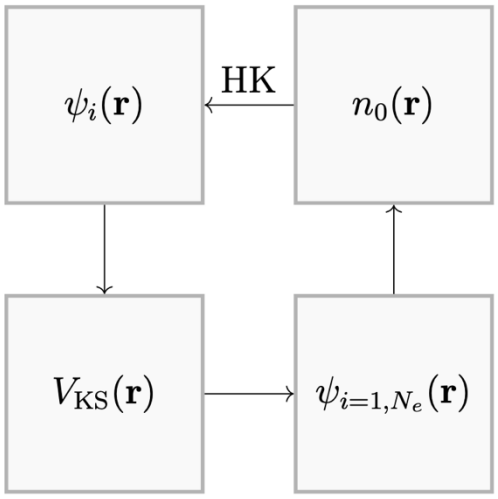


Figure 4. Through the use of the Kohn-Sham ansatz, it becomes possible to determine the ground state properties of a many-body system in a self-consistent manner, taken from ref. [23]

CHAPTER 2: Identify different protonic and aluminum species in H-ZSM5 zeolite

2.1 Abstract

Solid-acid materials with tunable acidic and structural properties are promising heterogeneous catalysts for tailoring the activity and selectivity of advanced petrochemical processes. Additionally, the catalytic performances are dictated by acidic strength, density and local environment of active sites. The latter is related to their locations and the presence of EFAL or PFAL species, which strongly affect the reaction mechanism and host-guest interaction. Here, we exploited DFT calculations to interpret solid-state ^{1}H NMR and ^{27}Al NMR spectroscopy for identifying different structures of possible active sites in H-ZSM5 zeolite. The active sites can be IBA or synergistic sites (BAS/EFAL and BAS/PFAL). The DFT results revealed that ^{1}H chemical shift of isolated Brønsted acid sites (IBAS) is sensitive to their locations. The recently reported broad signal 11-18 ppm arises from the BAS that forms hydrogen bonds with oxygen atoms belonging to vicinal EFAL/PFAL, and the silanol groups in silanol nests resulted from dealumination. Moreover, computed ^{27}Al NMR values of tetrahedral Al are in the well-known range of 53-63 ppm, while the ^{27}Al NMR of EFAL and PFAL can expand to a boarder range of 55-85 ppm. The combination of DFT calculation and NMR spectroscopy allows to clarify all protonic and aluminum species in H-ZSM5 zeolite. All these findings are important in understanding the structures of H-ZSM5 zeolite and the catalytic role of EFAL/PFAL species, which is expected to be beneficial for rational design of numerous zeolite-mediated hydrocarbon reactions.

2.2 Introduction

Solid-acid catalysts are valuable for many catalyzed processes such as alkane cracking, alkene isomerization, aromatic alkylation, polymerization and biomass conversion.[24, 25] Microporous zeolites with pore diameters in the sub-nanometer range are solid-acid catalysts most commonly employed. The catalytic properties of zeolites arise from the strong acidic protons, positioned at BASs, that compensate for the negative charge on the framework, resulted from the substitution of Si^{4+} with Al^{3+}. On the other hand, the acid site's distribution and location determine their performance in hydrocarbon transformations. [14, 15, 26, 27]

Previous studies showed that the sitting of Al is not arbitrary and depends on the synthesis parameters and Si/Al ratio.[11, 12] These dependences of activity and selectivity on the site location could result from different sub-nanometer confinement environments. That is, the transition states are more stabilized in tighter confinement due to enhanced van der Waals interactions between the transition states and the zeolite frameworks.[12-15] For example, Li et al.[12] have synthesized H-ZSM5 zeolite enriched with Al locating in 10-member ring (MR) channels by using B and observed higher selectivity to propene and less to butene and pentene in cracking reactions of 1-hexene over these samples than on conventionally prepared H-ZSM5. This less selectivity to large olefins was attributed to the reduced preference of formation of bulky cationic intermediates in 10-MR channels due to the small confinement. Similarly, oligomerization, cyclization and hydrogen transfer reactions producing aromatics and alkanes were proposed to happen preferably at intersections. According to Janda et al. [14], the dehydrogenation and terminal cracking of n-butene were found to occur preferentially at the intersection due to larger intrinsic entropies that result in lower Gibbs free energies at sites with smaller confinement. Through the use of DFT calculations, Boronat et al. [16] examined the mechanism of carbonylation of methanol and dimethyl ether (DME)

at different sites in H-MOR zeolites. They discovered that the selectivity of methanol carbonylation was greater in the 8-MR location due to the restricted pore size, which prevented the reaction of methanol from forming DME.

On the other hand, literature has presented evidence that indicates the acid site character may be more intricate, as some Al framework atoms can be extracted from the framework and create EFAL. [17, 18, 25, 28-32] Moreover, it is widely acknowledged that exposing zeolite to moisture can intensify the density of EFAL. [28, 32-34] The most preferred EFAL species are oxoaluminum ions, such as AlO^{+}, $Al(OH)^{2+}$, $Al(OH)^{2+}$ and Al^{3+}, and some neutral species including $Al(OH)_3$ and AlOOH. [20, 21, 34] These EFAL species can transform between each other with the presence of water. [22] Apart from the EFAL that are completely removed from the zeolite framework, PFAL species are also present in zeolite catalysts due to incomplete hydrolysis of framework Al atoms. In a previous study, 2-dimensional ^{27}Al NMR spectroscopy provided evidence for two types of tetrahedral aluminum in dehydrated H-ZSM-5 zeolite in close proximity to each other: the first, Al(IV)-1, arose from framework BAS, while the second, Al(IV)-2 was attributed to incompletely hydrolyzed Al(IV)-2. [35] The free energy involved in the hydrolysis of Al framework to form different degrees of PFAL species is presented in Chapter 3. [36] PFAL refers to Al partially coordinated to the framework with the remaining coordination being OH groups. These species are precursors to EFAL species under water treatment. Various types of PFAL have been reported depending on the treatment conditions. [18] While steaming may lead to a loss of BAS density, a brief steaming period has been shown to significantly enhance the rate of many hydrocarbon transformations due to the synergistic sites effect of BAS/EFAL and BAS/PFAL, as reported in previous studies. More recently, pulsed water treatment has been used to introduce EFAL into MFI

in a more controlled manner, leading to significantly enhanced cracking rates over these synergistic sites. [25]

Identification of the locations and structures of the acid sites is thus critical to understand the catalytic behaviors and controlling the desirable products in zeolite. Solid-state NMR spectroscopy is a powerful tool for investigating the structural characterization of active sites in zeolites. ^{1}H NMR and ^{27}Al NMR spectroscopy can provide valuable information to identify the structures of active sites in zeolites. [28-30, 35, 37-40] While ^{27}Al NMR can provide information about aluminum state, the local environment of proton can be characterized by ^{1}H NMR. The MFI structure is a good zeolite framework for such a study since it is very unsymmetrical with 12 crystallographic T sites.

In other to comprehend the catalytic behaviors and regulate the desired product in zeolite, it is crucial to identify structure and location of active sites. Solid-state NMR spectroscopy is a potential tool for investigating the structural characterization of active sites in zeolite. Valuable information about the structure of zeolite can be obtained through ^{1}H NMR and ^{27}Al NMR spectroscopy, with ^{27}Al NMR providing information about the aluminum state and ^{1}H NMR characterizing the local environment of protons. The MFI structure is highly unsymmetrical with 12 distinct crystallographic T sites, which is an excellent zeolite framework for conducting such studies. Chen et al. [29] carried out one- and two-dimensional ^{1}H NMR spectroscopy to elucidate various types of protonic species in H-ZSM5 zeolite. The signal 4.0-5.0 ppm are generally assigned to the well-known BAS. The two signals 2.8 and 11-16 ppm can be removed by ammonium hexafluorosilicate (AHFS), suggesting that these species could be associated with EFAL. Our recent work reported that the broad signal at 11-16 ppm rose from BAS in proximity with EFAL $Al(OH)_2$ or $Al(OH)_3$ and the signal at 2.8 ppm was assigned to hydroxyl group of

EFAL $Al(OH)_2$. [41] In addition, the broad signal at 5-9 ppm rising from both framework and EFAL species are less understood. For ^{27}Al NMR, the three main peaks at roughly 60, 30 and 0 ppm serve as indicators for tetrahedral framework Al, five-coordinated, and octahedral EFAL. [22, 32] The ^{27}Al chemical shift signal could expand to 65-74 ppm region in the early stage of hydrolysis. [35, 42] Additionally, the 2-dimensional $^{1}H\{^{27}Al\}$ NMR spectra gave evidence that there are two coupling between tetrahedral Al and proton: 51/4.2 ppm and 54/2.8 ppm in H-ZSM5. [43] In particular, the 51/4.2 ppm correlation is related to the well-known BAS while 54/2.8 ppm resulted from the coupling of either framework crystallization defect or partially hydrolyzed framework Al. [35] These findings allow us to conclude that the synergies between BAS and EFAL species present in the dehydrated H-ZSM5 zeolite. Nevertheless, further investigation is needed to elucidate the detailed structures of all possible species after hydrothermal treatment, as the signal overlaps in experimental spectra make interpretation complex. A study combining 1H NMR and 27Al NMR based on DFT-calculation is therefore valuable for giving detailed information on the structures of different aluminum species as well as their interplay in H-ZSM-5 zeolite.

Here, we benchmark DFT data and experimental NMR spectra for H-ZSM5 zeolite. Our analysis includes a comprehensive examination of the ^{1}H chemical shift and ^{27}Al chemical shift for isolated BAS at different locations, as well as a discussion of the chemical shifts for potential synergistic sites involving BAS and EFAL or PFAL. The strong agreement between our experimental findings and theoretical calculations enables us to differentiate between NMR signals and uncover intricate details about the structures of synergistic sites.

2.2.1 NMR Chemical Shift

This chapter will involve the computation of the nuclear magnetic resonance (NMR) chemical shift of H-ZSM-5 zeolite. To identify the structure and location of active sites and the local environment surrounding them, both ^{1}H NMR and ^{27}Al NMR were employed. The interaction between an external magnetic field, B, and a nuclear magnetic moment is expressed as follows:

$$\mathrm{E} = -\mu_{\mathrm{A}} \cdot \mathrm{B} \tag{2.1}$$

In the above equation, $\boldsymbol{\mu}_{\mathrm{A}}$ represents the spin magnetic moment of a specific nucleus, while B denotes an external static homogeneous magnetic field. In atoms, molecules, and solids, the electrons provide shielding for B, meaning that the nucleus interacts with an effective filed. Therefore, when nuclear σ is subjected to a specific chemical environment, and σ represents the nuclear shielding tensor, then:

$$\mathrm{E} = -\mu_{\mathrm{A}} \cdot (1 - \sigma)\mathrm{B} \tag{2.2}$$

The term $\boldsymbol{\mu}_{\mathrm{A}}$. **B** is typically excluded from zero-order quantum chemistry calculations; therefore, the nuclear shielding tensor can be expressed as:

$$\sigma_{\mathrm{A}} = \left.\frac{\partial^2 \mathrm{E}}{\partial \mathrm{B}\, \partial \mu_{\mathrm{A}}}\right|_{\mathrm{B}=0,\mu_{\mathrm{A}}=0} \tag{2.3}$$

To obtain the formal agreement with Eq. (2.3), the second derivative can be computed analytically, but numerical methods are often preferred due to the complexity of the energy expression. To establish formal agreement with Eq. (2.3), E, H and Ψ are expanded in a perturbation series in $\boldsymbol{\mu}_{\mathrm{A}}$ and **B,** and terms that are bi-linear in both are collected. The dimensionless quantity σ, which is typically given in units of 10^{-6} (parts per million, or ppm), is established. The rotational average is represented by the isotropic shielding constant, σ. Experimental data typically report the chemical shift, δ, which is defined as:

$$\delta = \sigma^{\text{reference}} - \sigma \quad (2.4)$$

In this context, the value of s is established for a nucleus of interest in a reference compound. Quantum chemical calculations of NMR for similar molecules often produce consistent errors of a similar magnitude and direction, when using the same functional and basic set. Therefore, a more accurate reference molecule for computational purposes may be one with a well-known chemical shift that is chemically similar to the molecule under investigation.

2.3 Computational methods

Zeolite model geometry: The unit cell of ZMS-5 consists of 96 T atoms (T = Si, Al) and 192 oxygen atoms. The proton and aluminum chemical shifts of twenty-four BAS at different locations including intersection, straight channel, sinusoidal channel, small void, 5-member ring (5-MR) and 6-member-ring (6-MR) were computed. Ghorbanpour et al. [44] reported that BAS at T7 was the most thermodynamically stable. Based on that finding, a BAS was positioned at T7 in all synergistic site configurations. To obey the Löwenstein's rule, the positions of Al site pair in framework were set in the Al-O-(Si-O)$_x$-Al (x = 1 and 2) sequences. The PFAL species are partially hydrolyzed Al calculated following the dealumination mechanism by Silaghi et al. [17]

Computations: Our DFT calculations were performed using Vienna ab initio simulation package (VASP). [45] Perdew-Burke-Ernzerhof (PBE)[46] generalized gradient approximation (GGA) was used for the exchange-correlation potential. DFT-D3 semi-empirical method[47] was employed to account for the van der Waals interaction. The system was fully relaxed with a kinetic cutoff of 400 eV. A single Γ point in the first Brillouin zone was used for atomic relaxation. The lattice parameters of unit cell zeolite were set accordingly to the experimental study: a = 20.078 Å, b = 19.894 Å and c = 13.372 Å, as in our previous studies. [25, 30, 35, 48] The geometry optimizations

continued until the force excess on each atom was smaller than 0.02 eV/Å. The self-consistent field electronic calculations were assumed to cone 10^{-6} eV.

The chemical shift was calculated using the linear response function method. [49] The ^{1}H NMR and ^{27}Al NMR chemical shifts were obtained by shift factors of 30.9 and 562 ppm, respectively, which convert the calculated chemical shielding to chemical shifts. The protonic and aluminum chemical shifts were subsequently computed for all proposed complexes.

2.4 Results and discussions

2.4.1 ^{1}H NMR and ^{27}Al NMR of isolated Brønsted acid sites at different locations.

We conducted benchmark studies by contrasting experimental NMR spectroscopy with calculated 1H NM and 27Al NMR data to identify potential species in H-ZSM5 zeolite. Through this investigation, we aimed to elucidate the structure of all feasible species. **Figure 5** depicted the three-dimensional microporous channel system of ZSM-5 zeolite, which comprises of straight channels oriented along b direction and sinusoidal channels running along a direction. The two types of channels are connected at intersections, which are 6.36 Å in diameter.[9] These channels serve as delivery systems for molecules diffusion in the a, b and c directions. There are 12 crystallographically distinct tetrahedral sites and 6 possible positions for a BAS including intersection, straight channel, sinusoidal channel, small void, 5-MR and 6-MR. In experimental ^{1}H NMR and ^{27}Al NMR spectra, the well-known signal of BAS is at 4.0-4.5 pm and the tetrahedral framework Al is at 54-61 ppm.[25, 28, 29, 32, 35, 50, 51].

Figure 6 illustrates the calculated ^{1}H and ^{27}Al chemical shifts of IBAS and their responding calculated structures at different locations. As demonstrated in **Figure 6a-f**, at the intersection and

straight channel, H^1 chemical shift of acidic OH groups are in between 4.1 and 4.5 ppm. In the sinusoidal and small voids, the ^1H chemical shifts are slightly higher, in the range of 4.6-5.3 ppm **(Figure 6g-l)**. Notably, **in Figure 6m-r**, the ^1H chemical shifts of BAS at the 5-MR and 6-MR downfield in 5.0-8.5 ppm region, which causes from the hydrogen bonds formed with oxygen atom on the ring. The high electronegativity of oxygen to which the proton is hydrogen bonded decreases the electron cloud around the proton, leading to deshielding of the protons. The variation of ^1H chemical shifts of BAS is attributed to the degree of hydrogen bonds. Moreover, the deshileding phenomenon also account for the slightly higher ^1H chemical shift of certain BAS located in the sinusoidal channel and small voids. These regions have smaller confinements, enabling more oxygen atoms to encircle the BAS as compared to the intersection. This results in the withdrawal of electron density from neighboring atoms by these electronegative atoms, leading to higher chemical shift values. Furthermore, the deshielding effect caused by hydrogen bond formation in 5MR/6-MR is significantly more pronounced than that of the surrounding oxygen in the sinusoidal and small voids. Hence, ^1H chemical shifts of BAS in 5-MR/6-MR can shift to 8.5 ppm. These outcomes suggest that the protonic chemical shift of IBAS is sensitive to their positions. Our calculated ^1H NMR values of BAS at the intersection and void channels agree well with the well-known 4.0-5.0 ppm peak. According to research by Gounder's group, the stability of framework Al centers can be influenced by their surrounding environment. [52] The majority of substituted tetrahedral Al is connected to oxygen atoms that are approachable to the intersection or the main channel void. Particularly, the relative Al exchange with TPA^+ indicate a intrinsic preference for Al-sitting; the most stable Al substitutions are positioned close to T12, which locate at the intersection. [52] Additionally, BAS preferentially point toward the large voids. [26] Thus, most of

BAS in ZSM-5 dominantly reside at the intersection and main void channels, which exhibit ^{1}H NMR in the range of 4.1-5.5 ppm.

In experiments, the board 5-9 ppm peak observed at the shoulder downfield of the BAS peak is less understood. However, it has been demonstrated that ammonium hexafluorosilicate (AHFS) can partially remove this peak, indicating that it arises from both framework and extra-framework species. [28, 29] Our results in **Figure 6m-r** provide the first evidence that the peak 5-9 ppm can be attributed to framework BAS located at 5-MR and 6-MR, which forms H-bonds with framework oxygen atoms. The dependence of ^{1}H NMR of BAS to locations has been reported previously; for example, the peaks at 4.3 and 5 ppm were assigned to acidic hydroxyl groups at super cages and sodalite cages in calcined H-Y zeolite, respectively. Furthermore, the ^{27}Al chemical shifts of tetrahedral framework BAS are in the range of 53-63 ppm, which are in good agreement with well-known tetrahedral Al peak[22, 35, 40, 42, 50, 51].

For ^{27}Al NMR, this section solely focuses on the tetrahedral framework BAS, which exhibits chemical shift between 53-63 ppm. This range is consistent with the well-known chemical shift range for tetrahedral Al.

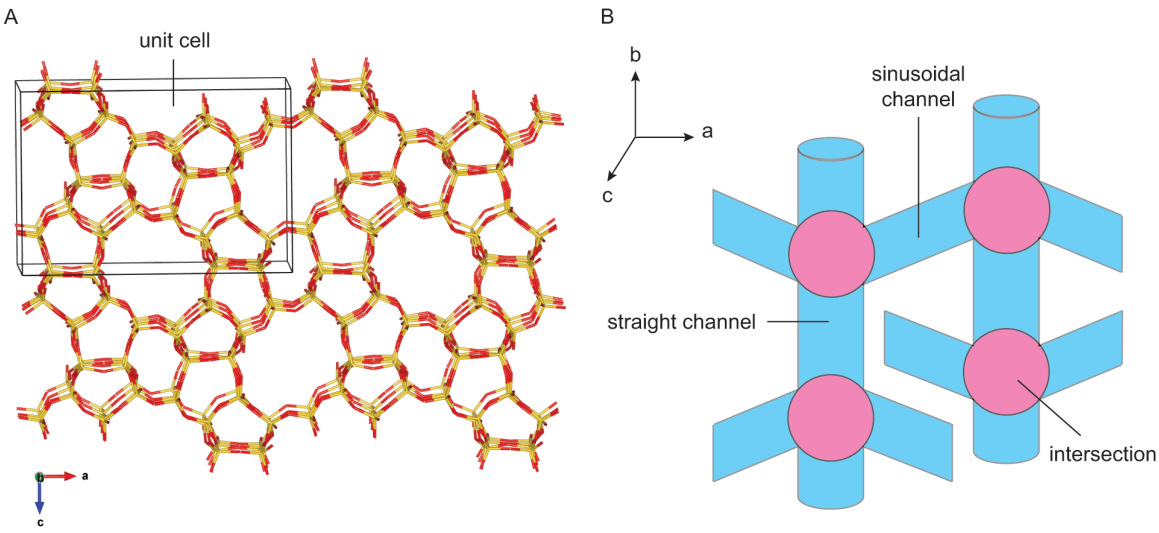


Figure 5. A) Calculated H-ZSM5 zeolite structure; B) Schematic diagram of three-dimensional channel system of H-ZSM5 zeolite morphology comprising of the straight and the sinusoidal channel.

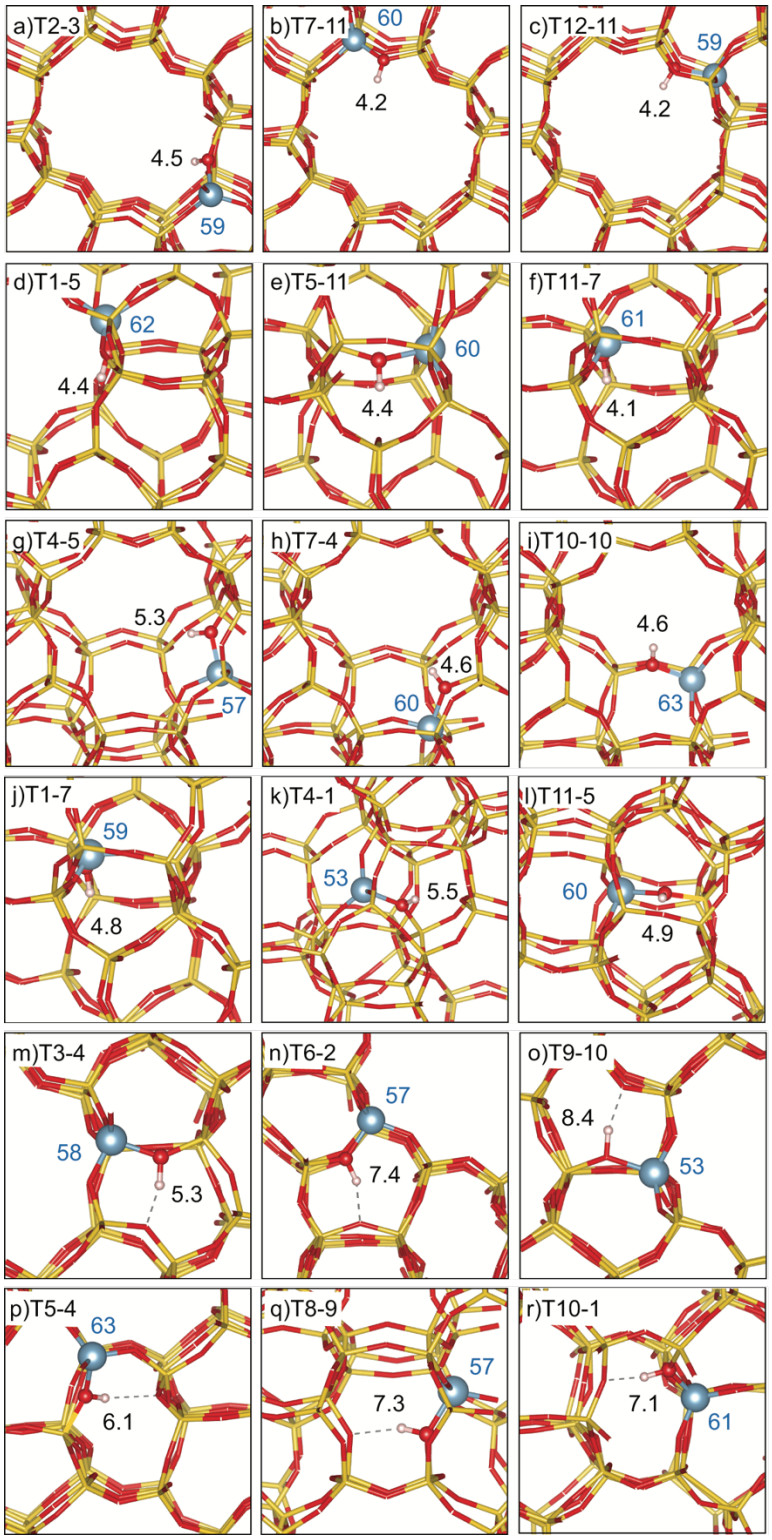


Figure 6. DFT-calculated proton and aluminum chemical shift of BAS at different locations in H-ZSM5 zeolite: a, b, c) intersection; d, e, f) straight channel; j, h i)

sinusoidal channel; j, k, l) small void; m, n, o) 5-member ring (5-MR); p, q, r) 6-member-ring (6-MR). Back numbers: ^{1}H NMR, and blue numbers: ^{27}Al NMR.

2.4.2 ^{1}H NMR and ^{27}Al NMR of different EFAL species stabilized at the intersection.

We examined various cationic EFAL species such as AlO^{+}, $Al(OH)^{2+}$ and $Al(OH)_2^{+}$ and neutral species such as $Al(OH)_3$ and AlOOH. The EFAL species exhibit a preference to connect to the AlO_4^{-} tetrahedral moiety. [21] **Figure 7** shows the optimized structures of EFAL species formed at the intersection and their corresponding chemical shifts. In structures 1, 2, 3, 4, and 5a, the EFAL coordinated to the tetrahedral framework at T12. The EFAL $Al(OH)_3$ can either form cluster like structure 5b or coordinated to AlO_4^{-} tetrahedral moiety like structure 5a. The ^{1}H chemical shifts of OH associated with EFAL are in the range of 0.7-2.3 ppm.

Now we discuss ^{27}Al NMR of EFAL species. While the ^{27}Al chemical shift of AlO^{4-} moieties are still in the range of tetrahedral Al, it's worth noting that the ^{27}Al NMR chemical shifts of EFAL exhibit a wider range of values, varying from 58 to102 ppm. This range is dependent on the specific of EFAL structures, such as binding partner and coordination numbers with the framework. Structure 1-4 in **Figure 7**, EFAL AlO^{+}, $Al(OH)^{2+}$ and $Al(OH)_2^{+}$ and AlOOH are bonded with the two framework oxygen atoms neighboring the tetrahedral Al sites, and the Al-Al distance are similar, about 2.8 Å. In structure 5a, where $Al(OH)_3$ EFAL is present, it only connects with on framework oxygen, resulting in a longer Al-Al distance of 3.1 Å. This indicates a weaker interaction with the framework in comparison to the other EFAL species.

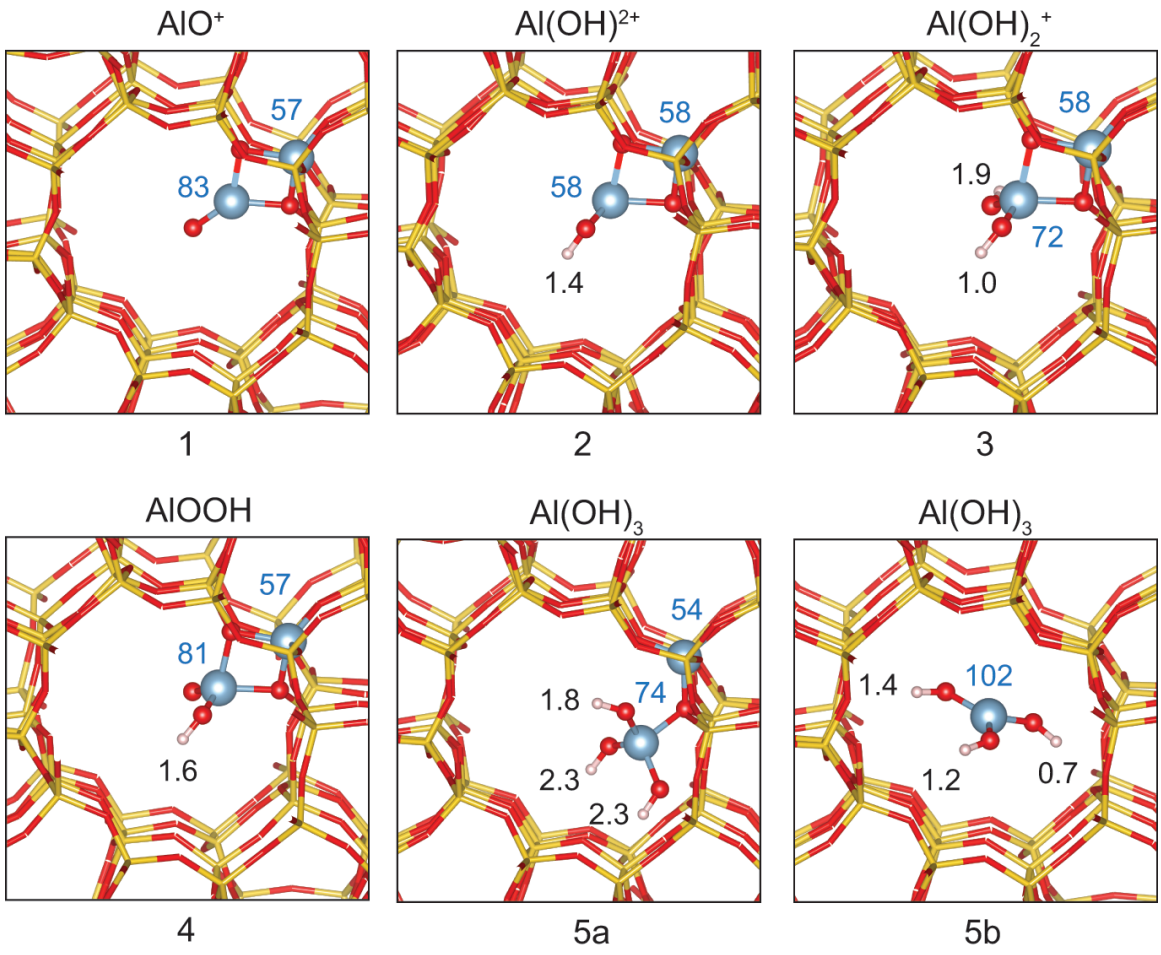


Figure 7. Optimized structures of various EFAl species stabilized at the intersection and their DFT-calculated ^{1}H NMR and ^{2}7Al NMR.

The observation of tri-coordinated Al signal is impossible using traditional ^{27}Al NMR due to its huge quadrupolar (C_q >30) and low density. [53] Prior studies used trimethylphosphine oxide (TMPO) and tri-butylphosphine oxide (TBPO) as probe molecules to evaluate the acid strength of sites containing tri-coordinated Al species. [53, 54] In this situation, DFT calculations can provide a powerful tool for exploring the ^{27}Al NMR values of tri-coordinated Al species. The ^{27}Al chemical shift of cluster Al(OH)^3 in 5b is shown at 102 ppm. Furthermore, computed quadrupolar (C_q) values for Al atoms in structure 5b are roughly 13 and 32 MHz for the tri-coordinated EFAL and

tetrahedral framework Al, respectively. The C_q is sensitive to symmetry of Al sites, the more unsymmetrical environment the larger the C_q. In this case, C_q of Al(III) is nearly three time larger than Al(IV) due to the fact that geometry of Al(III) is obviously less symmetric than Al(IV).

2.4.3 ^{1}H NMR and ^{27}Al NMR of synergistic site BAS/EFAL species

When BAS locates in spatial proximity with an EFAL species, they form synergistic sites, which have been shown to result in considerably stronger catalytic activity. [18, 25, 31, 32] Recently, we revealed the broad peak at 12-15 ppm rose from BAS located in proximity with EFAL $Al(OH)_2^+$ and $Al(OH)_3$, and the signal 2.8 ppm are attributed to hydroxyl groups associated with EFAL. [30] These two signals can be introduced by hydrothermal treatment and can be washed by AFHS, indicating they are associated with EFAL species. To examine the BAS/EFAL synergies, we choose T7-11 (the left term represents the tetrahedral site, which is substituted with Al and the second term denotes the neighboring tetrahedral site of silicon atom connected to the protonated oxygen) as BAS. We also assessed how the distances between BAS and EFAL impact to chemical shifts by considering T11 and T12 for location of EFAL.

Figure 8 displays the optimized geometries of a variety of BAS/EFAL, in which EFAL locate at T12, which is separated from BAS by two Si linking atoms and do not have direct interaction (e.g., hydrogen bond) with BAS. Structure 10b comprise a BAS and an adjacent EFAL $Al(OH)_3$ cluster without direct interaction, stabilizing at the intersection. One can see that the ^{1}H and ^{27}Al chemical shifts in these synergistic sites remain almost the same with isolated BAS and isolated EFAL. On the other hand, in structures 6b, 7b, 8b, 9b, 10c, and 10d (**Figure 9**), the EFALs are positioned at T11, which is only one Si linking atom away from the BAS at T7. In these synergistic sites, the BAS forms hydrogen bonds with oxygen atoms which are associated with

EFAL species. These hydrogen bonds shift the ^{1}H NMR of the BAS to 15-18 ppm. The phenomena happen in the same way with the higher value of BAS at 5-MR/6-MR, in which the hydrogen bonds result in the deshielding of the proton.

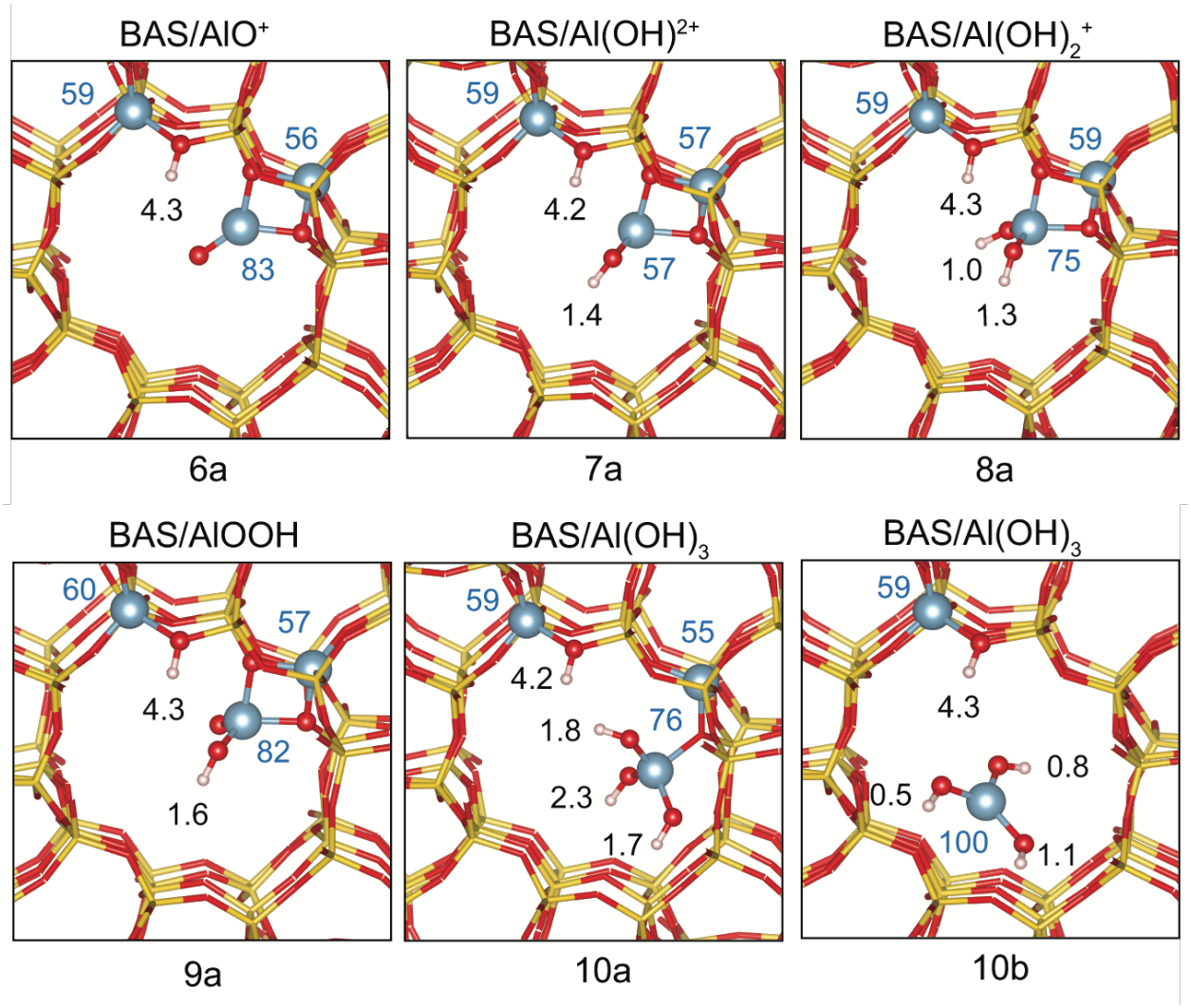


Figure 8. Optimized structures of a variety of synergistic sites BAS/EFAL species stabilized at the intersection and their DFT-calculated ^{1}H NMR and ^{27}Al NMR. In these synergistic sites, EFAL and BAS do not form hydrogen bonds. Black numbers: ^{1}H NMR and blue numbers: ^{27}Al NMR.

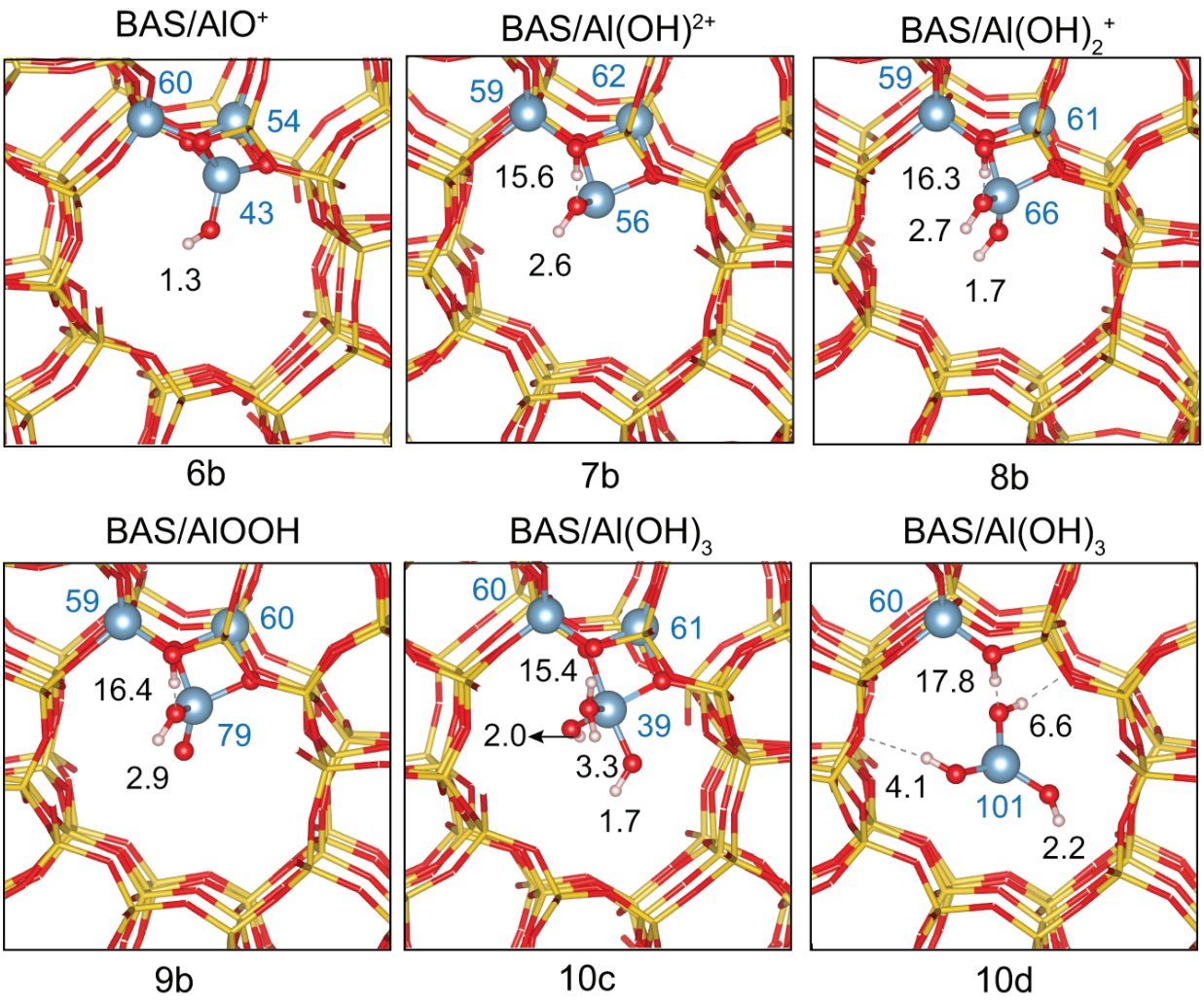


Figure 9. Optimized structures of a variety of synergistic sites BAS/EFAL species stabilized at the intersection and their DFT-calculated ^{1}H NMR and ^{27}Al NMR. In these synergistic sites, BASs form hydrogen bonds with EFAL. Black numbers: ^{1}H NMR and blue numbers: ^{27}Al NMR.

To check this effect in sinusoidal and straight channels, we calculated chemical shifts for synergistic site BAS/Al(OH)$_2^+$ in both channel geometries, as shown in **Figure 9**. The ^{1}H chemical shifts of BAS in synergistic sites 8c and 8d resonate at values of 13.1 and 11.3 ppm. The computed chemical shifts of synergistic sites in straight and sinusoidal channels are comparable to those

located at the intersection. Generally, the hydrogen bonds forming between proton and oxygen atoms belonging to EFAL species can shift the ^{1}H chemical shift of proton to 11-18 ppm. The broad range of ^{1}H chemical shifts reflect the different degrees of hydrogen bonds, which depend on the relative distances of O-H bonds.

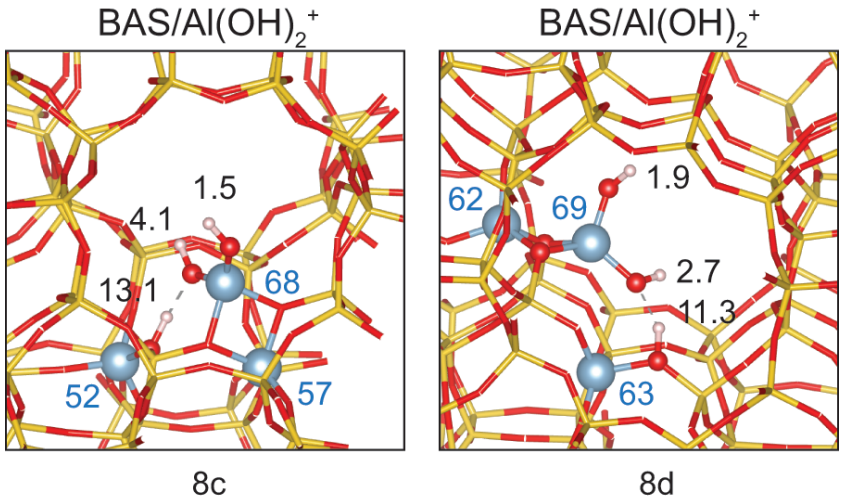


Figure 10. Optimized structures of synergistic sites BAS/Al(OH)$_2^+$ and their DFT-calculated ^{1}H NMR and $^{2}7Al$ NMR stabilized at 8c) sinusoidal channel; 8d) straight channel.

In addition, some ^{1}H NMR of OH groups can be shifted to 6.6 ppm, shown in structure 10d. Even though this chemical shift is in the same range with BAS at 5-MR/6-MR, the difference is that it belongs to the EFAL species and can be removed by chemical wash AHFS. These results provide confirmation of the assertion that the 5-7 ppm signal is attributed to both framework and extra framework species. Generally, we show that the BAS formed hydrogen bonds with different EFAL species will resonate at higher values of chemical shift, at 11-18 ppm. The ^{1}H chemical shifts of OH groups in EFAL are mainly in the range of 1.7-3 ppm while some can be much higher at about 6.6 ppm. In experiments, many coupling signals of two Al in proximity were observed

using 2-dimensional ^{27}Al NMR[39]. They can be the signals of BAS/BAS or BAS/EFAL. Particularly, the signals (55, 87) and (55, 114) ppm were reported in dealuminated HY zeolite, however, the structures corresponding to these signals do not know yet. [39] From **Figure 4**, even though the NMR signals in HY zeolite can be slightly different from that in H-ZSM5 zeolite, it's capable of assigning the (55, 87) ppm to the synergistic site between BAS and EFAl (AlO^+, $Al(OH)_2^+$ or AlOOH) while the signal (55, 114) could arise from the BAS/$Al(OH)_3$ synergies.

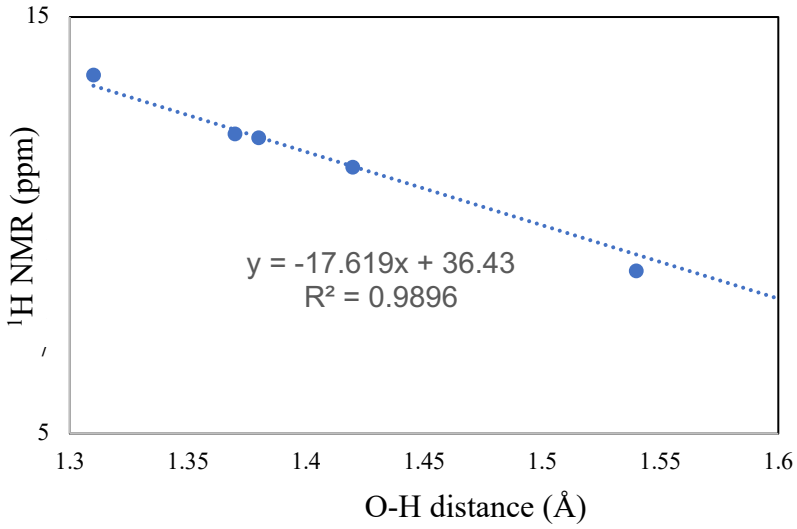


Figure 11. Linear relationship between the O-H bond distance and ^{1}H NMR of proton in synergistic sites.

2.4.4 ^{1}H NMR and ^{27}Al NMR of synergistic site BAS/EFAL species

The hydrolysis of framework atoms in zeolite is a well-known phenomenon that occurs upon exposure to water. [18, 25, 31-33, 55] The extent of dealumination under hydrothermal treatment is proportional to the duration, temperature, and partial pressure of steam, resulting in the coexistence of framework Al, PFAL, and EAFL species in zeolite treated with water. [18, 25, 33, 42, 50, 56] In the previous section, we discussed ^{1}H and ^{27}Al NMR of different BAS/EFAL synergistic sites. Here,

we propose the synergistic sites generated from BAS and PFAL species, which can coexist as means of enhancing catalytic performances in benzene hydride transfer and n-hexane cracking reactions. [35]

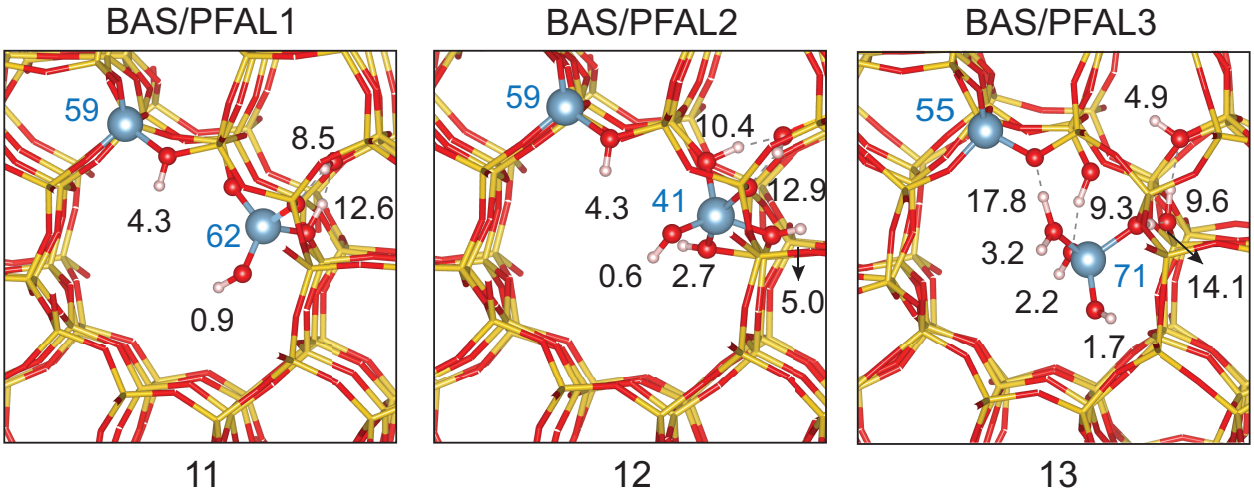


Figure 12. Optimized structures of synergistic sites BAS/PFAL species stabilized at the intersection and their DFT-calculated ^{1}H NMR and ^{27}Al NMR.

While EFAL species have been studied extensively, the structures and catalytic functions of PFAL species remain a current topic of interest. Within the PFAL species, there are three sub-species: PFAL1, PFAL2, and PFAL3, which are each described as incorporating one, two and three water molecules. The detailed chemical shifts for BAS/PFAL synergistic sites are given in **Figure 7.** One can see **in Figure 7** that PFAL1 and PFAL3 are four-coordinated Al species while PFAL2 refer to be penta-coordinated Al species. Most of the silanol Si(OH) groups in silanol nest are in high deshielding environments, at 8-13 ppm, owing to the hydrogen bond generated with framework oxygen atoms. The silanol groups having no direct interaction with oxygen atoms have ^{1}H chemical shift at about 5 ppm. The ^{1}H NMR of OH groups on PFAL varies between 1-3 ppm. In the case of BAS/PFAL1 and BAS/PFAL2 (structure 11 and 12), there is no direct interaction

between PFAL and BAS, and the ^{1}H chemical shift of BAS at T7 remains unchanged. The chemical shifts of the A(IV)-2 are 62 and 71 ppm in the cases of four-coordinated PFAL1, PFAL3, respectively, which agree with observation for ^{27}Al chemical shift of H-ZSM5 after hydrothermal treatment. [35, 42] Supporting for this result, Ravi et al.[56] reported the ^{27}Al NMR signal at 63 ppm for irreversible Al-OH species appearing from calcination in static air. The mentioned irreversible Al-OH species in should be PFAL species. The five-coordinated Al in PFAL2 species was characterized by a chemical shift of 40 ppm. These results explain for the expansion of ^{27}Al NMR peak in experimental spectra under steaming treatment. [35, 42]

2.4 Conclusions

The theoretical calculations provide precise assignments of NMR spectra for acid sites and their surrounding in zeolites. Thus, by combining DFT-calculation with experimental NMR results, the quantitative information on different active sites (IBAS and synergistic sites) in zeolites may be accurately determined. Further calculations can provide the acid properties and catalytic performances over zeolites. The assigned structures of various protonic and aluminum species are shown in Tables 1 and 2, respectively. The ^{1}H NMR of IBAS are sensitive to their locations and local environments. The well-known signal 4.2 - 4.5 ppm is attributed to BAS at the intersection and void channels. The smaller confinement can lead to higher values of ^{1}H NMR of BAS. The broad signal 5-9 ppm, partially washed by AHFS, is assigned for framework BAS at 5-MR/6-MR or silanol groups in silanol nests for the first time. It is noteworthy that the broad signal 11-18 ppm rise from BAS forming hydrogen bonds with adjacent EFAL/PFAL species. Furthermore, the ^{27}Al NMR values are sensitive to coordination numbers and binding ligands. The ^{27}Al chemical shifts of tetrahedral framework Al are in the range of 53-63 ppm, consistent with experimental

observation. For different EFAL and PFAL species, the chemical shift values are in the broad range of 55-85 ppm, that is rational to the expansion of aluminum peak up to 85 ppm for steamed samples. We believe that the synergistic models of BAS/EFAL and BAS/PFAL presented in this work are useful for studying numerous hydrocarbon reactions in zeolite under hydrothermal treatment.

Table 1. Assignments for protonic species in H-ZSM zeolite by combining experimental spectroscopy and DFT calculations.

Assignment of species	**^{1}H NMR (ppm)**	**Framework**	**Extra-framework**	**Partially coordinated framework**
BAS at the intersection and straight channels	4.2-4.5	v	x	x
BAS at the sinusoidal channels and small voids	4.6 – 5.3	v	x	x
BAS at 5MR/6-MR	5.0 -8.5	v		
OH associated with EFAL/PFAL	0.7 – 3.2	x	v	v
BAS forming hydrogen bond with EFAL/PFAL	11.0 – 18.0	v	Maybe (when EFAL delocalize proton)	Maybe (when PFAL delocalize proton)

Silanol groups in silanol nests (without hydrogen bond with oxygen framework)	5.0			
Silanol groups in silanol nests (with hydrogen bond with oxygen framework	8.5 – 14.1			

Table 2. Assignments for aluminum species in H-ZSM zeolite by combining experimental spectroscopy and DFT calculations

Assignment of species	^{27}Al NMR (ppm)	Framework	Extra-framework	Partially coordinated framework
Tetrahedral BAS	53 - 63	v	maybe	unlikely
Tetrahedral EFAL	54 - 69	v	likely	
Tri-coordinated EFAL	100	v	x	x
Tetrahedral PFAL	62 - 71	maybe	maybe	v
Five-coordinated PFAL	41	x	x	v

CHAPTER 3: Dynamical behaviors of aluminum species in H-ZSM-5 zeolite

3.1 Abstract

Extensive discussions and debates have taken place regarding the impact of EFAL species on industrially important reactions including alkane cracking. It has been widely acknowledged that water treatments can influence the framework aluminum sites, leading to modifications in activity. Although various hypotheses have been proposed, the prevailing theory suggests that the synergistic effect between BAS and EFAL, when in proximity, enhances the catalytic activity of zeolite. This section proposes possible mechanisms for the formation of BAS/EFAL and BAS/PFAL synergistic sites, with the latter arising from the incomplete hydrolysis of Al in pairs. Furthermore, an explanation is provided for a recently reported pulsed water technique, which introduces very small amounts of water into zeolite catalysts, thereby enhancing the rate of n-hexane reaction without compromising crystallinity or the total BAS density. In addition, thermodynamic cycles connecting different EFAL complexes were constructed, involving elementary steps such as hydration/dehydration and proton transfer. The calculations and discussions of sodium titration to various active sites situated in different locations were also conducted. Examining the sodium titration behavior is crucial in analyzing the performance of each individual active site. Understanding the thermodynamic characteristics of aluminum species in zeolites through these findings is significant for the rational design of various hydrocarbon reactions catalyzed by zeolites.

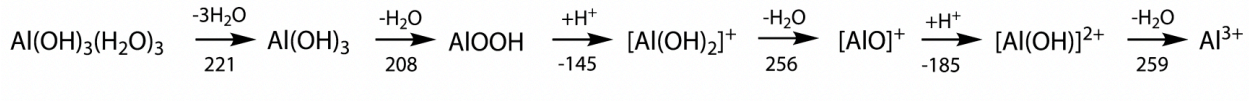
3.2 Introduction

The zeolite is subjected to a steam treatment to create mesopores by partially breaking the Al-O and Si-O bonds within the framework through hydrolysis. [57, 58] This process removes some Al or Si species from the framework, which results in the formation of EFAL and silanol nest. The silanol nest is characterized by the presence of four hydroxyl groups surrounding the tetrahedral void. [59] There is a vast amount of literature devoted to the generation and thorough investigation of extra-framework aluminum (EFAL) species located inside cavities.

Several studies have reported that the process of dealumination can occur at specific sites. [60, 61] The dealumination behavior of a zeolite is also influenced by the structure of the zeolite frameworks. [60] For instance, zeolite beta possesses a 12-ring pore system that extends in three dimensions, making its framework highly flexible. On the other hand, zeolite mordenite has one-dimensional 12-ring pore system, while ZSM-5 has a three 10-ring pore system. Compared to beta zeolite, both structures exhibit less flexibility, which makes the process of dealumination more challenging. Additionally, dealumination could be impacted by the number of T-atoms present in four-ring, as the tension in smaller rings is greater. [60] Van Geem et al. [61] investigated the dealumination of mordenite and substantiated this finding. They arrived at the conclusion that the dealumination atoms in mordenite are distributed randomly throughout all T-sites, and that the initial stage of dealumination occurred in four-rings, based on their MAS NMR and FTIR analyses. This finding was supported by Muller et. al., [60] who noted that among the four zeolite types (mordenite, ZSM-5, ferrierite, and beta zeolite), beta zeolite is the easiest to dealuminate. The beta zeolite structure contains 75% of tetrahedral sites in four-rings, with half of them linked to two four-ring, making it easier to dealuminate. ZSM-5 zeolite is highly stable towards dealumination, owing to the low percentage (17%) of tetrahedral sites in four-ring, and they can be synthesized

with varying Si/Al ratios and crystal sizes without complications. Ferrierite exhibits the most stable due to the fact that all tetrahedral sites are bound to five-rings, rather than four-rings.

Chen et al. [42] provided evidence to demonstrate that even at room temperature exposure of ZSM-5 to moisture can result in the hydrolysis of the Al framework atoms. Likewise, Agostini et al. [62] reported that the dealumination occurs at moderate temperature (450-500 K) during the steaming of NH4-Y. Shilaghi et al. [17] reported the comprehensive mechanism of dealumination in **Scheme 1**, along with the reported free energy of the dealumination process for different zeolite frameworks. The free energy profile of dealumination in ZSM-5 is presented in **Figure 13**. The incomplete hydrolysis leads to PFAL, while the EFAL generated from dealumination can transform to different forms, shown in **Scheme 2.** [22] The most preferred EFAL species are oxoaluminum ions, such as AlO^+, $Al(OH)^{2+}$, $Al(OH)^{2+}$ and Al^{3+}, and some neutral species including $Al(OH)_3$ and AlOOH. [20, 21, 34]



Scheme 2. Conversion of different EFAL species in Faujasite zeolite. The energy is reported in kJ/mol. This figure is taken from ref. [22]

In this section, to propose for the formation of BAS/PFAL synergistic sites, we adopted the dealumination mechanism in Silaghi's paper.

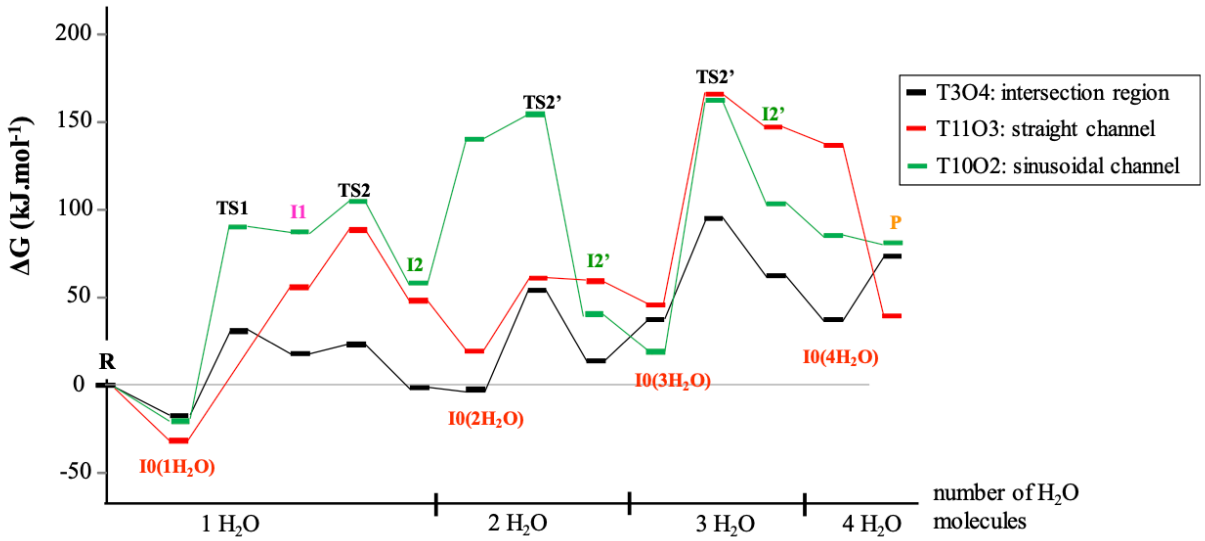


Figure 13. The free energy profiles for the favored dealumination route of T3O4, T10O2, and T11O3 sites in H-MFI, which involved four water molecules and resulted in the formation of EFAL $Al(OH)_3H_2O$, were analyzed at a temperature of 450 K. The calculation of free energy utilized a physisorbed water reference. [17]

Furthermore, Liu et. al. [22] predicted that at high temperatures during zeolite activation, the EFAL species are mobile and would arrange themselves into clusters with more than one Al center and that these resulting tri- and tetranuclear clusters would be preferentially stabilized inside the small sodalite cages of faujasite due to a favorable coordination and charge-compensation environment. The cationic clusters, with multiple charges, strongly enhance the protolytic propane cracking activity of vicinal supercage BAS. Recently, Pham et. al. [25] reported the different change of BAS density and activity on hexane cracking reactions under two distinct water treatments (pulsing and steaming). During the pulsing treatment, the catalysts were subjected to multiple 2.85 µmol water pulses spaced qt 10-minute intervals. In **Figure 14b**, Pham and coworkers observed

that there was no measurable loss in BAS density when HZSM5-11.5 was treated with sequential pulses of water. The potential for BAS losses is expected to be even less significant for catalysts with lower BAS density. The catalytic activity under pulsing treatment remained constant after reaching its maximum level. On the other hand, the catalysts were exposed to continuous steaming conditions where a consistent stream of water vapor passed across them for a prolonged time. This steaming initially resulted in an enhancement of catalytic activity, but it eventually decreased after prolonged exposure to steam (**Figure 14a**). Pham and coworkers showed that both methods of treatment increased the catalysts' activity by approximately 3-3.5 times. It was hypothesized that the activity increase was due to the generation of synergistic sites. In the pulsed experiment, it is likely that the catalytic activity would increase until the maximum number of BAS/EFAL synergistic sites is achieved. In contrast, when a continuous steam treatment is used, the number of BAS decreases due to the dealumination process.

The mechanism for forming synergistic sites varies across different water treatment conditions, as observed. Further discussion on this mechanism can be found in the results and discussions section of this chapter.

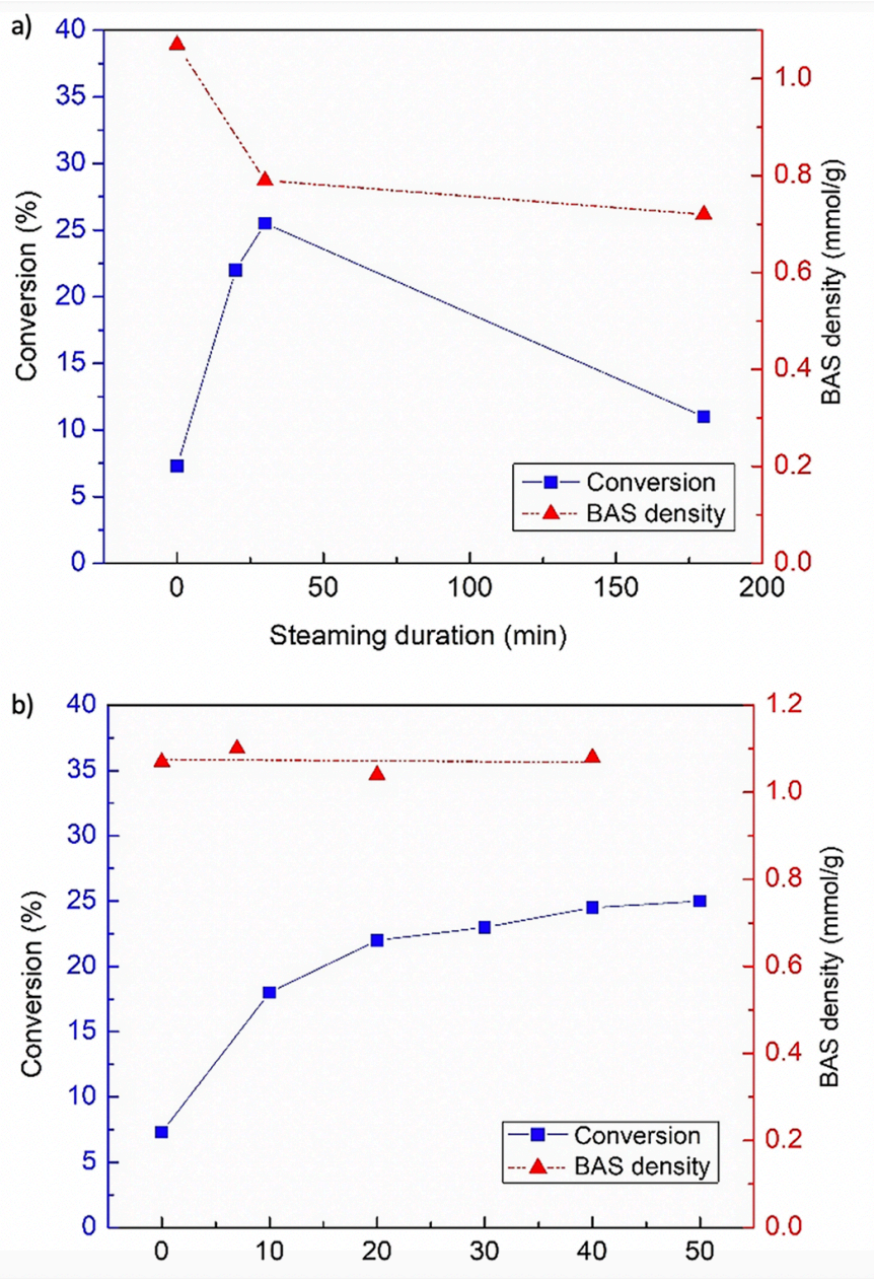


Figure 14. Conversion of n-hexane cracking on HZSM5-11.5 catalyst and BAS density (determined by IPA-TPD) as a function of (a) steaming duration (catalyst was treated by steaming) and (b) number of pulses of water (catalyst was treated by pulsing water). The steam treatment was at 480 °C in both cases, with a water partial pressure of 18.6 kPa either in a continuous manner or in pulses. Reaction conditions: T = 480 °C, PnC6 = 4.5 kPa with 0.48 µmol of n-hexane injected in each pulse, 5 mg amount

of catalyst. The BAS densities of HZSM5-11.5-0.5hS and HZSM5-11.5-3hS are 0.79 and 0.73 mmol/g, respectively. This figure is taken from ref. [25]

3.1.1 Nudged Elastic Band (NEB) Method

The description of the NEB method is detailed in ref. [63] Briefly, the NEB method [64] is a commonly utilized approach for studying reactions and diffusion events on solid surfaces. This method aims to locate a reaction pathway that links two local energy minima on the potential energy surface corresponding to the reactant and product states. To present this pathway, a discrete representation is employed, whereby N_{im-2} intermediates images (i.e., molecular configurations) are generated between the reactant and product configurations. The accuracy of the method depends on the number of intermediate images used, as the method converges to the pathway when N_{im-2} is sufficiently large. An iterative optimization algorithm is utilized to adjust the intermediate images to the nearest reaction path, as is typical for numerical methods that rely on discretization of continuous variables. A gradient-based optimization method is employed alongside an NEB force to enhance effectiveness, while the endpoint configurations remain unchanged. The NEB force is comprised of the sum of two forces: a spring force (F^{sp}) that only operates along the path, and a perpendicular component of the atomic force ($F^{\perp}$) acting on the atoms. The perpendicular force is:

$$\mathrm{F}_{\mathrm{i}}^{\perp} = \mathrm{F}_{\mathrm{i}} - (\mathrm{F}_{\mathrm{i}} \cdot \hat{\tau}_{\mathrm{i}})\hat{\tau}_{\mathrm{i}} \qquad (3.1)$$

where $\hat{\tau}_i$ is the local tangent at image I along the path. To determine the unit tangenet, the "upwind tangent" technique is employed. [65] This approach normalized the line segment between an image and its adjacent image with higher energy. In instances where the image lies at an energy extremum along the path, the unit tangent is calculated as the normalized energy-weighted average of the two line segments that connect the image to its neighboring images. To regulate the distribution of images along the path, a spring force acting tangentially to the path is utilized. The spring force is:

$$F_i^{sp,\parallel} = (k_i^{sp}|R_{i+1} - R_i| \; - \; k_{i-1}^{sp}|R_i \; - \; R_{i-1}|\hat{\tau}_i \tag{3.2}$$

where R_i represents the 3M-dimensional atom coordinate vector for image i. The length of the path segment corresponding to image I can be defined as the distance between R_{i+1} and R_i denoted as $|R_{i+1} - R_i|$. The spring constant k_i^{sp}, is utilized to determine the stiffness of the spring interaction for this particular path segment.

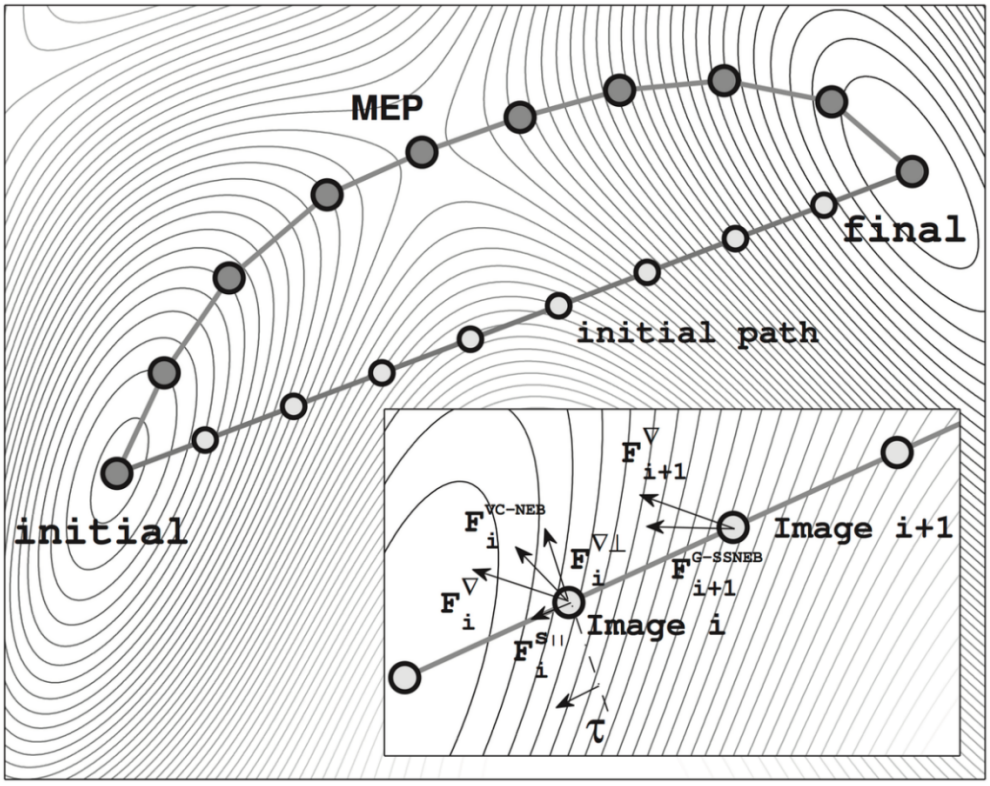


Figure 15. This figure from Jonsson et. al. illustrates an example NEB simulation that shows the creation of initial images (represented by a line with white circles) along a direct reaction path from the initial state to the final state, and the optimized final path (represented by a line with gray circles) passing through the MEP of that specific reaction. [63]

In NEB calculations, the shape and position of the reaction pathway are modified only by the atomic forces acting perpendicular to it, which makes it necessary to project the atomic forces base on a reliable estimate of the local tangent to the pathway. This approximation of the tangent is a critical aspect of NEB calculations. Additionally, the distribution of images along the pathway is regulated through the use of harmonic springs that connect adjacent images, but only the component of the spring force that acts tangentially to the path is taken into account. If this

distribution control is not applied, the images tend to slide toward the energy minima at the fixed endpoints. The NEB method is typically implemented with a uniform spring constant for all springs, resulting in an evenly spaced distribution of images along the path. However, it is possible to assign different spring constants to different pairs of images to achieve a specific distribution.

The energy maximum along the path of minimum potential energy, known as MEP, corresponds to the saddle point energy that provides that activation energy barrier. This quantity is crucial in estimating the transition state using harmonic transition state theory. A depiction of this process is shown in **Figure 13**.

3.1.2 Climbing Image Nudged Elastic Band (CI-NEB) Method

To obtain an estimate of the activation energy for a reaction path, the highest energy point is identified, which corresponds to a first-order saddle point on the energy surface and represents the bottleneck of the transition between the reactant and product states. In NEB calculations, this point is treated differently to improve its accuracy. [66] This highest energy image is referred to as the climbing image (CI) and is subject to an uphill force parallel to the path and a downhill force perpendicular to the path, resulting from the atomic forces acting on the atoms. This approach, known as climbing image NEB (CI-NEB), enables a more precise location of the highest energy point. The spring forces, however, do not affect the CI. [67]

Initiating the CI from a NEB calculation that is only partially converged could be advantageous in practice. This means that when a given criterion, such as $\max|F^{\perp}| < \varepsilon_{CI}$, is fulfilled. This process can be carried out at the beginning of the NEB calculation, and during optimization, the CI can shift from one image to another, particularly when a higher energy image than the current CI emerges. This approach guarantees that the CI will converge to the highest

energy maximum along the path. Given that the reaction path (reference pathway) is primarily required to achieve a good tangent estimate for the CI, tighter convergence thresholds are often applied to the CI than to the other images.

In some cases, it's unlikely for the images to optimize directly to the saddle point; therefore, extra images need to be computed between the two highest energy images. If the saddle point is not found, we will carry out dimer calculation, which is presented in next section. Consequently, determining the activation barriers can become highly demanding in terms of computational resources.

3.1.3 Dimer method

The description of the dimer method is detailed in ref. [68] This method for locating saddle points involves utilizing a pair of images or replicas that depict the differently. This pair of images is referred to as the "dimer". To determine saddle points, the algorithm requires moving the "dimer" in an uphill direction on the potential energy surface, starting from the neighborhood of the initial state's potential energy minimum and ascending towards the saddle point. During this ascent, the "dimer" is also rotated to the potential energy's lowest curvature mode at its current position. Voter introduced a technique in his hyperdynamics method that allows for the estimation of the lowest curvature mode at a specific point without the need to evaluate the Hessian matrix. This approach is utilized to develop a repulsive bias potential that speeds up the classical dynamics of activated processes. [69]

For certain uncomplicated systems, to avoid doubling the computational cost by introducing more images, the dimer method can be employed instead, which offers a relatively straightforward means of locating the saddle point.

3.1.4 Thermodynamic Quantities and Frequencies

Quantum chemical programs calculate energies for stationary nuclei in isolation at 0 K. To compare these values with experimental results, additional terms are required to account for zero-point vibrations and the finite temperature of the experiment. Assuming ideal gas behavior based on statistical mechanics, the difference in enthalpy between 0 K and z non-zero temperature T can be expressed as follows:

$$\Delta H(T) = H_{trans}(T) + H_{rot}(T) + \Delta H_{vib}(T) + RT \tag{3.3}$$

The correction terms for enthalpy due to translational, rotational, and vibrational changes, as well as the zero-point energy, can be expressed as follow: [70]

$$H_{trans}(T) = (3/2)RT \tag{3.3}$$

$$H_{rot}(T) = (3/2)RT \quad (RT \text{ for a linear molecule }) \tag{3.4}$$

$$\Delta H_{vib}(T) = H_{vib}(T) - H_{vib}(0) = N_0 h \sum_i \frac{\nu_i}{(e^{h\nu_i/kT} - 1)} \tag{3.5}$$

$$H_{vib}(0) = \frac{1}{2} h \sum_i \nu_i \tag{3.6}$$

Equations (3.6) and (3.7) involve summations over all I normal modes. Furthermore, assuming ideal gas behavior, one can use statistical mechanics to derive equations for the total entropy, as expressed in ref. [70]

$$\mathrm{S(T)} = \mathrm{S_{trans}\,(T)} + \mathrm{S_{rot}\,(T)} + \mathrm{S_{vib}(T)} + \mathrm{S_{el}} - \mathrm{nR[ln(nN_0) - 1]} \tag{3.7}$$

Equation (3.9) - (3.12) can be utilized to calculate the entropic contributions from translation, rotation, vibration, and electronic effects:

$$S_{\mathrm{trans}}\,(T) = nR\left\{\frac{3}{2} + \ln\left[\left(\frac{2\pi MkT}{2}\right)^{3/2}\left(\frac{nRT}{P}\right)\right]\right\} \tag{3.8}$$

$$\mathrm{S_{rot}(T)} = \mathrm{nR}\left\{\frac{3}{2} + \ln\left[\frac{(\pi \mathrm{v_A v_B v_C})^{1/2}}{\mathrm{s}}\right]\right\} \tag{3.9}$$

$$\mathrm{S_{vib}(T)} = \mathrm{nR}\sum_i \{(u_i e^{u_i} - 1)^{-1} - ln(1 - e^{-u_i})\} \tag{3.10}$$

$$\mathrm{S_{el}} = \mathrm{nR\ln\omega_{el}} \tag{3.11}$$

The following notations are employed in Equations (3.3) to (3.11):

R = ideal gas constant

n = mole of molecules

N_0 = Avogadro's number

M = mass of molecule

h =Planck's constant

k = Boltzmann's constant

T = temperature

P = pressure

$I_A, I_{B,} I_C =$ principle moment of inertia

$v_A, v_B, v_C = \frac{h^2}{8\pi I_A kT}$, etc.

$v_i =$ vibrational frequencies

$\omega_{el} =$ electronic ground state degeneracy

$s =$ symmetry number

$u_i = \frac{hv_i}{kT}$

To compute thermodynamic properties, it is necessary to determine the vibrational frequencies of a molecule. Let's consider a molecule with N atoms and assume that the nuclei are situated near equilibrium positions. To obtain the mass-weighted Cartesian displacements for nucleus A, we take the difference between the displaced and equilibrium Cartesian coordinates and multiply them by $\sqrt{M_A}$, where M_A represents the mass of the nucleus in question. Assuming the harmonic approximation and limiting the energy expansion around the equilibrium position to the second order, we can express the energy in terms of X = (X_1, …, X_N) as:

$$\mathrm{E} = (1/2)\mathrm{X}^{\dagger}\mathrm{QX} \tag{3.12}$$

Here, we have chosen the energy scale such that E = 0 when the molecule is at equilibrium. The matrix Q, which has dimensions of 3N x 3N, can be expressed as:

$$Q = \left.\frac{\partial^2 E}{\partial \boldsymbol{X} \partial \boldsymbol{X}'}\right|_{\boldsymbol{X}=\boldsymbol{X}'=0} \tag{3.13}$$

With the normal modes of the system are obtained through the eigenvectors, q, while the mass-weighted force constants are obtained from the corresponding eigenvalues, k_α. In the

harmonic approximation, the vibrational frequencies denoted as ω, are related to the mass-weighted force constant via:

$$\omega_\alpha = \sqrt{k_\alpha} \tag{3.14}$$

Certain quantum chemical programs are capable of calculating the second derivative of the energy with respect to nuclear displacements analytically. However, in instances where analytic derivatives are not feasible, but analytic gradients are computable, the second derivative term in Equation (3.14) is replaced by a finite difference, and the resulting frequencies are deemed to be computed numerically.

$$Q = \frac{\partial^2 E}{\partial X \partial X'} | X = X' = 0 \approx \frac{\Delta(\partial E/\partial X)|X = 0}{\Delta X'} \tag{3.15}$$

In this Chapter, we will utilize the equations mentioned above, in conjunction with the analytically calculated frequencies, to ascertain the entropic and enthalpic contributions to the Gibbs free energy for hydrolysis reactions of Al framework atoms.

3.1.5 Quasi-rigid rotor harmonic oscillator approximation (q-RRHO) method

Simulating zeolitic reactions presents an added difficulty in the form of calculating enthalpies. Quantum chemical calculations can offer molecular-level insights into the interactions between zeolites and adsorbates in addition to modeling the energetic variations and dynamics of significant reactions taking place within the channels and pores of zeolite catalysts. Calculating vibrational energy levels is a challenging task that involves modeling the full-dimensional potential energy surface, which can be computationally infeasible for most systems except for those that are extremely small.

When dealing with basic molecular structures, it is typical to approach the issue by making assumptions about how vibrational modes operate, treating them as harmonic oscillators. This allows for the determination of energy levels and thermodynamic functions via a normal mode analysis that relies on second-order derivatives of the electronic potential energy surface. [71] Unfortunately, when studying the translational and rotational degrees of freedom of a molecule in zeolites, their potential energy surfaces are often highly anharmonic, meaning that the simple harmonic oscillator model cannot realistically account for their behavior.

Various techniques have been employed to address the limitations of the harmonic oscillator approximation, such as anharmonic sampling along normal mode coordinates, [72] frequency down scaling, and interpolation approaches. The quasi-rigid rotor harmonic oscillator (q-RRHO) approximation proposed by Grimme[73] is perhaps the most commonly used alternative to the harmonic oscillator approximation, which involves replacing the entropies of low-frequency normal modes with a semi-empirical interpolation between rigid rotor and harmonic oscillator entropies, utilizing the Head-Gordon[74] damping function v.

To compute the correction term, a modified approach based on the q-RRHO method was employed. In this method, the vibrational energy contribution is characterized by a below specific description:

$$\mathrm{V} = \sum_{\mathrm{i}} \mathrm{V}_{\mathrm{i}}^{\text{quasi-RRHO}} \tag{3.16}$$

$$= \sum_{\mathrm{i}} \left[\omega(\mathrm{v_i}) \times \mathrm{V}_{\mathrm{i}}^{\mathrm{RRHO}} + \left(1 - \omega(\mathrm{v_i})\right) \times \frac{1}{2}\mathrm{RT} \right] \tag{3.17}$$

$$\omega(\mathrm{v_i} = \frac{1}{1 + (\mathrm{v_0}/\mathrm{v_i})^4} \tag{3.18}$$

in which R is gas constant, T is absolute temperature, and v_i is the frequency of vibrational mode i, v_0 is taken as 100 cm^{-1}, and V_i^{RRHO} is the vibrational energy contribution of mode i represented by q-RRHO:

$$V_i^{RRHO} = \frac{1}{2} N_A h v_i + RT\left(\frac{h v_i}{kT}\right)\frac{e^{-h v_i/kT}}{(1 - e^{-h v_i/kT})} \quad (3.19)$$

where k is the Boltzmann constant, h is the Planck constant and N_A is the Avogadro constant.

In this Chapter, the q-RRHO method is employed to calculate the entropic and enthalpic contribution to Gibb free energy of framework Al atoms' hydrolysis.

3.3 Computational details

Zeolite model geometry: The unit cell of ZMS-5 consists of 96 T atoms (T = Si, Al) and 192 oxygen atoms. The proton and aluminum chemical shifts of twenty-four BAS at different locations including intersection, straight channel, sinusoidal channel, small void, 5-member ring (5-MR) and 6-member-ring (6-MR) were computed. Ghorbanpour et al. [44] reported that BAS at T7 was the most thermodynamically stable. Additionally, Gounder et al. [52] revealed that the most stable Al substitutions are positioned close to T12, which locate at the intersection. Based on these findings and the Löwenstein's rule, the site pairs are set at T7-T12, which are separated by 2 Si linking atoms. The process of dealumination was computed according to the mechanism reported by Silaghi et al. [17]

Computations: Our DFT calculations were performed using Vienna ab initio simulation package (VASP). [45] Perdew-Burke-Ernzerhof (PBE)[46] generalized gradient approximation (GGA) was used for the exchange-correlation potential. DFT-D3 semi-empirical method[47] was employed

to account for the van der Waals interaction. The system was fully relaxed with a kinetic cutoff of 400 eV. A single Γ point in the first Brillouin zone was used for atomic relaxation. The lattice parameters of unit cell zeolite were set accordingly to the experimental study: a = 20.078 Å, b = 19.894 Å and c = 13.372 Å, as in our previous studies. [25, 30, 35, 48] The geometry optimizations continued until the force excess on each atom was smaller than 0.02 eV/Å. The self-consistent field electronic calculations were assumed to cone 10^{-6} eV.

The climbing image nudged elastic band method, which uses 8 images, was employed to identify transition states (TS) and calculate activation barriers. The force threshold for NEB calculations was set to 0.02 eV/Å. Transitions states were confirmed by verifying the presence of a single imaginary frequency through vibrational analysis. The Gibbs free energy was calculated using the harmonic oscillator model at 500ºC. The energy threshold for vibrational frequency calculations was set at 10^{-8} eV. The low-frequency vibrations resulting from free rotation and translations were addressed using the quasi-rigid rotor harmonic oscillator approximation (qRRHO) developed by Grimme[73] and Head-Gordon. [75] Additionally, the pressure of gas-phase systems in Gibbs free energy calculations was carried out at 1 atm.

3.4 Results and discussions

3.4.1 The formation of BAS/PFAL from a site pair via incomplete hydrolysis

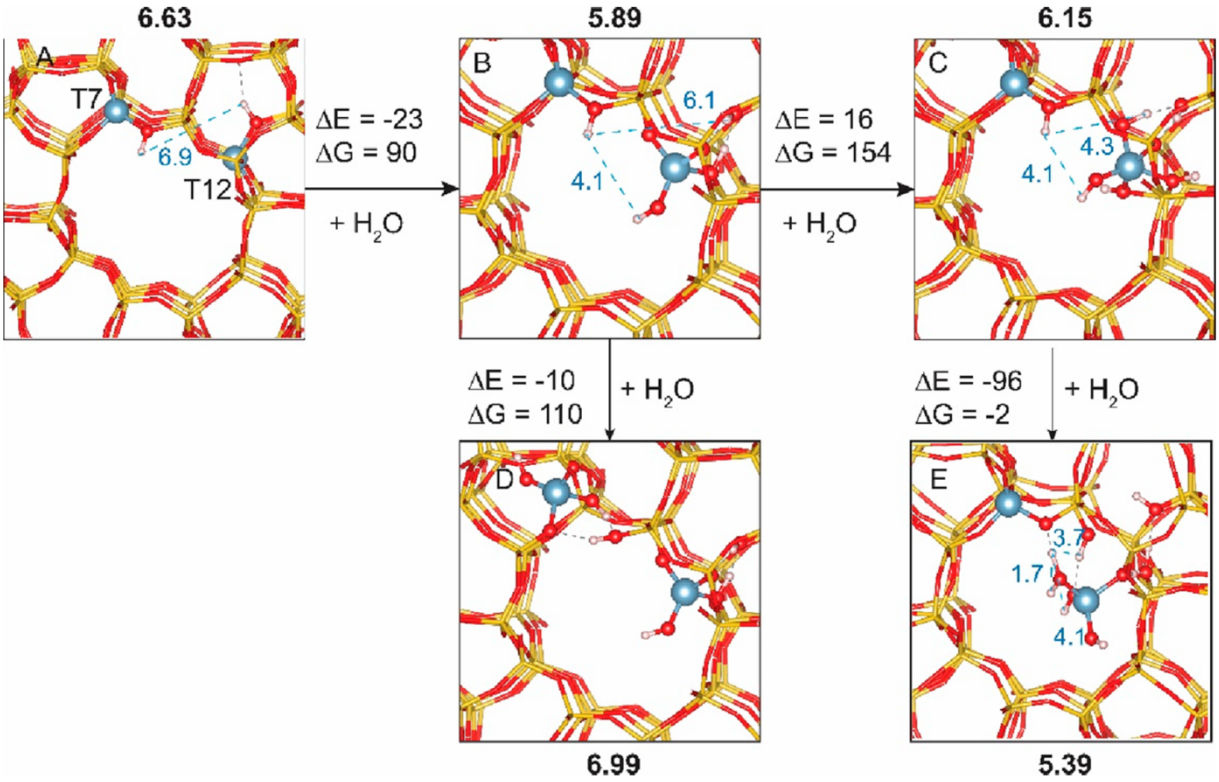


Figure 16. DFT calculations for model hydrolysis of (a) an Al(IV)-1/Al(IV)-1 pair, resulting in (b) an Al(IV)-1/Al(IV)-2 framework pair. Possible structures resulting from additional hydrolysis are shown in (c−e). Total energies and free energies are calculated with an ideal gas reference for water. The Al−Al internuclear distances (in Å) are shown in bold text above or below each structure, and H−H distances are shown in blue within each figure. [36]

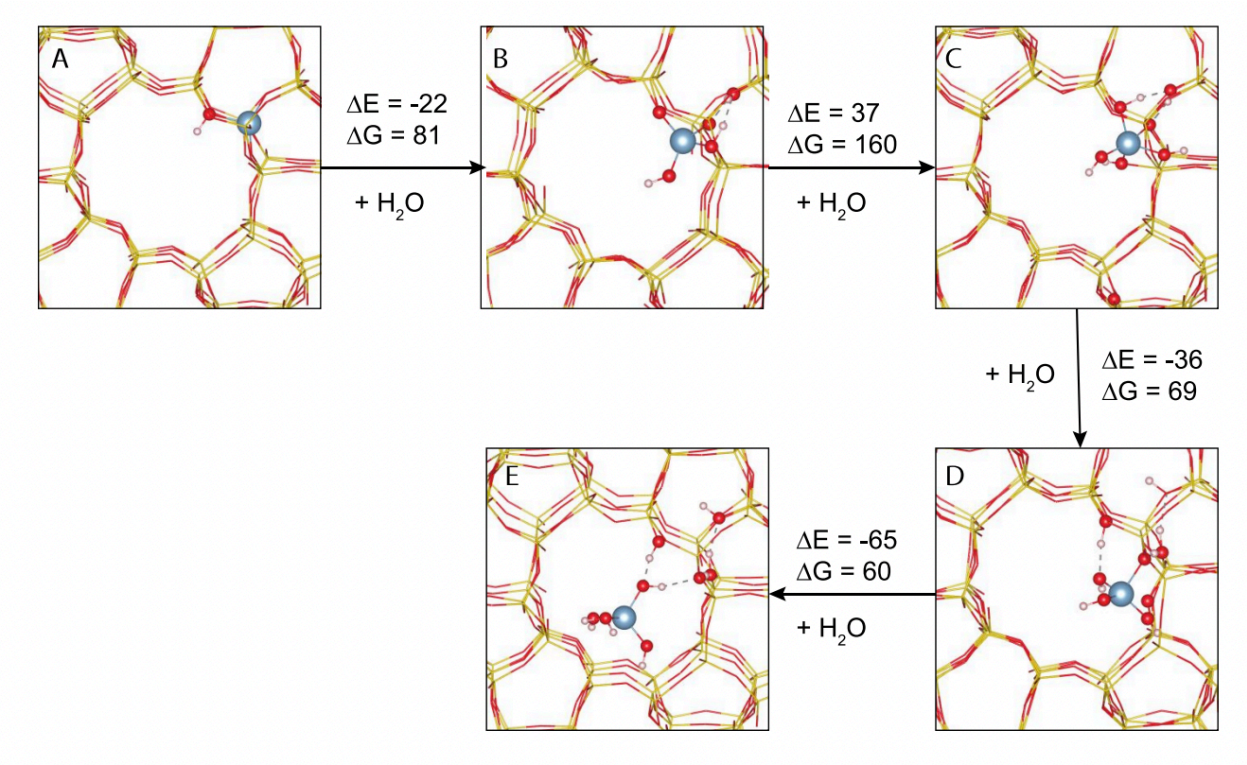


Figure 17. Total energies and Gibbs free energies (gas phase water as reference) for the hydrolysis of isolated BAS at T12. [36]

This section provides the idea of generations of BAS/PFAL synergistic sites, which have been reported to increase the activity in n-hexane cracking and benzene hydride transfer. Additionally, the section introduced two different Al(IV) species: Al(IV)-1, which is the tetrahedral Al in the framework BAS, and Al(IV)-2, which represents PFAL. When exposed to water vapor, the BAS site pair at T7-T12 (as shown in **Figure 16A**) undergoes a reaction with water, wherein one of the two framework sites reacts with water. The hydrolysis reaction begins with the T12 sites reacting with water, resulting in the formation of PFAL (as shown in **Figure 16B**), which is an exothermic step with a ΔE of -23 kJ/mol and a ΔG of 90 kJ/mol. Our calculations indicate that the T12 site is disturbed by water and displaced towards the intersection. This leads to a reduction in the atomic distance between an Al(IV)-1/Al(IV)-1 from 6.63 to 5.98 Å for a

Al(IV)-1/ Al(IV)-2 pair, along with a concomitant decrease in the nearest H-H distance to 4.1 Å, and a decrease in the other H-H distance from 6.7 to 6.1 Å. After the first Al-O bond is broken, the second water molecule may continue to attack the T12 site to break the second Al-O bond and form the configuration shown in **Figure 16C**, or it may react with the BAS at T7 to form the structure shown in **Figure 16D**, with the free energy of approximately 154 and 110 kJ/mol, respectively. The Gibbs free energies of the initial hydrolysis step in T7 and T12 exhibit similarity. The variance in ΔG between the first and second hydrolysis step of T12 can be attributed to the structure of Al that is partially hydrolyzed and depicted in configuration 16C. In this configuration, the coordination number of Al site is five instead of four, although no Al(V) signals were found in the samples discussed in this study except for those that underwent severe steaming. The partially coordinated Al in the configuration (**Figure 16E**) can continue to undergo a reaction with water molecules for form a structure (**Figure 16E**) with ΔG of -2 kJ/mol. In **Figure 16E**, the Al site at T12 coordinates with only one oxygen framework atom after reacting with three water molecules. This results in a partially coordinated Al that approaches the BAS at T7, causing proton delocalization and reducing the Al-Al distance to 5.39 Å. **Figure 17** compares these calculations with an isolated T12 site without neighboring Al sites. The reported free energy values are moderately higher than literature values due to the use of gas phase as reference instead of physisorbed water. During the first and second hydrolysis steps, the adjacent BAS at T7 does not affect the hydrolysis of T12. However, in the third step, the partially hydrolyzed Al species interact with the proton at T7 (as shown in **Figure 16E**), resulting in a more energy favorable process when a site pair is present.

Based on the preceding discussions, it can be inferred that the initiation of BAS/PFAL sites occurs through BAS site pairs. Consequently, the density of BAS in the sample and the conditions of water treatment are two key determinants that influence the formation of BAS/PFAL sites.

3.4.2 The formation of BAS/FAL from via migration of EFAL

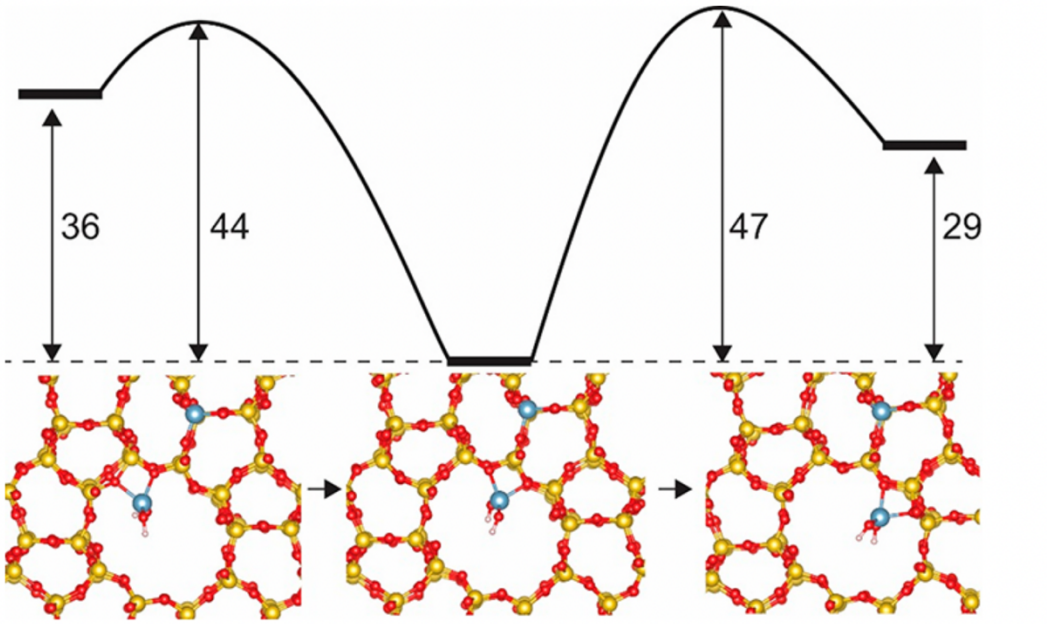


Figure 18. DFT calculations of migration of $Al(OH)_2^+$ at the intersection. The colors blue, yallo, red, and white represent Al, Si, O, and H atoms, respectively. The energy units are given in kJ/mol. [25]

In order to explore how extra-framework $Al(OH)_2^+$ migrates between different locations in MFI zeolites, the activation barriers and reaction energies of its migration at the intersection were calculated (as depicted in Figure 18). The electrostatic interactions between the positively charged EFAL and the negative charge surrounding the framework Al have an impact on the migration of $Al(OH)_2^+$ at the intersection. Specifically, the framework Al generates an electrostatic force that

attracts the $Al(OH)_2^+$ cation towards it. Despite the presence of a spacer in the form of a -O-Si-O- unit between them in the structure depicted in **Figure 18**, the $Al(OH)_2^+$ cation prefers to position itself facing the framework Al. The movement of $Al(OH)_2^+$ to a location that is further away from the framework Al by one additional unit of -O-Si-O- requires an input of 29-36 kJ/mol of energy and has an activation barrier of 44-47 kJ/mol. This indicates that $Al(OH)_2^+$ located far from the framework Al is compelled to migrate towards it due to enhanced stability, but with a moderate activation barrier of 9-18 kJ/mol. The study also investigated the migration of $Al(OH)_2^+$ in the sinusoidal channel, where the ion was intentionally placed far from the framework Al to minimize electrostatic interactions. The findings show that the migration of $Al(OH)_2^+$ from a T12 site to a T3 site in the sinusoidal channel is a thermodynamically neutral process with a ΔE value of only 2 kJ/mol and an activation energy of 23 kJ/mol. Consequently, the calculations suggest that the migration barrier of the EFAL cation is moderate and the migration process is driven toward the framework Al species. Moreover, barriers associated with moving away from local minima to more favorably stabilized positions, usually pairs of sites, are in line with experimentally observed barriers.

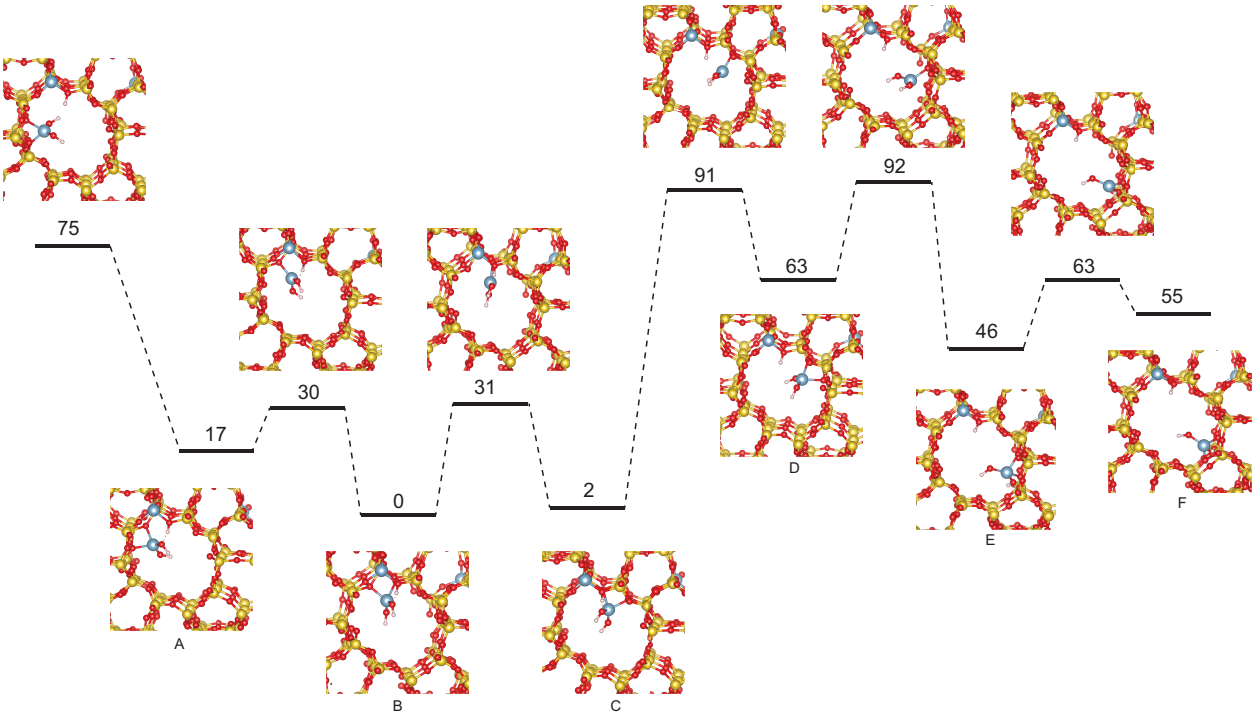


Figure 19. The role of BAS in stabilizing the EFAL species.

Another factor that can influence the generation of highly active sites is the ability of zeolite structure to stabilize EFAL species, which is hypothetically related to the H bond networks in zeolites. In this model, the AlO^{4-} moiety was set far away from the migration region to compensate for the cationic EFAL, which would not influence the migration of the EFAL $Al(OH)_2$. The EFAL $Al(OH)_2^+$ started at the location that is 4 Si linking T sites away from BAS at T7, then it moved toward the BAS in counterclockwise in 10-MR. The results have shown that when the EFAL species form H bonds with BAS, the energies of the systems are significantly lower than the others. Within 3 positions (**Figure 19, A-C**) in which H bonds between BAS and EFAL are formed, the activation energy for the migration of EFAL species is not profound, about 30 kJ/mol. However, the migration of these EFAL species further away from the BAS requires relatively high energy barriers (58-89 kJ/mol). This result suggests that once H bonds are formed, it is difficult for EFAL species to migrate further. In other words, EFAL species will be trapped nearby BAS by H bonds.

As investigated in DPE, these BAS/EFAL sites do not correspond to the higher activity for alkane cracking reaction. However, if there is another neighboring BAS, it is likely that these EFAL species can synergistically enhance the activity of that BAS. This will explain why pairs of BAS are required for the generation of highly active sites. This result will explain the previous results about the generation of synergistic sites during pulsing treatment. [25] Furthermore, when EFAL species are far from the BAS and their movements are not influenced by the presence of BAS, the energy barrier to migrate from (E) to (F) via the TS-6 is not sufficiently high. This suggests that the migration of EFAL species inside the zeolite pores is typically not an energy-demanding process in the absence of framework Al atoms. While Al-Al pairs are important for the formation of synergistic sites because the H bond can help to kinetically trap the EFAL species.

3.4.3 Energy for sodium exchange

Table 3. Reaction Energies for Cation Exchange of Different Active Sites and Their Corresponding Locations. [31]

type of sites	reaction	position	T-site	ΔE (kJ/mol)
IBAS	ZH → ZNa	intersection	T7-11	−2
		straight	T5-1	−10
		sinusoidal	T9-9	−12
BAS-EFAL	ZH → ZNa	intersection	T7-T12	−45
		straight	T5-T12	−66
		sinusoidal	T5-T7	−88
BAS−BAS	$Z_2H_2 \rightarrow Z_2HNa$	intersection	T7-T3	−4
	$Z_2HNa \rightarrow Z_2Na_2$			−18
	$Z_2H_2 \rightarrow Z_2HNa$	straight	T1-T12	−13
	$Z_2HNa \rightarrow Z_2Na_2$			+3
	$Z_2H_2 \rightarrow Z_2HNa$	sinusoidal	T5-T7	+14
	$Z_2HNa \rightarrow Z_2Na_2$			−12

In this section, we employed DFT computations to elucidate the differences in the sodium exchange affinities, as presented in Table 3 and Figure 20. The ZSM-5 zeolite features a three-dimensional network of channels, including straight (5.3 × 5.6 Å) and sinusoidal (5.1 × 5.5 Å) pores, with cavity regions where these channels intersect having a diameter of 6.36 Å. [9] The straight and sinusoidal micropores exhibit comparable pore sizes and are more restricted than the intersection cages. The sodium titration outcomes indicate that the IBAS at the straight and sinusoidal channels is somewhat more favorable than that at the intersections, which can be attributed to the confinement effect. Previous research has shown that sodium cations tend to remain in the smaller voids of CHA zeolites. [26] The vàiations in sodium exchange åe not

substantial, being under 10 kJ/mol in the ẽamnied locations. This implies that the substitution of sodium is determined by both thermodynamic prediction and availability of sites. We then compare the sodium substitutions of IBAS and synergistic sites at the intersection, the sodium titration of IBAS rises by 2 kJ/mol, while the synergistic site rises by 45 kJ/mol. This suggests that replacing the BAS proton in a synergistic site with sodium is much more straightforward than doing the same with IBAS. **Table 2** illustrates the sodium titration at straight and sinusoidal pores for synergistic site, which may be attributed to the development of several bonds between Na+ and the oxygen in $Al(OH)_2^+$. As a result, when introducing sodium to zeolite in a partial manner, the BAS protons in synergistic sites are the first to be replaced by sodium cations, thereby removing the synergistic sites in zeolites. Moreover, there is a strong inclination for Na^+ titration to synergistic sites of different locations, and this follows the same pattern as the isolated acid center.

When BAS in pairs, the distance between them affects the behavior of sodium titrations by influencing the interactions between sodium and protons, as well as the interactions between sodium atoms during the first and second sodium titrations of protons in pairs. The coordination number of sodium with framework oxygen atoms is also determined by the local environment and void confinement, as demonstrated in **Figure 20 g-k**. The exchange of both Al atoms in pairs is thermodynamically favorable at the intersection. Previous research has shown that the energy required for sodium titration of BAS in pairs in CHA zeolites varies by 50 kJ/mol depending on the location of these paired sites. Moreover, the configuration where both the proton and the sodium cation occupy the same 6-MR in CHA zeolite has the highest energy, with the proton pointing out of the ring place. This suggests that there is a repulsion between the proton and the sodium exchange when their locations are sufficiently close. [26]

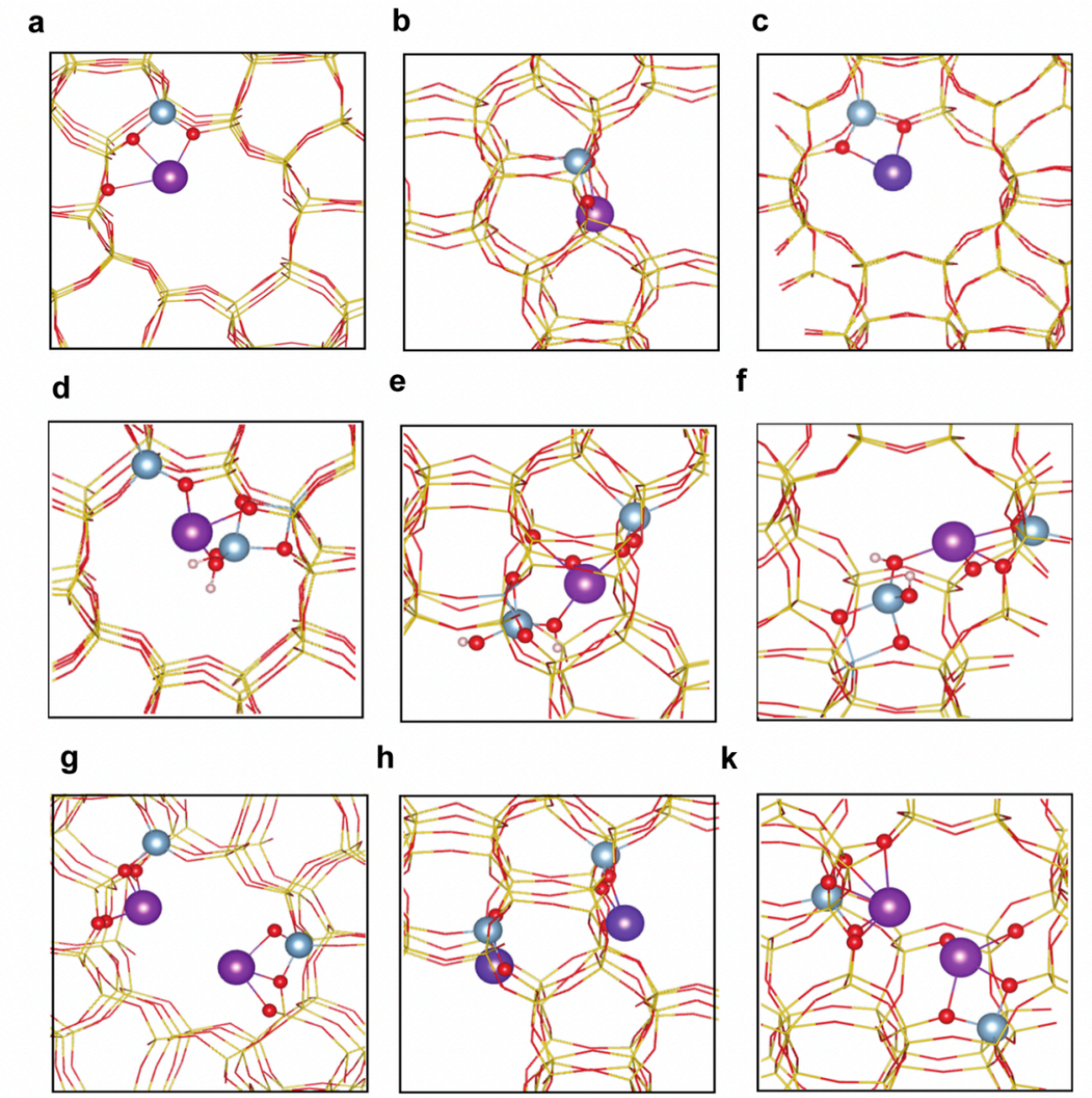


Figure 20. Calculated structures of Na+ titrated to (a) IBAS at the intersection, (b) IBAS in the straight channel, (c) IBAS in the sinusoidal channel, (d) BAS/EFAL at the intersection, (e) BAS/EFAL at the straight channel, and (f) BAS/EFAL in the sinusoidal channel; calculated structures of Na+ titrated to (g) paired BAS at the intersection (h) paired BAS in the straight channel and (k) paired BAS at the sinusoidal channel. Na, Al, O, Si, and H atoms are colored purple, cyan, red, yellow, and white, respectively. [31]

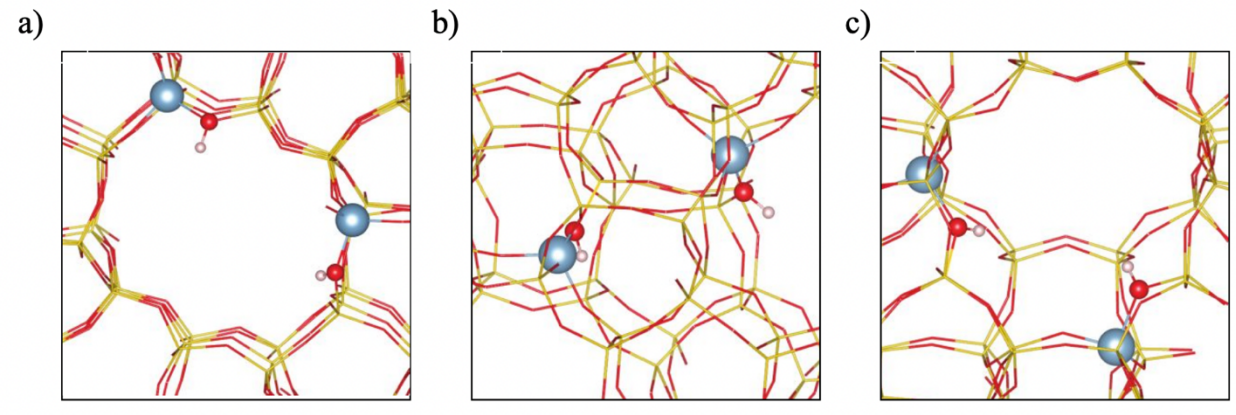


Figure 21. The optimized structures of paired BAS at a) intersection, b) straight channel, c) sinusoidal channel. [31]

Table 2 shows that the initial titrations to paired BAS are exothermic in the straight channels and the intersections because the protons relax into larger voids, resulting in no repulsion upon the first titration. However, in straight channels, the repulsion caused by the short distance between Al atoms and the larger size of two sodium cations makes the second exchange of Al sites less thermodynamically favorable. In ZSM-5, the distribution of tetrahedral sites is generally tighter in the straight channels than in the intersection and sinusoidal channels. Therefore, the Al distance in the Al-O(Si-O)$_2$-Al sequence in straight channels are shorter than those in the intersection and sinusoidal channels. In sinusoidal channels, two protons pointed to smaller void, resulting in the first sodium titration to paired BAS being 14 kJ/mol endothermic due to the repulsion between the proton and sodium. After the second sodium titration in the sinusoidal channels, two sodium cations relax to positions further from each other to reduce the repulsion and form multiple bonds with framework oxygen. This makes the second titration 26 kJ/mol easier than the first one. Zeolite samples with higher BAS density will have more Al in pair at the intersections, which will be favorably titrated by sodium.

3.4.4 Interconversion of different EFAL species in ZSM-5

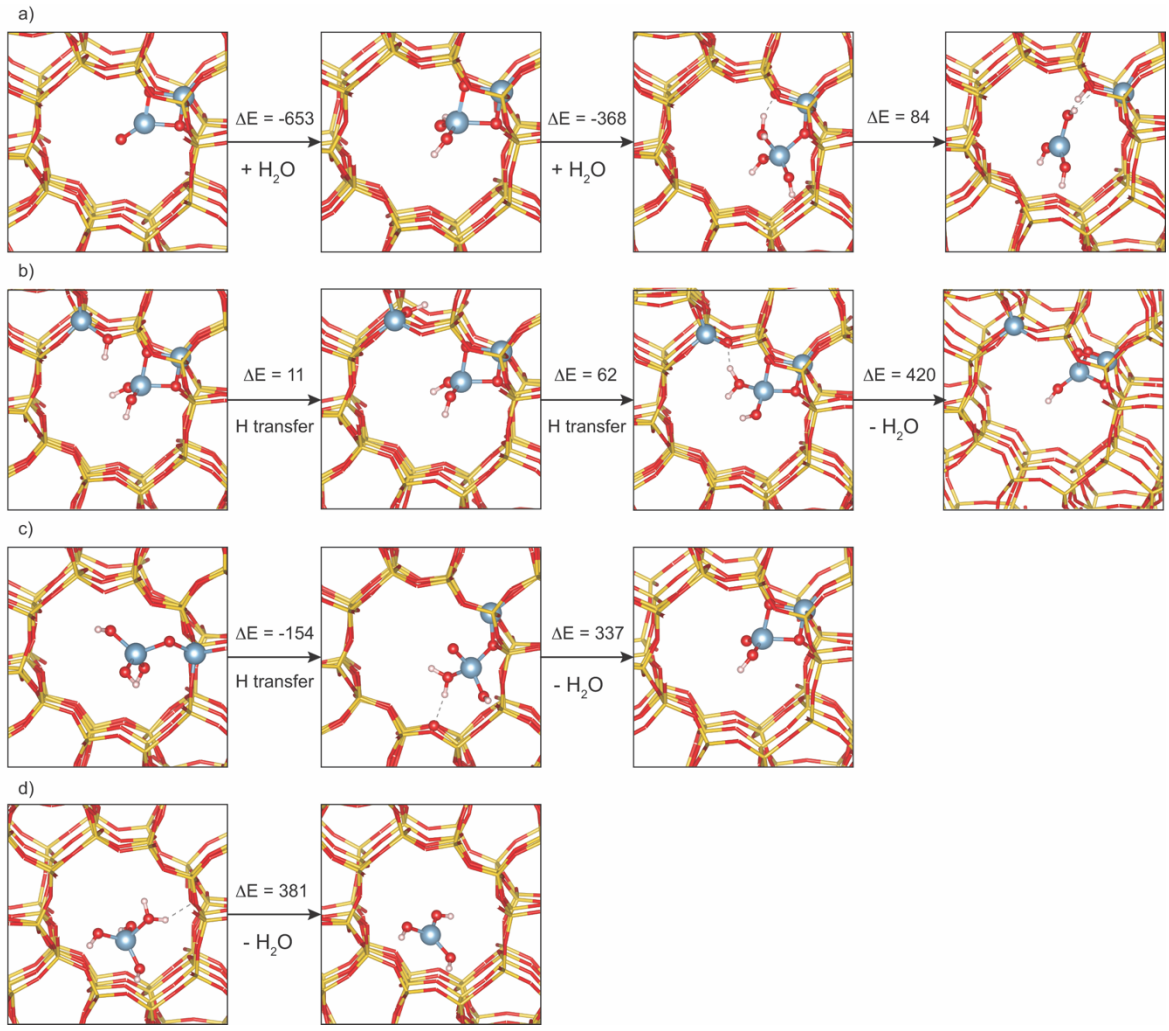


Figure 22. Transformation of EFAL species in ZSM-5.

Various potential EFAL complexes can transform into one another through elementary steps such as hydration/dehydration and proton transfer. The energetics of these transformations are summarized in **Figure 22**. Particularly, in **Figure 22a**, the hydration of AlO^+ to $Al(OH)_2^+$ is a highly exothermic process (ΔE = -653 kJ/mol). Both EFALs AlO^+ and $Al(OH)_2^+$ connect to the AlO_4^- tetrahedral moiety through two framework oxygen atoms. Further hydration of $Al(OH)_2^+$ reduces the total energy of the system by 368 kJ/mol, resulting in the formation of $Al(OH)_2H_2O$,

where Al is coordinated with only one framework oxygen atom. The deprotonation of $Al(OH)_2H_2O$ to AlO_4^- moiety creates a BAS and EFAL $Al(OH)_3$, requiring an energy input of 84 kJ/mol. In **Figure 22b**, the transformation of the $Al(OH)_2^+$ to a less stable AlO^+ species occurs through proton transfer and the elimination of water. Dehydration of $Al(OH)_3$ to form a hypothetical AlOOH loss energy of 183 kJ/mol, involving an intramolecular proton transfer and subsequent desorption of water (**Figure 22c**). The water desorption step is exothermic by 337 kJ/mol, which is partially compensated by the proton transfer step with ΔE = -154 kJ/mol. In an earlier section, we discussed the hydrolysis of the Al framework, where the fully hydrolyzed process results in the formation of EFAL $Al(OH)_3H_2O$ and silanol nest. Direct dehydration of $Al(OH)_3H_2O$ to $Al(OH)_3$ requires a reaction energy of 381 kJ/mol (**Figure 22d**). These data indicate that thermodynamics, rather than kinetics, play a predominant role in regulating the interconversion of EFALs within the zeolite pores.

CHATER 4: Catalytic Role of EFAL and PFAL species in Alkane Reaction

4.1 Abstract

The purpose of this study is to investigate the influence of extra-framework aluminum (EFAL) and partially-coordinated framework aluminum (PFAL) on intrinsic acid strength and on the monomolecular cracking and dehydrogenation reactions of propane. Periodic DFT calculation was used to model synergistic sites created from Brønsted acid sites (BAS) and various EFAL ($Al(OH)^{2+}$, $Al(OH)_2^{+}$, AlOOH and $Al(OH)_3$) as well as PFAL. The computed deprotonation energy (DPE) suggests that the possible active sites in H-ZSM5 zeolite include isolated BAS (IBAS) and synergistic sites, which have no direct interaction (e.g., hydrogen bond) with the proton. The quasi-rigid rotor harmonic oscillator approximation (qRRHO) was used to calculate thermodynamic (enthalpy, entropy, and Gibb free energy) changes for adsorption states and transition states. The activation enthalpies of monomolecular propane cracking on all proposed synergistic sites are significantly lower compared to that of IBAS. Decrease in activation enthalpies of propane cracking with presence of EFAL and PFAL species are driven by higher charge transfer. The transition state of cracking happens early in the reaction coordinate and strongly interacts with the active site; thus, the activation entropy is less affected by the local environment. For the hydrogenation reaction (a later transition state), activation enthalpies are insignificantly changed, while activation entropy decrease with the presence of EFAL and PFAL because the confinement strongly influences on the freedom of movement of this more-like product transition state. Concurrently, propane in pulse reaction supported by catalysts containing

different concentrations of EFAL and PFAL shows a consistent trend on activation enthalpy with DFT results.

4.2 Introduction

The H-ZSM-5 zeolite is a widely employed catalyst in industrially important reactions, particularly cracking, isomerization, alkylation, fluid catalytic cracking (FCC) and methanol-to-propylene (MTP)[76]. The catalytic properties of zeolites arise from the strong acidic protons, positioned at BASs, which compensate for the negative charge on the framework, resulting from the substitution of Si^{4+} with Al^{3+}. Apart from BAS, the extraction of these Al^{3+} from the framework under hydrothermal treatments may create PFAL and EFAL species in the zeolite structure, which provide interesting catalytic properties. [18, 34, 35, 42, 58, 77] The partial hydrolysis of framework aluminum generates tetrahedral PFAL species, which can be the precursors of EFAL. The PFAL species partially coordinate to the zeolite framework through lattice oxygen atoms and hydroxyl groups being other coordinations. [18, 19, 50]

The positive catalytic effects of EFAL and PFAL species have been investigated before. [22, 25, 32, 35, 78] For example, Zhang et al.[32] observed roughly 50 and 80 times higher reaction rates of n-pentane cracking and dehydrogenation over steamed H-ZSM5 zeolite. They proposed that the enhanced catalytic activity was attributed to the stabilization of cracking and dehydrogenation transition states via increasing activation entropy. As reported by Liu et al.[22], the cationic multi-nuclear EFAL cluster inside the sodalite cages of FAU zeolite compensated the negative charge of the deprotonated zeolite framework, which stabilized the ion-pair transition state and decreased the activation barrier of propane cracking.

Despite several proposed scenarios for the catalytic effects of EFAL species, the synergistic effects generated by the EFAL and PFAL species in proximity of BAS seem to be responsible for the zeolite activity enhancement. [32, 38, 78-80] Zeolite structure, which plays a vital role in its catalytic performance, is very sensitive to the treatment conditions. Therefore, it is reasonable to attribute

the different explanations for the synergistic effects to the unalike structures formed under different treatments. The synergistic sites in zeolite can be formed as BAS/EFAL or BAS/PFAL. EFAL, on the other hand, can be in a cationic form such as AlO^+, $Al(OH)^{2+}$, $Al(OH)_2^+$ or a neutral cluster like $Al(OH)_x(H_2O)_y$. [22, 33] These EFAL species can transform among themselves via hydration/dehydration and proton transfer. [22] They may also migrate along the zeolite framework. [22, 25] In our earlier study, we showed two tetrahedral aluminum sites, coexisting in H-ZSM5 zeolite, which were observed via ultrahigh field two-dimensional (2D) ^{27}Al magnetic nuclear resonance (NMR).[35] The first tetrahedral aluminum Al(IV)-I is the well-known framework BAS while the second tetrahedral aluminum Al(IV)-2 population can be controlled by post-synthetic treatment. The Al(IV)-2 sites were attributed from incompletely hydrolyzed framework aluminum and the ^{27}Al NMR signal at early state of hydrolysis (one water incorporated) ranged from 65 to 74 ppm.[35] It was also shown that these sites significantly enhanced the catalytic activity of n-hexane cracking and benzene hydride-transfer reactions. [35] Ravi et al.[56] supported these findings, noting that the formation of the second tetrahedral aluminum sites only occurred at 550 ^oC during calculation, which corresponded to a decrease in the population of BAS. These sites were shown to be coordinated to the hydroxyl groups and irreversible upon ammonium exchange. Recently, we have constructed various structures of synergistic sites at different locations (intersection, straight and sinusoidal channels) by combining computed ^{27}Al NMR and ^1H NMR and experimental spectra (Chapter 2). The unlike catalytic effect of individual EFAL and PFAL species remains less understood.

Inspired by prior studies, we investigated the intrinsic acidity and catalytic performance of various active sites within H-ZSM5. Our analysis included the calculations of deprotonation energy (DPE) for a range of active sites, including isolated BAS and synergistic sites, in other to

assess the influence of nearby EFAL and PFAL in the intrinsic acid strength of the proton. Propane cracking and dehydrogenation reactions were employed as probe reactions. To gain a better understanding of the effect of individual EFAL and PFAL species on the catalytic performance of BAS, we provided calculated enthalpy, entropy, and Gibbs free energy profiles for all active sites.

4.3 Computational details

All periodic DFT calculations were performed using VASP[81] version 5.4.1. The PBE generalized gradient approximation (GGA)[82] exchange-correlation potential was used with the projector augmented wave (PAW)[83] method. The energy cutoff was set at 400 eV during the structure optimization process, and the DFT-D3[84] method was employed to account for dispersive interactions. The relaxation of all atoms was performed until the atomic net force on each atom was less than 0.02 eV/Å and the electronic convergence reached 10^{-6} eV. The partial atomic charges were determined by using Bader charge analysis[85] as implemented by Henkelman[86].

The ZSM-5 unit cell comprises 96 T-sites (Si or Al), and 192 oxygen atoms. The dimensions of the unit cell were fixed with a = 20.078 Å, b = 19.894 Å, c = 13.372 Å and $\alpha = \beta = \gamma = 90^{o}$.

The structures of synergistic sites at the intersection were adopted from our previous papers (NMR paper). The deprotonation energies were given by calculating the energy difference between the isolated charged species and the BAS:

$$\mathrm{DPE} = \mathrm{E_{Z^-}} + \mathrm{E_{H^+}} - \mathrm{E_{HZ}}$$

in which $\mathrm{E_{Z^-}}$, $\mathrm{E_{H^+}}$ and $\mathrm{E_{HZ}}$ are energy of negatively charged deprotonated zeolite, proton and the zeolite before protonation, respectively.

The climbing image nudged elastic band method, which uses 8 images, was employed to identify transition states (TS) and calculate activation barriers. The force threshold for NEB

calculations was set to 0.02 eV/Å. Transitions states were confirmed by verifying the presence of a single imaginary frequency through vibrational analysis. The Gibbs free energy was calculated using the harmonic oscillator model at 500 °C. The energy threshold for vibrational frequency calculations was set at 10^{-8} eV. The low-frequency vibrations resulting from free rotation and translations were addressed using the quasi-rigid rotor harmonic oscillator approximation (qRRHO) developed by Grimme [73] and Head-Gordon. [75] Additionally, the pressure of gas-phase systems in Gibbs free energy calculations was carried out at 1 atm.

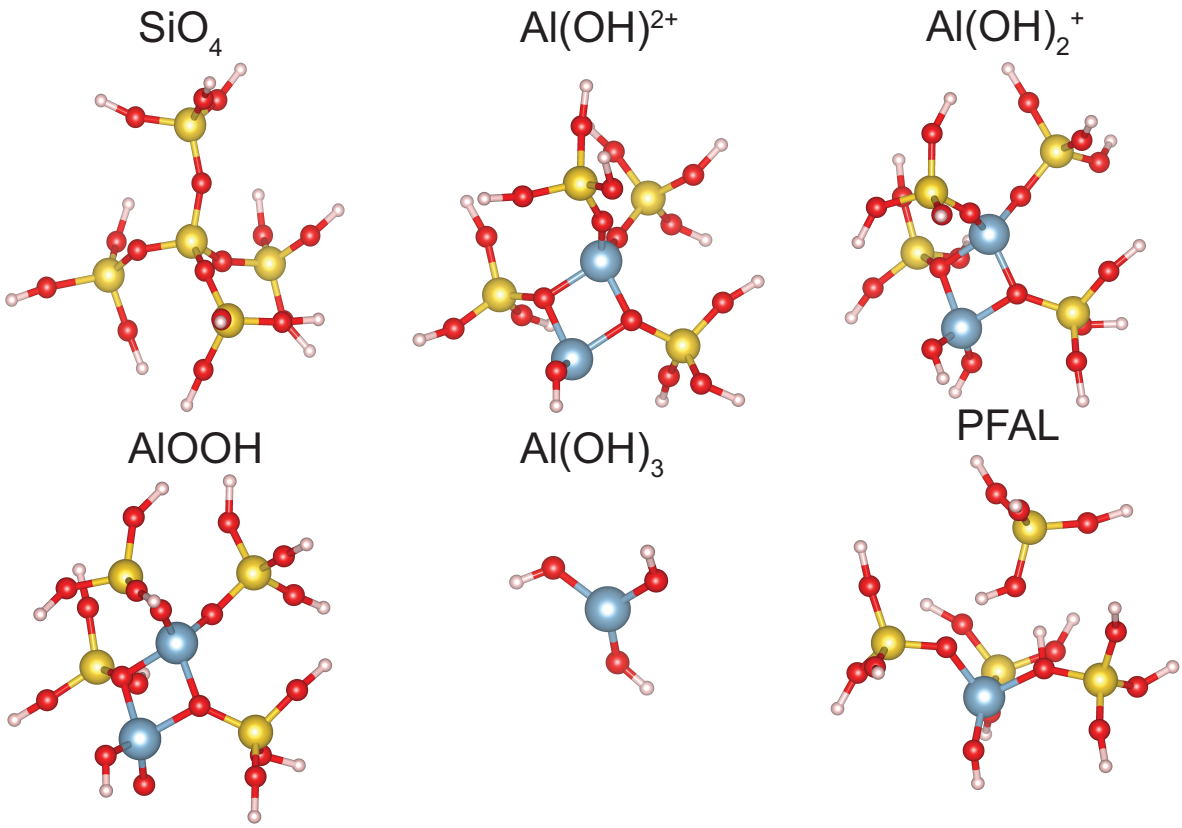


Figure 23. Calculated structures used in polarizability calculations.

Polarizabilities isolated cluster/molecules were calculated using Gaussian 09. [87] The clusters/molecules were taken from optimized structures from VASP calculations and then single

point energies calculations were carried out with B3LYP hybrid functional [88] and 6-311g +(d,p) basis set. The clusters/molecules used in polarizability calculations are shown in **Figure 23**.

4.4 Results and discussions

4.4.1 Effect of EFAL and PFAL to intrinsic acid strength of ZSM-5 zeolite

In chapter 2, the structures of possible active sites, including IBAS and synergistic sites, were proposed by comparing the computational and experimental ^{1}H and ^{27}Al NMR chemical shift (**Figure 24)**. The synergistic sites are composed of a conventional BAS and a nearby EFAL or PFAL species. There are two possible synergistic sites for each EFAL species: in one of them, the EFAL does not have a direct interaction with the proton; in the other one, the EFAL is located closer and forms a hydrogen bond with the proton. For PFAL in this study, we considered the species forming at the early stage of hydrolysis (one water molecule incorporated). The energy and Gibb free energy formation of this PFAL was discussed early in chapter 3. [36] To evaluate the intrinsic acidity of different proposed active sites in **Figure 24**, the DPE of them were calculated and compared. The DPE is the energy required to remove the proton from a BAS to an infinite distance, thus representing an indicator for intrinsic acid strength of a zeolite catalyst. The considered protons are positioned at T7 for all the studied models to reduce the other factors which could affect the DPE.

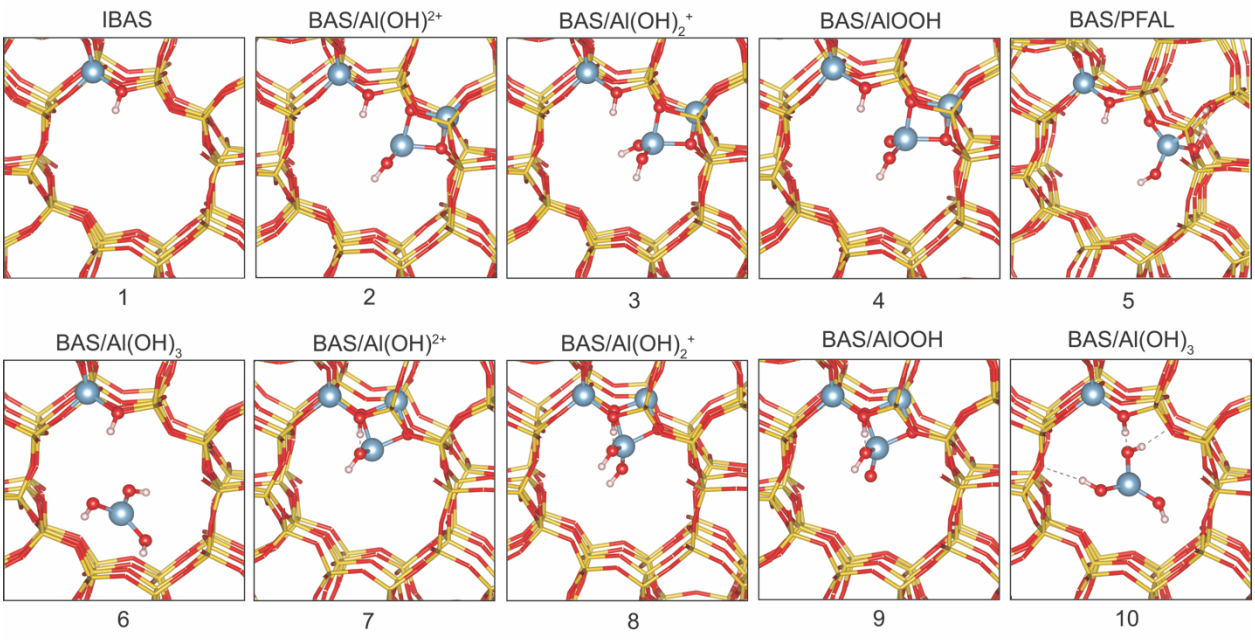


Figure 24. Calculated structures of proposed active sites in H-ZSM5 zeolite.

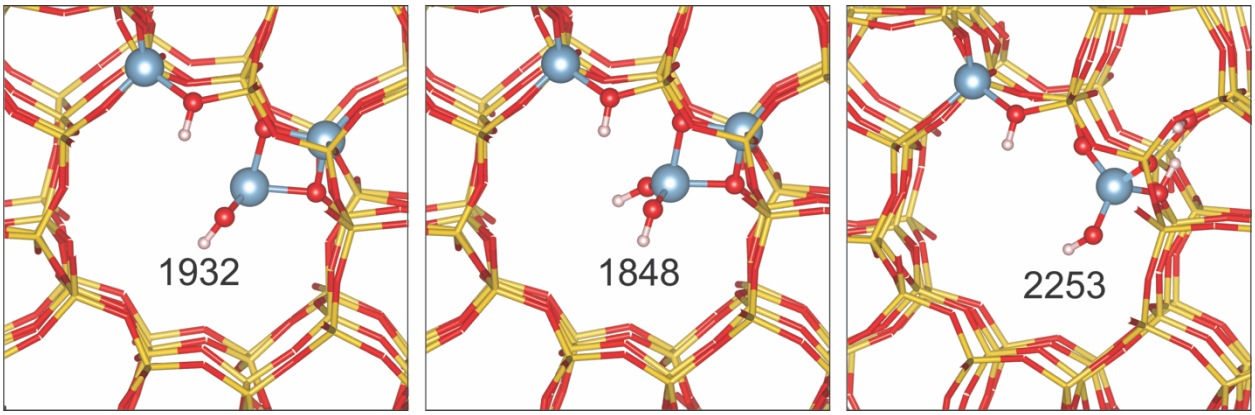


Figure 25. The numbers present the DPE of hydroxyl group in each structure. Units are kJ/mol.

As **Table** 1 illustrates, the DPE of synergistic sites without hydrogen bonds **(structure 2-6, Figure 24)** fall within the range of 1653-1660 kJ/mol, with a difference of less than 16 kJ/mol compared to DPE of IBAS (1644 kJ/mol). These DPE values match well with prior finding from Jones et. al., [89] which reported a range of 1620-1667 kJ/mol for isolated BAS in various locations of MFI zeolite. The presence of EFAL and PFAL species near a BAS without direct interaction (e.g. hydrogen bond) could alter the electron affinity, leading to small variations in the DPE values of these synergistic sites. Importantly, for synergistic sites where EFAL and PFAL species are closer to BAS and form hydrogen bond with it (**structure 7-10, Figure 24**), the DPE values significantly increase, reaching up to 1790 kJ/mol as seen in Table 1. These hydrogen bond make BAS more challenging to protonate guest molecules as they require extra energy to be broken. Even though the synergistic sites with hydrogen bond are weaker, in another of our study, it was demonstrated that they contribute to activity enhancement. The hydrogen bond plays a role in stabilizing the EFAL species and if another BAS is in proximity, it can greatly enhance the activity of that BAS. Li et al. [38, 79] supported these finding noting that the coordination of EFAL species to oxygen atom nearest to framework Al is responsible for the enhancement of acidity of dealuminated HY zeolite, rather than the direct interaction (such as hydrogen bond) between BAS and EFAL species. The ^{1}H NMR values of BAS having no direct interaction with EFAL/PFAL remain unchanged relative to IBAS while ^{1}H NMR of the BAS having hydrogen bonds are shifted to a downfield region of 11-18 ppm, as presented in chapter 2.

Additionally, the protons in hydroxyl groups associated with EFAL $Al(OH)^{2+}$, $Al(OH)_2^{+}$ and PFAL are not active because their DPEs are 288, 204, and 609 kJ/mol higher than that of the IBAS, respectively (**Figure 25). Figure 26** shows the DPE of various proposed active sites. It is thus reasonable to assume that only the protons in IBAS and synergistic sites, which do not form

hydrogen bonds with EFAL/PFAL are related to the catalytic activity. In the following sections, propane cracking and dehydrogenation reactions are only carried out on these active sites.

Table 4. The DPE values of the proposed active site in H-ZSM5 zeolite

Style of site	site	structure in Figure 1	DPE (kJ/mol)
IBAS	I-BAS	1	1644
Synergistic site without H-bond	$BAS/Al(OH)^{2+}$	2	1657
	$BAS/Al(OH)_2^{+}$	3	1660
	BAS/AlOOH	4	1653
	$BAS/Al(OH)_3$	5	1653
	BAS/PFAL	6	1654
Synergistic site with H-bond	$BAS/Al(OH)^{2+}$	7	1700
	$BAS/Al(OH)_2^{+}$	8	1709
	BAS/AlOOH	9	1682
	$BAS/Al(OH)_3$	10	1690

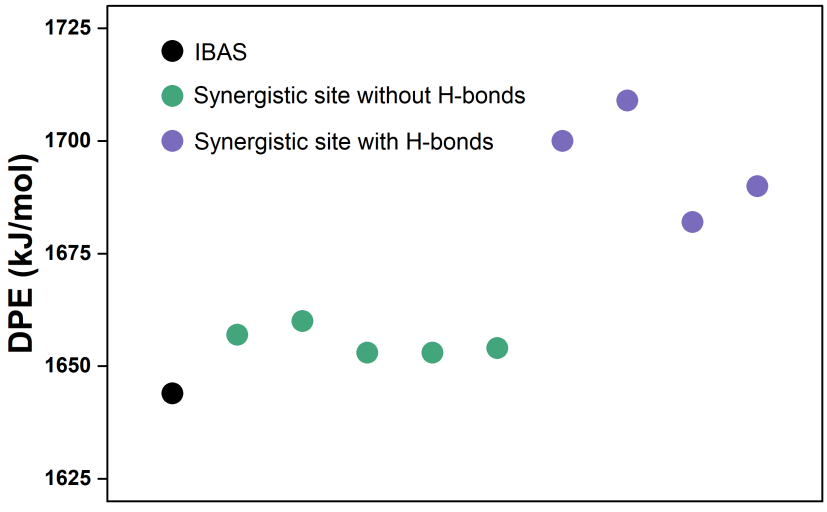
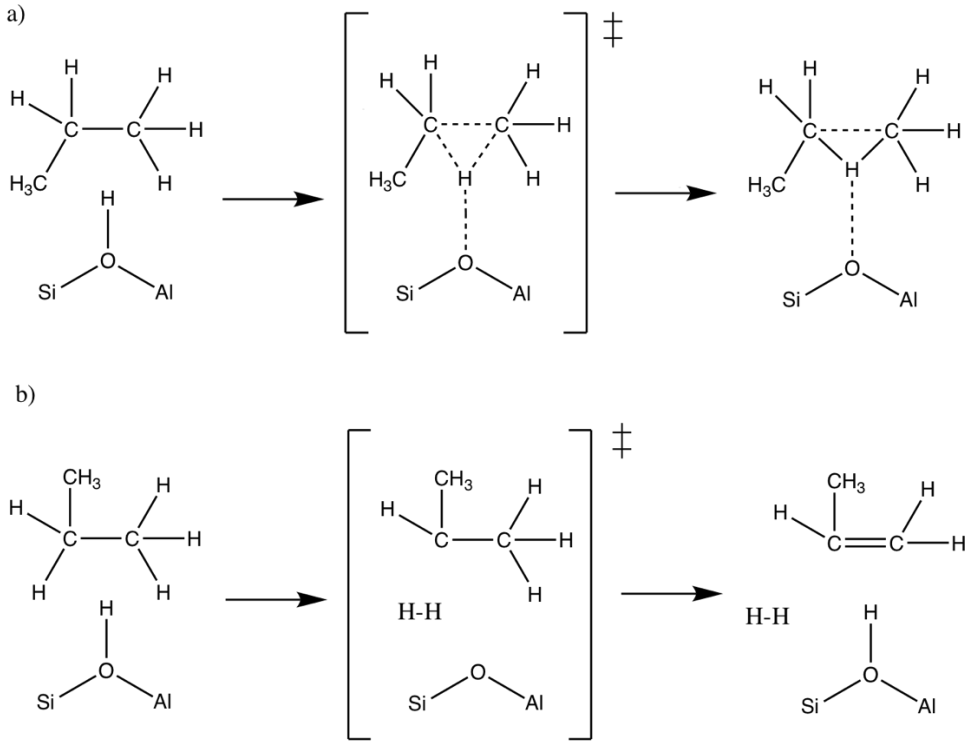


Figure 26. DPE for various proposed active site in HZSM-5 zeolite.

3.4.2 Propane cracking reaction

3.4.2.1 The influence of EFAL and PFAL on adsorption and activation energy of propane cracking.



Scheme 3. Reaction mechanism of propane a) cracking and b) dehydrogenation of methylene group.

Enthalpy, entropy, and Gibb free energy of propane cracking reactions were calculated and compared among different active sites. The cracking process is limited by the initial protonation of the C-C bond to form the propyl carbonium intermediate (**Scheme 3a**). The C-C bond of the propane molecule that undergoes cracking is located directly over the O-H group of BAS. All the adsorption-related values were calculated at this position of propane.

The adsorption, the intrinsic activation, and the apparent activation energy of propane cracking on a variety of active sites are presented in **Table 5 and Figure 27**. The adsorption energy

of propane over IBAS at the intersection is -68 kJ/mol, in good agreement with previous computational work reported by Moor et al. [90], which reported values of about -64 and -53 kJ/mol for propane adsorption in the straight and sinusoidal channels, respectively. There is little variation in the adsorption energies across the six active sites. The charge transfers between the propane molecule and zeolite framework at adsorption states are negligible, and these values are comparable across all active sites as shown in **Table 6**. The electron density differences in **Figure 28** show that the propane molecule interacts with the BAS while no charge interaction occurs between the propane molecule and EFAL/PFAL species. These results support the similarity of propane adsorption energy on IBAS and synergistic sites. However, the calculated adsorption energies tend to be less negative than the experimental measurements. For example, values reported by Gounder et al. [91] and Narbeshuber et al. [92] were 43 kJ/mol.

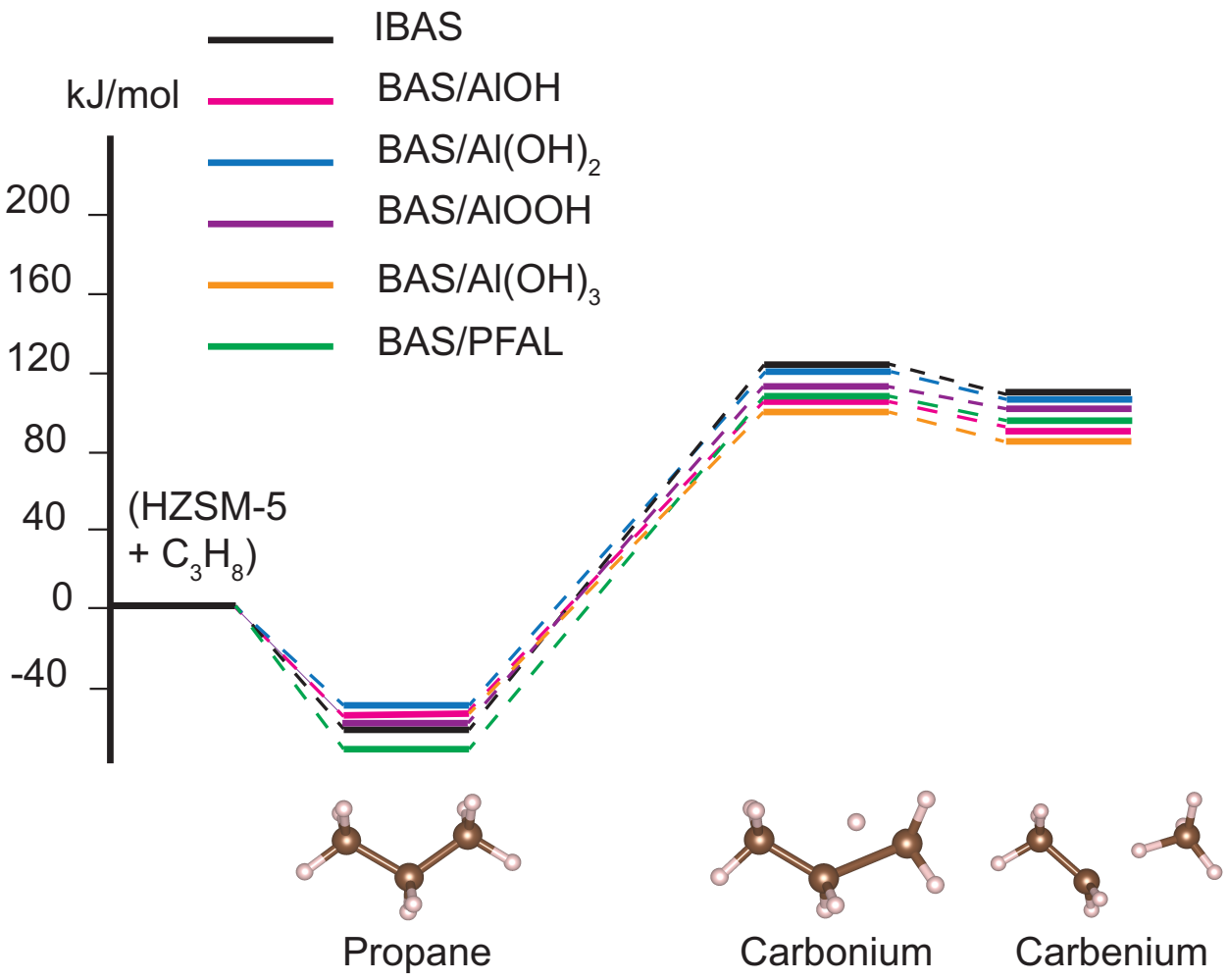


Figure 27. Enthalpy profiles of propane cracking on different active sites.

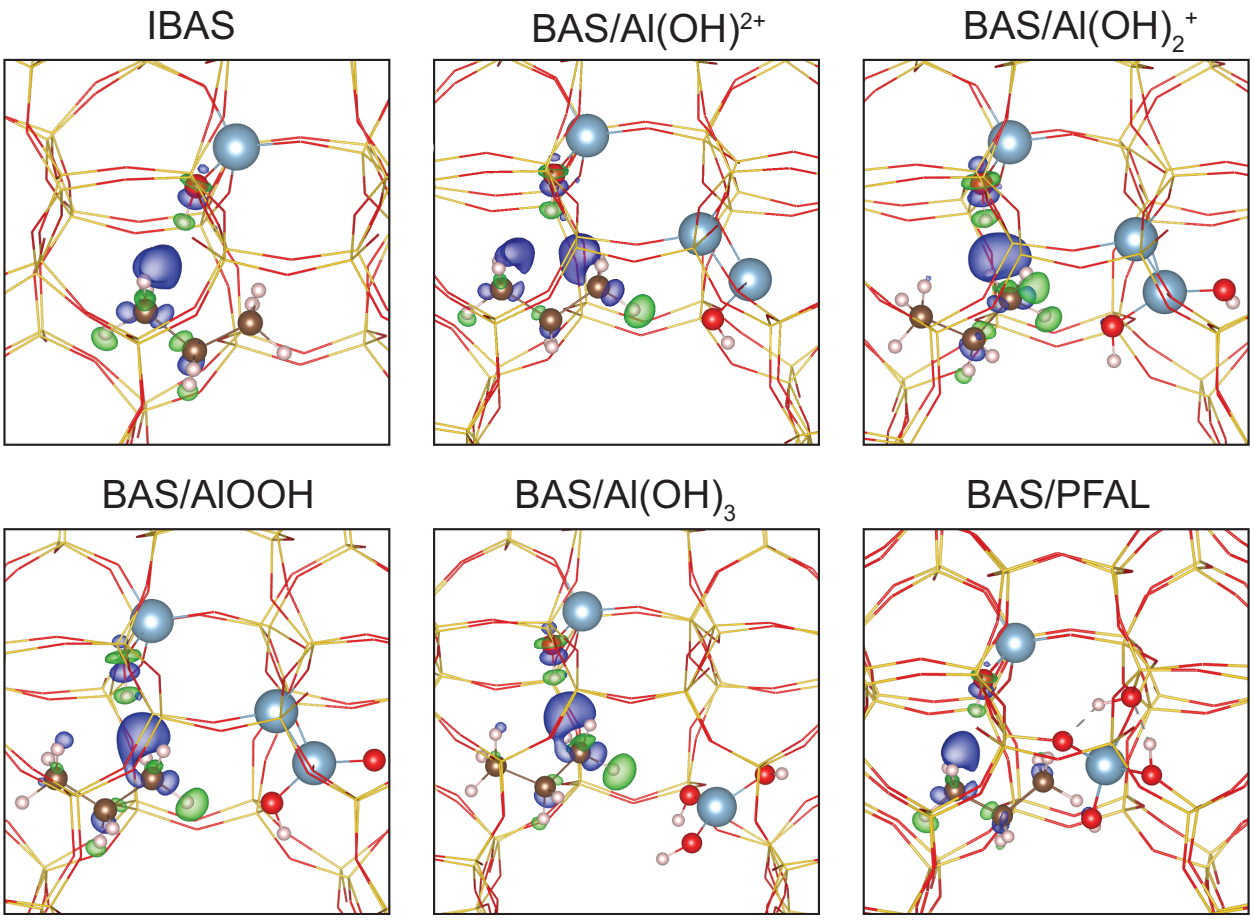


Figure 28. Electron density difference charge of propane at adsorption state on various active sites, the value of isosurface is 0.002 au. The blue color represents accumulation of charge and the green color represents depletion of charge.

Table 5. Adsorption, and activation energy of propane cracking reactions on different active sites. The calculation of energy utilized a gas phase propane reference.

Sites	ΔE_{ads}	ΔE_{app}	$\Delta E_{int}^{\ddagger}$	$\Delta E_{intermediate}$

	(kJ/mol)	(kJ/mol)	(kJ/mol)	(kJ/mol)
IBAS	-68	122	189	110
BAS/Al(OH)$^{2+}$	-63	106	169	106
BAS/Al(OH)$_2^+$	-61	120	181	120
BAS/AlOOH	-64	112	176	112
BAS/Al(OH)$_3$	-63	102	165	102
BAS/PFAL	-71	108	179	94

Table 6. Charge transfers from adsorption states to zeolite framework.

Sites	Charge transfer (e)
IBAS	0.025
BAS/Al(OH)$^{2+}$	0.029
BAS/Al(OH)$_2^+$	0.028
BAS/AlOOH	0.032
BAS/Al(OH)$_3$	0.025
BAS/PFAL	0.026

Table 7. Charge resides on TS of propane cracking reactions on various active sites.

Sites	Charges reside on TSs $C_3H_9^+$
IBAS	0.8

BAS/Al(OH)$^{2+}$	0.9
BAS/Al(OH)$_2^+$	0.8
BAS/AlOOH	0.8
BAS/Al(OH)$_3$	0.8
BAS/PFAL	0.8

Table 8. Atomic distances of transition states on different site, with C1: terminal C, C2: middle C, H: BAS, and O: the protonated oxygen.

Sites	C1-C2 (Å)	C1-H (Å)	C2-H (Å)	O-H
IBAS	1.71	1.48	1.73	1.26
BAS/Al(OH)$^{2+}$	1.88	1.22	1.32	2.29
BAS/Al(OH)$_2^+$	1.79	1.28	1.41	1.75
BAS/AlOOH	1.72	1.23	1.63	1.74
BAS/Al(OH)$_3$	1.68	1.49	1.79	1.29
BAS/PFAL	2.12	1.21	1.33	2.42

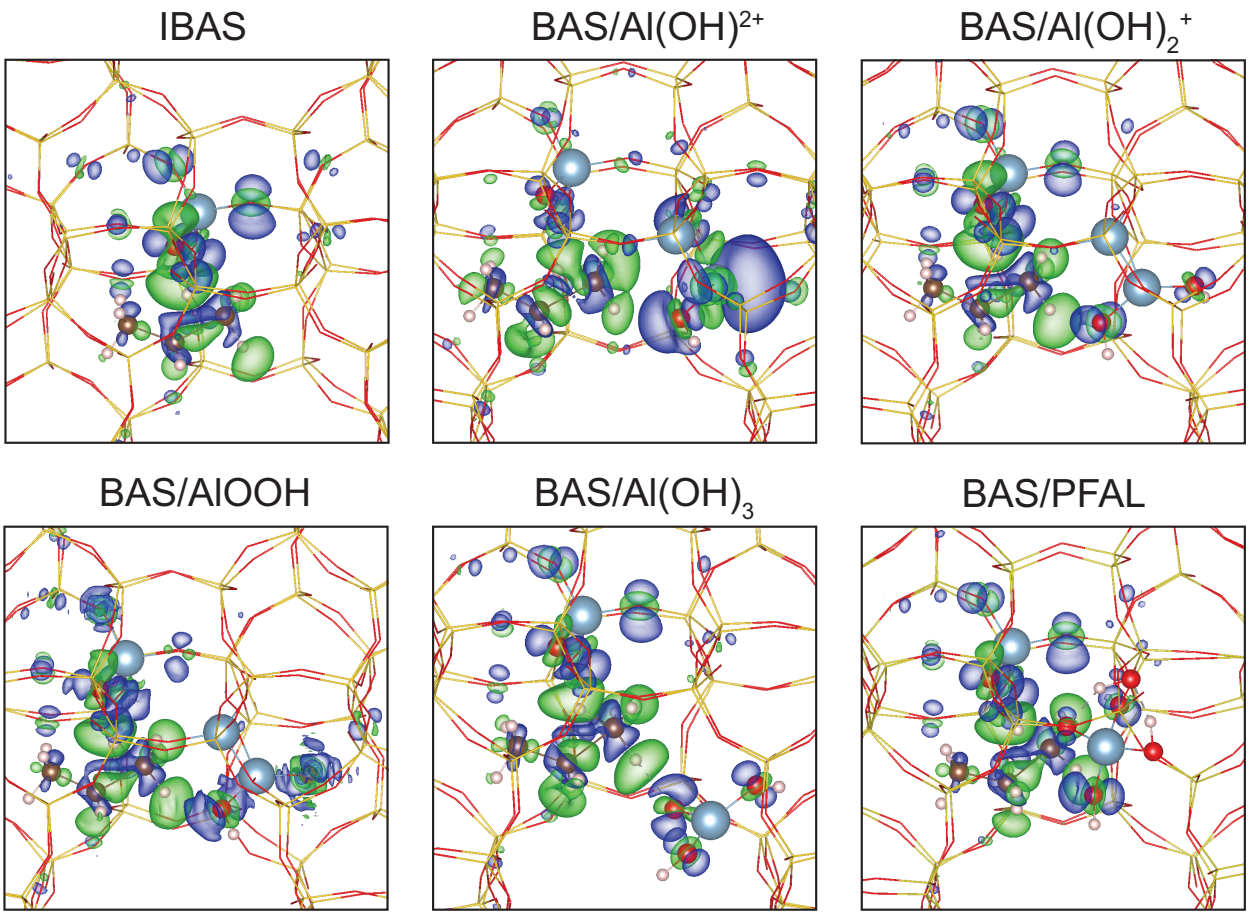


Figure 29. Electron density difference charge of TS of propane cracking reactions on various active sites, the value of isosurface is 0.002 au. The blue color represents accumulation of charge and the green color represents depletion of charge.

According to **Figure 27** and **Table 5**. The activation barriers of propane cracking reactions depend on the local environments surrounding active sites. The intrinsic activation energy of IBAS in this work (189 kJ/mol) is in good agreement with previously reported theoretical and experimental values. For instance, Gounder et al.[91] and Narbeshuber et al. [92] reported experimental values of about 200 kJ/mol and 195 kJ/mol, respectively, while Sharada et al. [93] using QM/MM

method reported a theoretical value of 184 kJ/mol. It is known that the PBE calculation method used in this study can result in underestimations of the barrier height. [94] This underestimation explains the slight discrepancy between our calculated value and experimental measurements. The propane cracking reaction shows significantly lower intrinsic activation energy, which ranges from 165-181 kJ/mol, among five distinct synergistic sites (compared to 189 kJ/mol for isolated BAS sites). Based on Bader charge analysis, the charges reside on TSs at all active sites except the BAS/$Al(OH)_2^+$ site is 0.8^+, while it is 0.9^+ on TS at BAS/$Al(OH)_2^+$ site. These results point towards the identity of the TS as $C_3H_9^+$ carbonium cation. The TS on BAS/$Al(OH)_2^+$ site possesses a charge higher than other TSs, and this value is closest to 1^+ as the proton approaches the C-C bond at a shorter distance compared to other TSs, as shown in **Table 8**. Additionally, **Figure 29** reveals that the positive charge localizes at the C-C bond that is attached by the proton, inducing dipole moments in the carbonium molecule. In contrast to the adsorption state, the carbonium cation $C_3H_9^+$ exhibits charge interactions with EFALs and PFAL species. The EFALs and PFAL species are charged species that possess dipole moments, enabling them to generate dipole-dipole forces with the TS carbonium cation $C_3H_9^+$, shown in **Figure 30**. These interactions stabilize the TS systems and decrease the activation barrier of the propane cracking reaction on synergistic sites.

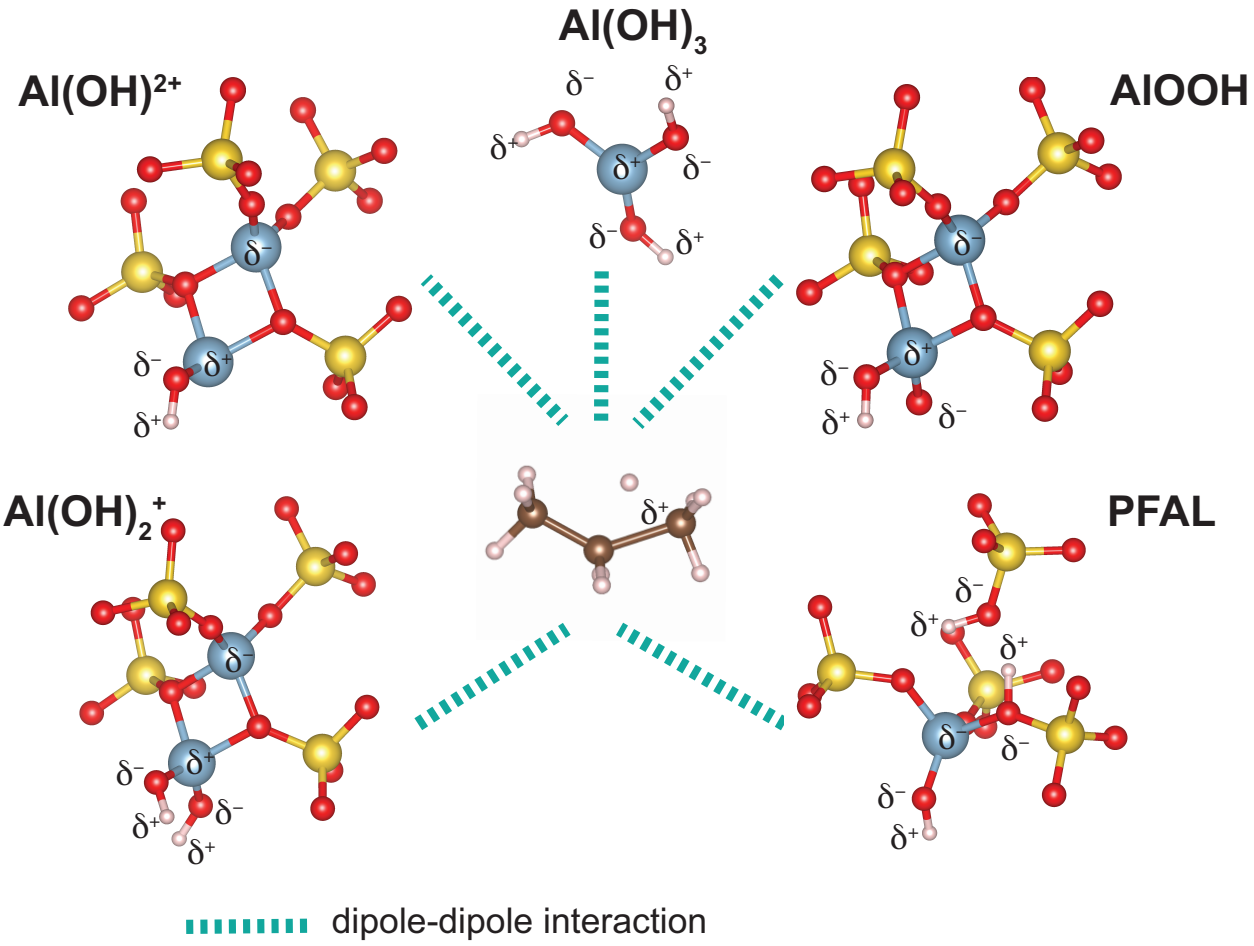


Figure 30. Electrostatic interaction between carbonium C3H9$^+$ and different EFAL and PFAL species.

Table 9 shows the polarizability of propane C_3H_8 and carbonium cation $C_3H_9^+$ on various active sites, whereas **Table 10** displays the polarizability of zeolite unit SiO_4 and different EFALs and PFAL. The term polarizability refers to the tendency of molecules to generate induced electric dipole moments when subjected to an electric field. The charge distribution of the TS carbonium cation is not uniform, and adjacent charged species can cause the molecule to have an instantaneous dipole, which then induces another dipole in its neighboring molecule. Thus, the existence of EFAL and PFAL enhances the electrostatic interaction at TS.

It is worth mentioning that the presence of EFAL $Al(OH)_3$ in reaction environment resulted in a significant reduction of the activation barrier by 24 kJ/mol. This potent stabilization is attributed not only to the dipole-dipole force but also to the formation of a hydrogen bond between the TS and OH group of the $Al(OH)_3$ species, shown in **Figure 29**. The sharing of the sole electron on a hydrogen atom bonded to an oxygen atom results in the hydrogen atom having a significantly smaller radius. This enables it to approach the EFAL $Al(OH)_3$ very closely, which leads to a highly stable configuration with low energy. Therefore, the impact of hydrogen bond can be substantial, and their strength is significant that they resemble weak covalent bond. This is why the activation barrier is the lowest at the BAS/$Al(OH)_3$ site compared to other active sites.

Table 9. Polarizability of propane in the gas phase and carbonium cation on different active sites.

	Polarizability of C_3H_8
Gas phase	37.8
Sites	**Polarizability of $C_3H_9^+$**
IBAS	74.3
BAS/$Al(OH)^{2+}$	142.5
BAS/$Al(OH)_2^+$	64.3
BAS/AlOOH	64.7
BAS/$Al(OH)_3$	64.7
BAS/PFAL	78.9

Table 10. Polarizability of zeolite unit SiO_4, EFALs and PFAL species.

Sites	Polarizability
SiO_4	32.3
$Al(OH)^{2+}$	209.4
$Al(OH)_2^+$	194.7
AlOOH	194.9
$Al(OH)_3$	32.7
PFAL	182.6

3.4.2.2 The influence of EFAL and PFAL on adsorption and activation entropy of propane cracking.

Table 11. The change of entropy along the reaction coordinate of propane cracking reactions on different active sites.

Sites	ΔS_{ads} (J/mol/K)	ΔS_{app} (J/mol/K)	$\Delta S‡_{int}$ (J/mol/K)	$\Delta S_{intermediate}$ (J/mol/K)
IBAS	-165	-188	-23	-155
BAS/$Al(OH)^{2+}$	-170	-185	-15	-181
BAS/$Al(OH)_2^+$	-164	-186	-22	-164
BAS/AlOOH	-165	-179	-14	-161
BAS/$Al(OH)_3$	-167	-196	-29	-177
BAS/PFAL	-159	-165	-6	-166

To evaluate the entropic changes of propane in different local environments within the H-ZSM5 zeolite, this study assumes that the reactant is strongly adsorbed onto active sites, resulting in the propane molecule being immobilized with negligible rotational and translational entropy motions. Additionally, the solid zeolite has minimal rotational and transitional motion, and thus any changes in entropy are solely due to alterations in harmonic vibrational modes. This method distinguishes entropy loss at transition states from stable states, allowing for the estimation of the contribution of entropy changes to activation barriers along the reaction pathway. **Table 11** provides a comparison of the entropy change for elementary steps versus the gas phase along the reaction coordinate. The adsorbed entropies of propane on different active sites analyzed in this work range from -170 to -159 J/mol/K and are not significantly different. Compared to prior studies, both Moor et al. and Gounder et al. [90, 91] reported a calculated entropy decrease of roughly -100 J/mol/K during adsorption, while the experimental value calculated based on statistical thermodynamic equations was -94 kJ/mol/K. According to Moor et al. [90, 91], the entropy loss during n-alkane adsorption could be better described by considering the loss of two rotational and one translational degree of freedom for the molecular entropy. In the case of MFI zeolite, Dauenhauter and coworkers[95] showed that assuming a loss of one translational and one rotational degree of freedom in entropy upon n-alkane adsorption led to underestimation for the entropy loss. However, they argued that assuming a loss all the three translational degrees of freedom would result in an overestimation for the entropy loss. They also found that the entropy loss of linear alkane upon adsorption on MFI was about 38% of their gas phase entropy. Even though this entropy model overestimates the entropy losses, it still provides a satisfactory comparison among the different active sites.

The majority of active sites, including IBAS, BAS/$Al(OH)^{2+}$, BAS/$Al(OH)_2^+$, BAS/AlOOH, and BAS/$Al(OH)_3$, exhibit activation entropies that are insignificantly different. The activation entropy on IBAS is -188 J/mol/K. Notably, the activation entropy on BAS/PFAL is 23 J/mol/K less negative than IBAS. The TS on BAS/PFAL site is a late one and resembles the product, which is evidenced by the elongated C-C bond (2.12 Å compared to 1.71 Å on IBAS). The more negative values of apparent activation entropies in the cracking reaction indicate that the transition states are more restricted in movement than that of the adsorption state, consistent with a prior study.[91] According to Sharada et al. [93], the transition state of cracking happens early along the reaction coordinate and interacts strongly with zeolite framework, which result in a tightly bound transition state. It can be deduced that the surrounding spaciousness of the actives has little influence on the motion of the transition states. This assessment is supported by the insignificant influence of EFAL and PFAL to the apparent activation entropies

3.4.2.3 The influence of EFAL and PFAL on adsorption and activation Gibbs free energy of propane cracking.

Table 12. Adsorption, and activation free energy of propane cracking reactions on different active sites, calculated at 773 K. The calculation of free energy utilized a gas phase propane reference.

Sites	ΔG_{ads}	ΔG_{app}	ΔG_{int}	$\Delta G_{intermediate}$
IBAS	60	267	207	230
BAS/$Al(OH)^{2+}$	68	249	180	246
BAS/$Al(OH)_2^+$	65	264	198	247
BAS/AlOOH	64	253	187	238

BAS/Al(OH)$_3$	66	250	186	236
BAS/PFAL	52	236	184	223

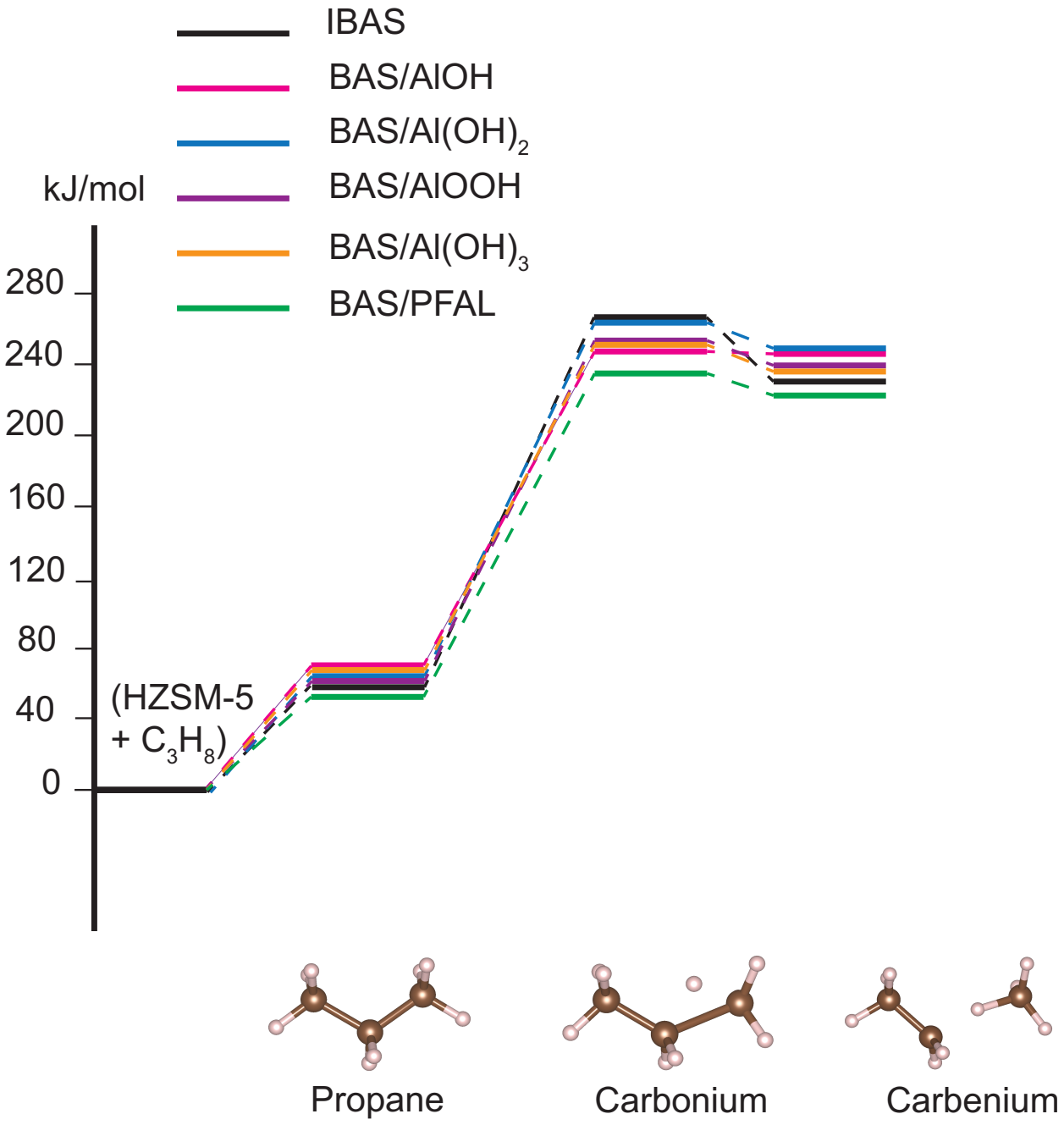


Figure 31. Free energy profiles of propane cracking on different active sites, calculated at 773 K.

Since the enthalpies and entropies for propane cracking are known, the Gibb free energies can be calculated as $\Delta G = \Delta H - T\Delta S$. The calculated values of Gibb free energy are given in **Table 12 and Figure 31**. As previously discussed, the free energies in this study would be

generally overestimated, but to a consistent extent, leading to reliable free activation barriers. In this work, the free energy of activation barriers on IBAS at the 10-MR intersection is 267 kJ/mol. The free energy of activation barriers of propane on BAS in 8-MR and 12-MR of mordenite zeolite was reported by Gounder et al. [91] were about 227 and 234 kJ/mol, respectively. There are significant decreases in the free activation energies activation on synergistic sites, resulting in a boost in the cracking reaction rate, primarily driven by lower activation energies.

3.4.3 Propane dehydrogenation reaction

3.4.3.1 The influence of EFAL and PFAL on adsorption and activation energy of propane dehydrogenation

Table 13. Adsorption, and activation energy of propane dehydrogenation reactions on different active sites. The calculation of energy utilized a gas phase propane reference.

Sites	ΔE_{ads} (kJ/mol)	ΔE_{app} (kJ/mol)	$\Delta E_{int}^{\ddagger}$ (kJ/mol)	$\Delta E_{intermediate}$ (kJ/mol)
IBAS	-62	159	221	84
BAS/Al(OH)$^{2+}$	-65	129	195	81
BAS/Al(OH)$_2^+$	-65	156	221	81
BAS/AlOOH	-64	168	232	78
BAS/Al(OH)$_3$	-72	164	236	89
BAS/PFAL	-67	157	224	86

The dehydrogenation reaction happens in parallel to the cracking reaction.[92] In this section, the dehydrogenation reactions are performed on various active sites. Propane dehydrogenation can take place by removing hydrogen from methyl or methylene groups. It has been reported that the activation barrier of a methylene group dehydrogenation is about 50 kJ/mol lower than the dehydrogenation reaction of a methyl group. [96] To minimize computational expenses, this study only focuses on the dehydrogenation of the methylene group, the mechanism of which is depicted in **Scheme 3b**. At the transition state configuration, O-H and C-H bonds are broken and simultaneously a hydrogen molecule together with a secondary propyl cation is formed. From one of terminal CH_3 groups, a proton jumps to a framework oxygen atom, forming a BAS and producing a propene molecule.

Table 13 and **Figure 32** show the energies profile of propane dehydrogenation along the coordinate reactions on different active sites. The intrinsic activation barrier of propane dehydrogenation on IBAS is 197 kJ/mol, which is in good agreement with previously reported results for CHA zeolite at 215 kJ/mol. [96] This slight difference can reasonably be accounted for by the difference in types of zeolite frameworks, the orientations of propane relative to the frameworks, and the employed computational methods. The EFAL and PFAL have less impact on the activation barrier for propane dehydrogenation than that on the cracking reaction. The striking observation is that the activation barrier on BAS/$Al(OH)_2^+$ is considerably lower than that on IBAS by 30 kJ/mol, whereas others synergistic sites have similar activation barrier to IBAS.

In **Figure 33**, it can be observed that there is a peak of TS molecules located 1.3 - 2 eV above the Fermi level, indicating a vacant orbital in the middle C after hydride transfer. **Table 14** provides information on the charges of the TSs, with all of them except for the one on BAS/$Al(OH)_2^+$ showing a charge of is 0.9^+, while the TS on BAS/$Al(OH)_2^+$ is charged 0.6^+. The

Bader charge analysis and density of states confirm that the TS of dehydrogenation is a carbenium $C_3H_7^+$. **Figure 34** shows the electron density differences, which illustrates that the positive charge delocalizes the entire TS molecule, resulting in a more symmetrically charged distribution. Additionally, the charge interactions between TS and most of EFALs and PFAL, with the exception of the EFAL $Al(OH)_2^+$, are negligible. The polarizabilities of TSs carbenium cation are comparable to the neutral propane molecule in the gas phase, and much lower than the polarizabilities of TS carbonium cations in propane cracking reactions. These findings suggest that the charge associated with the carbenium is more symmetrically distributed and they have low tendency to generate induced dipole moments. As a result, the EFAL and PFAL have a weaker influence on TS of propane dehydrogenation reaction. Differently, the lower activation barrier on BAS/$Al(OH)_2^+$ is due to the electrostatic interaction between the TS and EFAL $Al(OH)_2^+$ as shown in **Figure 34**.

Table 14. Charge resides on TSs of propane dehydrogenation reactions on various active sites.

Sites	Charges reside on TSs $C_3H_7^+$
IBAS	0.9
BAS/$Al(OH)^{2+}$	0.6
BAS/$Al(OH)_2^+$	0.9
BAS/AlOOH	0.9
BAS/$Al(OH)_3$	0.9
BAS/PFAL	0.9

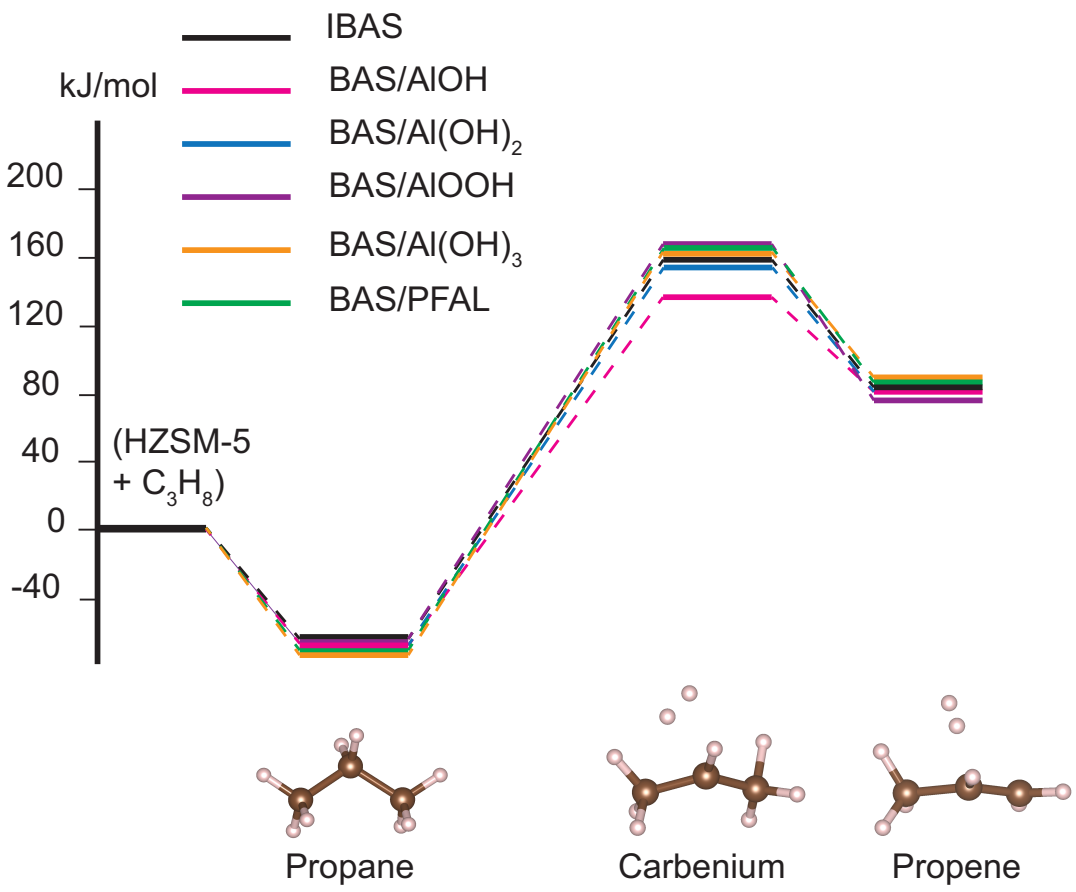


Figure 32. Energy profiles of the propane dehydrogenation reaction on different active sites.

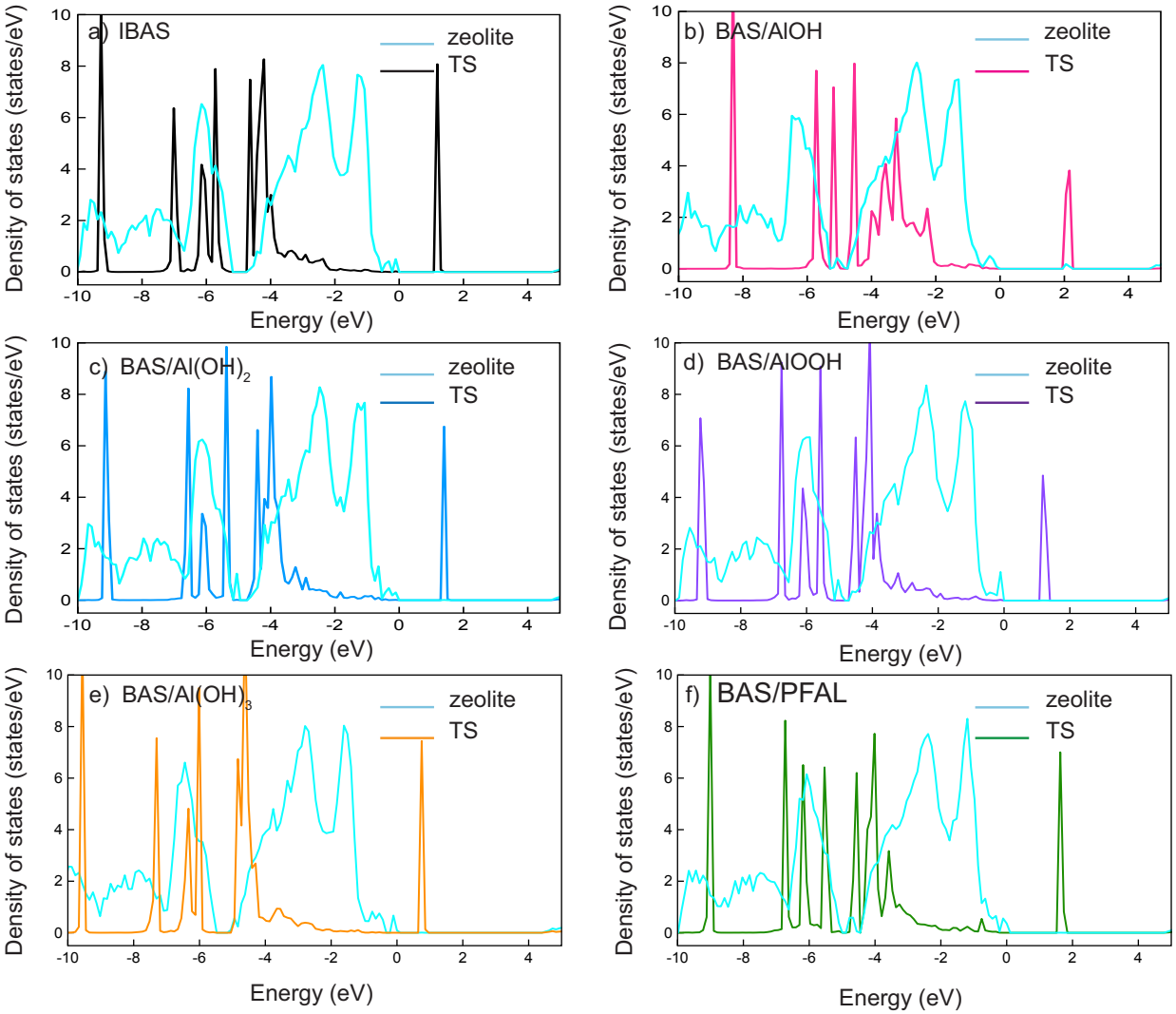


Figure 33. Density of state at the TSs of hydrogenation reactions.

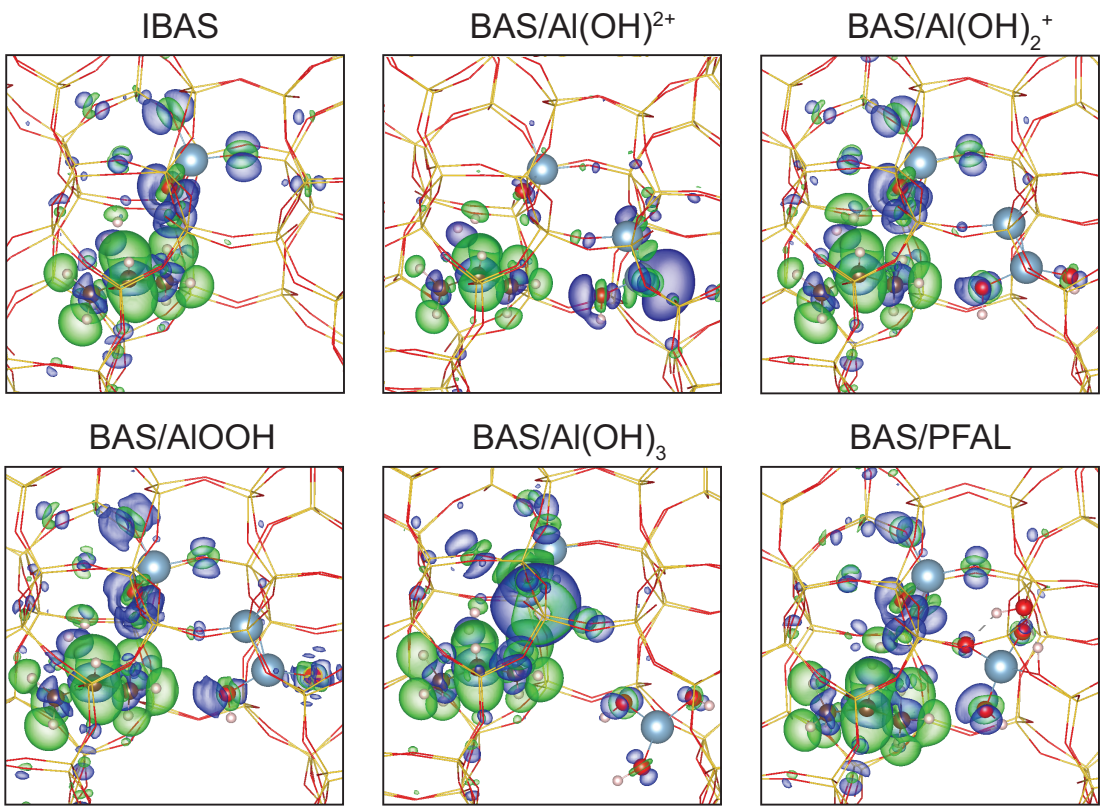


Figure 34. Electron density difference charge of TS of propane dehydrogenation reactions on various active sites, the value of isosurface is 0.002 au. The blue color represents accumulation of charge and the green color represents depletion of charge.

Table 15. Polarizability of propane in the gas phase and carbonium cation on different active sites.

	Polarizability of C_3H_8
Gas phase	37.8
Sites	**Polarizability of C_3H7^+**
IBAS	40.7
BAS/Al(OH)$^{2+}$	40.7

BAS/Al(OH)$_2^+$	41.1
BAS/AlOOH	40.9
BAS/Al(OH)$_3$	40.6
BAS/PFAL	41.6

3.4.3.2 The influence of EFAL and PFAL on activation entropy of propane dehydrogenation.

Table 16. The change of entropy along the reaction coordinate of propane cracking on different active sites.

Sites	ΔS_{ads}	ΔS_{app}	ΔS_{int}	$\Delta S_{intermediate}$
IBAS	-163	-129	34	-123
BAS/Al(OH)$^{2+}$	-161	-144	17	-125
BAS/Al(OH)$_2^+$	-163	-144	19	-124
BAS/AlOOH	-163	-139	24	-122
BAS/Al(OH)$_3$	-168	-150	18	-127
BAS/PFAL	-157	-154	3	-129

The losses of entropies at TSs for dehydrogenation are less negative than those of reactant states, indicating these TSs have greater freedom of movement relative to adsorption states and weakly interact with the active sites. This is in striking contrast to the cracking reaction, where the TS is more restricted in movement than the adsorption state. The dehydrogenation occurs later along the reaction coordinate, and the TS more resembles the product fragments. The space

surrounding the active sites has an impact on the TS of the dehydrogenation reaction. The confinement decreases in the presence of EFAL and PFAL specie, leading to apparent activation entropies on synergistic sites that are 10-25 J/mol/K more negative compared to that of IBAS.

3.4.3.3 The influence of EFAL and PFAL on free energy entropy of propane dehydrogenation.

Table 17. Adsorption, and activation free energy of propane dehydrogenation reactions on different active sites, calculated at 773 K. The calculation of free energy utilized a gas phase propane reference.

Sites	ΔG_{ads}	ΔG_{app}	ΔG_{int}	$\Delta G_{intermediate}$
IBAS	64	259	194	179
BAS/$Al(OH)^{2+}$	59	241	182	177
BAS/$Al(OH)_2^{+}$	61	267	206	177
BAS/AlOOH	62	275	213	172
BAS/$Al(OH)_3$	58	280	223	187
BAS/PFAL	54	276	222	185

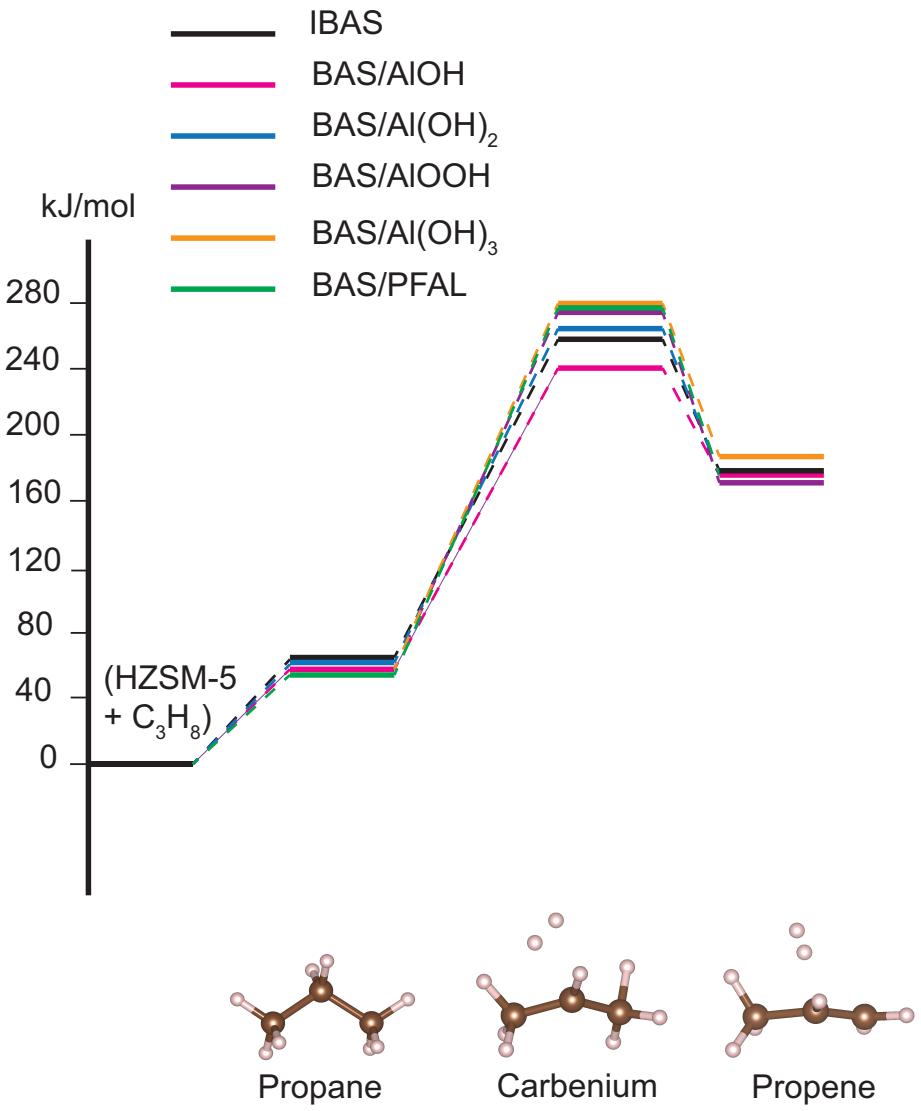


Figure 35. Free energy profiles of propane dehydrogenation reaction on different active sites, calculated at 775 K.

Table 17 and **Figure 35** present the free energy profile of dehydrogenation reactions on different active sites. It is noted that the synergistic site BAS/Al(OH)$^{2+}$ exhibits an apparent free activation barrier that is 18 kJ/mol lower than that of IBAS. For other synergistic sites, the activation barriers are comparable to that of IBA, but the activation entropies are more negative. As a results, the variation of free activation energy of dehydrogenation reactions on these sites is

due to the difference in activation entropy. The free energy barriers of dehydrogenation reactions on synergistic sites are higher because of the more negative of activation entropies in more confined environments.

3.4.3.3 Propane reaction under pulsedwater treatment.

Experiments conducted in this section was conducted by Tram Pham; we include this discussion here to compare with our DFT calculations. The propane cracking was carryout out in a pulsed reactor. The experimental results in this section give support for the DFT-results. The rate of propane conversion on H-ZSM5 zeolite is presented in **Figure 36**. The reaction order is close to 1, shown in **Figure 37**, suggesting a monomolecular reaction pathway. The distribution of products under investigated reaction conditions are comparable, which include C_3H_6 (~ 42 wt.%), C_2H_6 (~ 36 wt.%), CH4 (~ 18wt%), and other light hydrocarbons. These results suggest that propane cracking and dehydrogenation both can take place under the reaction conditions. It was shown in **Figure 36** that HZSM5-15-AHFS catalyst has a significantly lower activity compared to the parent H-ZSM5-15. This result suggests that the AHFS treatment removes EFAL species leading to the loss of synergistic sites. HZSM5-11.5 has lower activity than HZSM5-15, which can be attributed to fewer synergistic sites in this catalyst.

Figure 38 presents the Arrhenius plot for estimating the activation energies of propane conversion in the investigated catalysts. The amount of the catalyst is varied to maintain a comparable level of reaction conversion. In AHFS treated catalysts, the activation energy for propane conversion is the highest, which is associated with the barrier on typical BAS. This value is the lowest in HZSM5-15 due to a significant number of synergistic sites in this catalyst, as discussed in our previous work. [25] It is important to note that the required barriers of both cracking

and dehydrogenation have contributed to the measured activation energies. The trend of activation barriers in **Figure 38** is consistent with DFT-calculated results, though the experimental values are higher than DFT calculations. This may originate from three main sources: (1) PBE functional usually gives underestimated values for activation barriers; (2) In this study, only the dehydrogenation of methylene group was explored, as it was reported to be 50 kJ/mol higher than that of the methyl group. Thus, it is reasonable to assume that the activation barrier of propane dehydrogenation will be higher when both reaction pathways are considered. Additionally, (3) the heat adsorptions were overestimated in DFT results, leading to underestimation of apparent activation barriers.

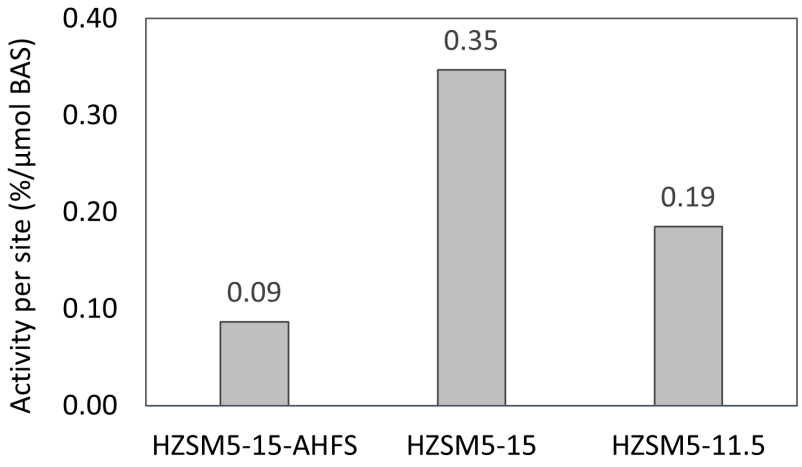


Figure 36. Activity per site of propane conversion in HZSM5-X zeolites, X is Si/Al ratio. 500 µl pulses of pure propane (>99%) are injected at temperature as 823 K. The BAS densities of HZSM5-15-AHFS, HZSM5-15 and HZSM5-11.5 are 0.45, 0.73 and 1.08 mmol/g, respectively.

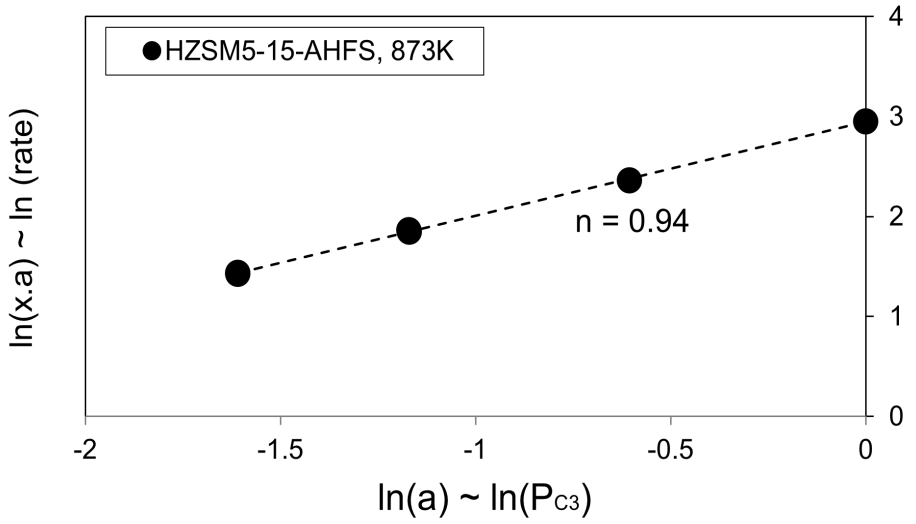


Figure 37. Estimation of the order of propane cracking on HZSM5-15-AHFS. In which x is the reaction conversion, a is the mole percent of propane in the loop.

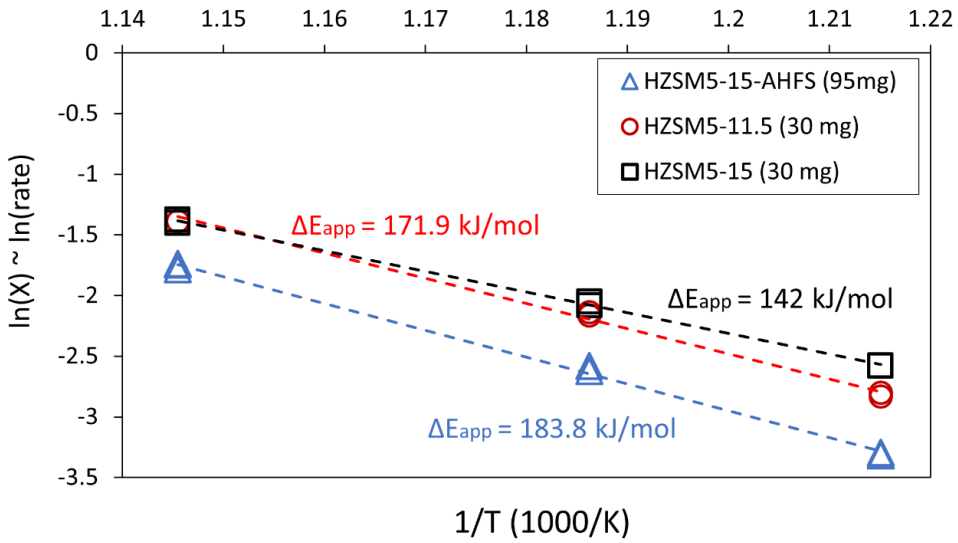


Figure 38. Estimation of apparent activation enthalpy of propane reactions on MFI zeolites.

3.4.4 Hexane cracking and dehydrogenation reactions

3.4.4.1 DFT calculations

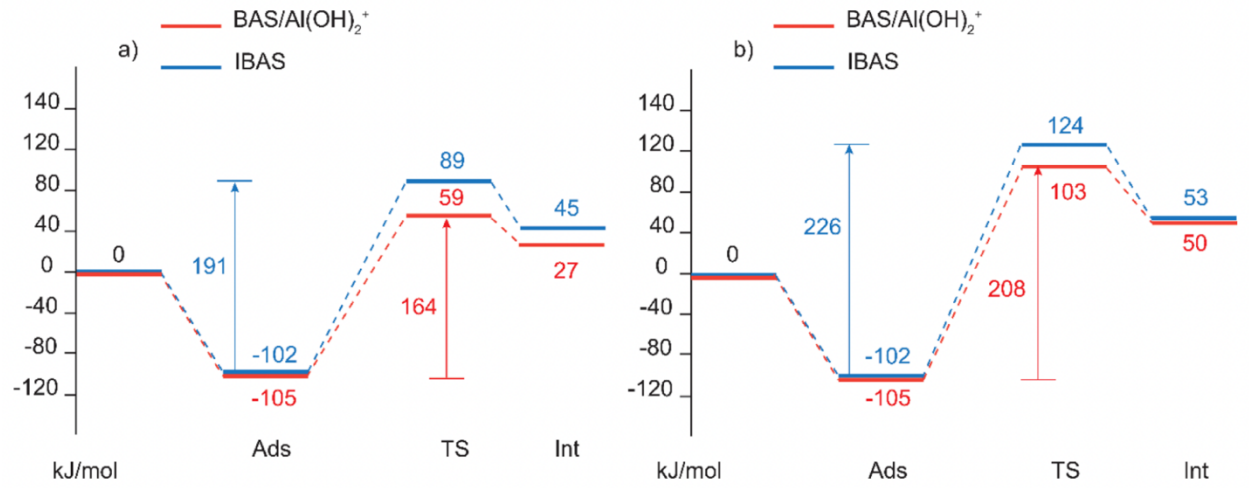


Figure 39. Reaction energy diagram of n-hexane (a) central cracking and (b) dehydrogenation of the methylene group. This figure was taken from ref. [31]

In the previous section, we discussed the roles of EFALs and PFAL in propane cracking. To further explore the role of EFAL species in different chain-length alkane cracking reaction, we utilized DFT calculations to compare the reaction profiles of hexane on IBAS and synergistic site $BAS/Al(OH)_2^+$. Hexane cracking on H-ZSM5 has multiple potential reaction pathways, and we selected central cracking and dehydrogenation of the methylene group as representative reactions. Figure 39 shows the reaction energy diagram of hexane central cracking and dehydrogenation on IBAS and synergistic site $BAS/Al(OH)_2^+$. The adsorption configurations are similar for both active sites, and the computed adsorption energies of hexane on IBAS and synergistic site are -102 and -105 kJ/mol, respectively.

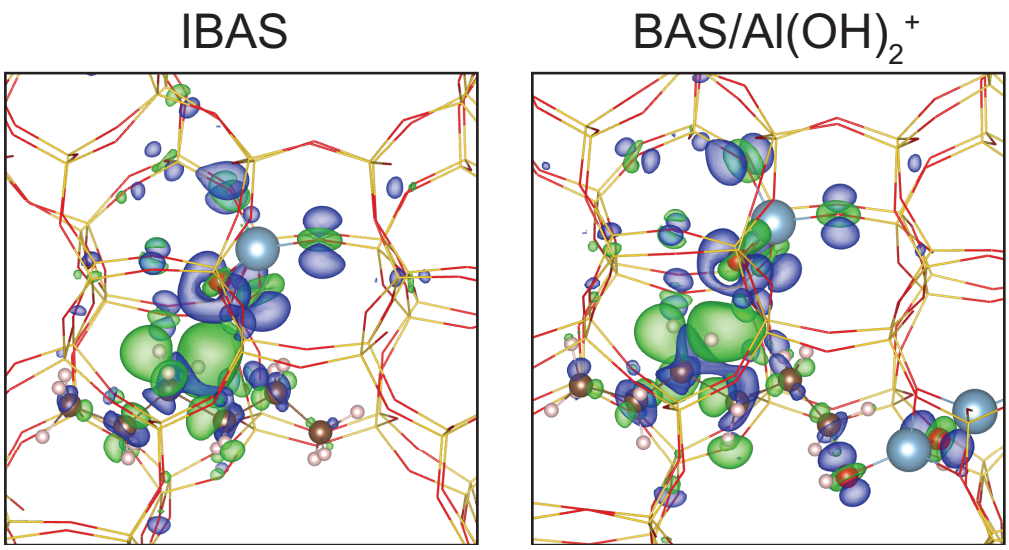


Figure 40. Electron density difference charge of TS of hexane cracking reactions on various active sites, the value of isosurface is 0.002 au. The blue color represents accumulation of charge and the green color represents depletion of charge.

The apparent activation energies for hexane central cracking are 89 kJ/mol over IBAS and 59 kJ/mol over the synergistic site. A similar trend is observed for the hexane dehydrogenation reaction, with an apparent barrier of 103 kJ/mol, which is 21 kJ/mol lower than that of IBAS. These results indicate that while the effect of EFAL species on the dehydrogenation reaction is less pronounced than on the central cracking reaction, it is still significant. The activation barriers for central cracking are lower than those for dehydrogenation, which is consistent with a prior study. [97] Additionally, the significant decrease in activation barriers for hexane conversion at the synergistic site is due to the electrostatic interactions between the TSs and EFAL $Al(OH)_2^+$. **Figure 40** and **Figure 41** illustrate the electron density difference charge of TS on IBAS and synergistic sites. In both TSs, the positive charges localize at the center of the molecules, which suggests that the molecules have dipole moments. The dipole-dipole interactions between the TSs and the EFAL

play a similar role as in the propane cracking reaction, stabilizing the energy of the systems and leading to a decrease in activation barriers.

Compared to propane, the polarizability of both the hexane molecule and its TSs in cracking and dehydrogenation reactions is high. As a result, the influence of EFAL on hexane reactions is more significant than that on propane. Furthermore, due to the longer chain length, the transition state of the dehydrogenation reaction of the methylene group in hexane has a positive charge localized at the center of the molecule, rather than being symmetrically distributed throughout the entire TS as in propane dehydrogenation reaction. Therefore, the impact of EFAL on the dehydrogenation of hexane is more potent than that on propane dehydrogenation.

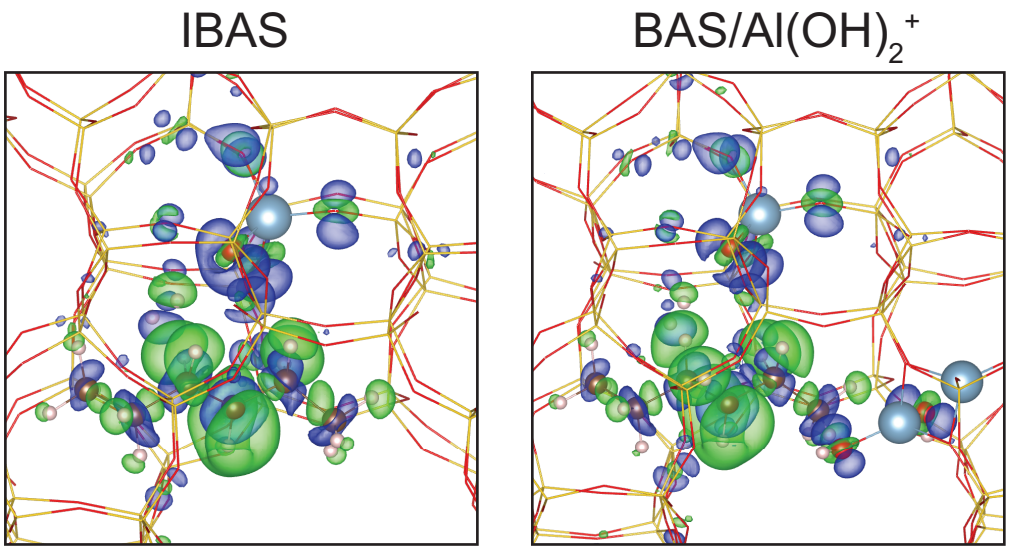


Figure 41. Electron density difference charge of TS of hexane dehydrogenation reactions on various active sites, the value of isosurface is 0.002 au. The blue color represents accumulation of charge and the green color represents depletion of charge.

Table 18. Polarizability of hexane in the gas phase, and its TSs in cracking and dehydrogenation reactions.

	Polarizability		
Locations	**Carbonium $C_6H_{15}^+$**	**Carbenium $C_6H_{13}^+$**	**Hexane C_6H_{14}**
IBAS	156.4	80.7	
BAS/Al(OH)$_2^+$	130.7	77.8	
Gas phase			73.8

Additionally, we found that the intrinsic activation barrier of n-hexane cracking over IBAS (191 kJ/mol) is similar to that of propane cracking (189 kJ/mol). This is in agreement with the finding of Gounder et al. [91] and Narbeshuber et al. [92], reported that the intrinsic activation barriers of hydrocarbons (C3-C6) cracking reactions are constant, and the variation in adsorption energy for different chain length hydrocarbons leads to different measured activation barriers.

3.4.4.2. Hexane conversion in pulsed and steaming reactions.

Experimenal results discussed in this section was obtained by Tram Pham. The hexane cracking was carryout out in pulsing and steaming reactions. The experimental results in this section give support for the DFT results. The aim of this section was to analyze the energies and entropies of the transition states of the cracking reaction in order to understand the reason behind the high activity on synergistic sites. Based on the data presented in Figure 42, the order of the reaction at various temperature on HZSM-5 catalyst is close to 1, indicating a monomolecular cracking mechanism in line with previous study. [98] To determine the cracking rate associated with the synergistic sites, the cracking rate corresponding to the IBAS measured on HZSM5-15-AHFS was subtracted. The findings show that the apparent activation enthalpy for the n-hexane cracking

on the synergistic sites is significantly lower (~75 kJ/mol) than that associated with the IBAS (110 kJ/mol), which is consistent with DFT results. The activation entropies obtained from different samples are comparable and listed in **Table 19**.

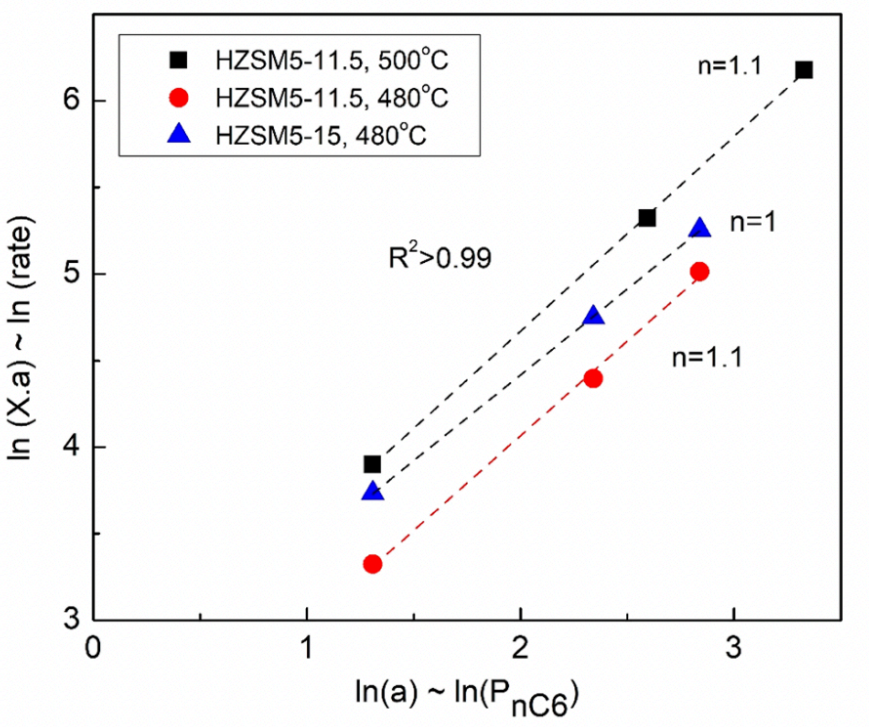


Figure 42. Determination of order of n-hexane cracking reaction, where a is the mole percent of n-hexane in the loop and X is the conversion of the reaction, taking from ref. [25]

The activation enthalpies and entropies for the synergistic sites were estimated using various HZSM-5 catalysts with Si/Al ratios ranging from 11.5 to 25, both in fresh samples and after exposure to pulsing and steaming water. The cracking barriers on IBAS were obtained from catalysts that had an insignificant amount of synergistic sites, such as zeolites with high Si/Al ratios and those after sodium exchange. The cracking rates associated with the synergistic sites

were calculated by subtracting the contribution of isolated sites from the measured rates at corresponding temperatures. It is worth noting that catalysts devoid of EFAL species, such as HZSM5-140, HZSM5-40, and HZSM5-15-AHFS, showed a similar apparent enthalpy of activation, despite differences in BAS location (intersection vs channels and concentration of paired sites. This enthalpy of activation is far greater than that observed when synergistic sites are present. Additionally, while the transition state enthalpy is significantly lowered over synergistic sites, the consequential penalties in TS entropy are far less pronounced.

Table 19. Estimated Activation Enthalpy and Entropy of n-hexane Cracking on Different MFI Zeolites, taking from ref. [31]

	ΔH_{app}, kJ/mol		ΔS_{app}, J/(mol K)	
MFI samples	IBAS	SBAS	IBAS	SBAS
HZSM5-11.5		74.0		−160.0
HZSM5-11.5-steamed		74.3		−160.0
HZSM5-11.5-water pulsed		74.2		−161.8
HZSM5-15		74.7		−160.0
HZSM5-15-water pulsed		74.0		−162.0
HZSM5-25		80.3		−152.1
NaHZSM5-15	105.2		−152.3	
NaHZSM5-25	105.8		−152.4	
HZSM5-15-AHFS	100.4		−150.9	
HZSM5-40	103.7		−150.2	
HZSM5-140	100.7		−152.5	

3.4.5 Acylation reaction of 2-methylfuran (2-MF) with acetic acid

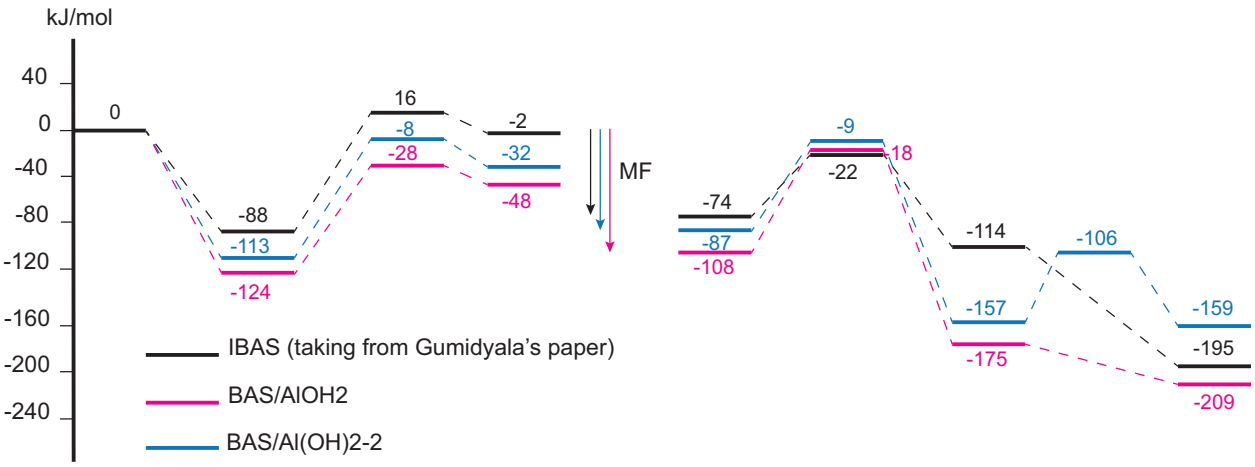


Figure 43. Energy profile of acylation of 2-MF with acetic acid on BAS with the presence of EFAL $Al(OH)_2^+$ in proximity.

In the preceding sections, we discussed the role of EFAL in the alkane cracking reaction. In this section, we will focus on investigating the impact of EFAL on the acylation reaction of 2-MF with acetic acid. The complete mechanism of the acylation reaction is shown in Scheme 4. When EFAL $Al(OH)_2^+$ is present, the mechanism follows the pathway with IBAS, which occurs on two oxygen atoms linked to the same Al atom (as shown in **Scheme 4a**). We analyzed the influence of EFAL $Al(OH)_2^+$ at two different distances from the BAS, which are the BAS/ $Al(OH)_2^+$ site where EFAL $Al(OH)_2^+$ is two Si linking atoms away from the BAS and the BAS/ $Al(OH)_2^+$-2 site where the EFAL is eight Si linking atoms away from the BAS. Initially, acetic acid adsorbs on HZSM-5 by forming hydrogen bond with the BAS. This step has a lower energy on BAS/ $Al(OH)_2^+$ and BAS/ $Al(OH)_2^+$-2, which are 25 and 36 kJ/mol more negative than that of IBAS, respectively. Subsequently, acyl species and water form with a true barriers of 96 and 105 kJ/mol on BAS/ $Al(OH)_2^+$ and BAS/ $Al(OH)_2^+$-2, respectively, which are comparable to the value

of IBAS. However, the apparent activation barriers are 24 and 44 kJ/mol lower than that of IBAS due to the stronger adsorption if the acetic acid molecule. The closer EFAL have stronger impact on the adsorption of acetic acid molecule.

In contrast to the dehydration step the, the subsequent C-C coupling steps have slightly higher apparent activation barriers with the presence of EFAL $Al(OH)_2^+$ at two different distances. The more stable acyl species on synergistic site may make the C-C coupling step more challenging. On the synergistic sites BAS/$Al(OH)_2^+$, the activation barriers of C-C coupling steps and dehydration are comparable, while on BAS/ $Al(OH)_2^+$-2, the activation barrier of C-C coupling is 10 kJ/mol higher than dehydration step. Even though the apparent activation barrier of C-C coupling step on synergistic sites are higher than that of IBAS, they are still lower than the apparent activation barrier of dehydration step on IBAS.

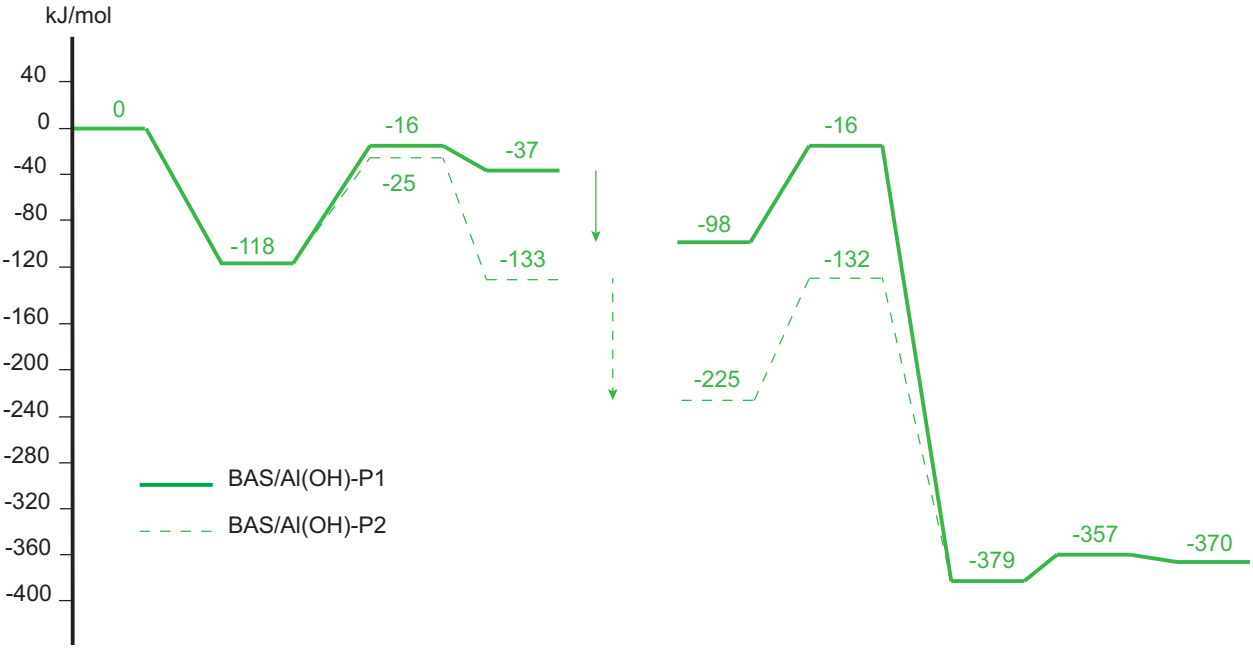
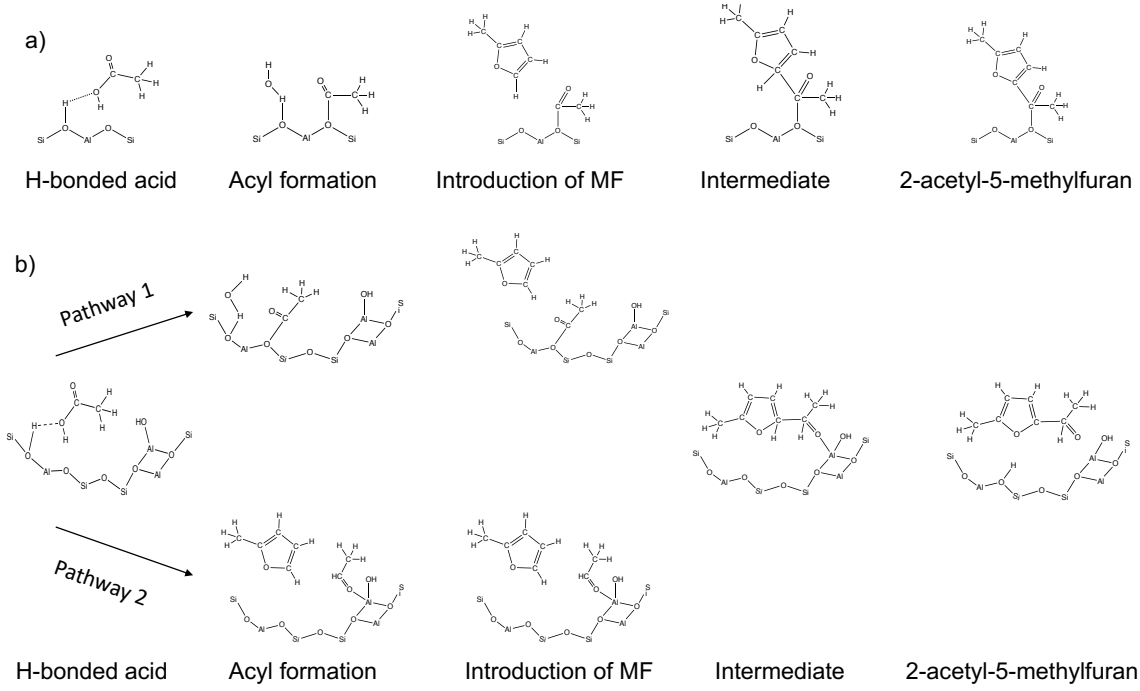


Figure 44. Energy profile of acylation of 2-MF with acetic acid on BAS with the presence of EFAL $Al(OH)^{2+}$ in proximity. The solid line represents reaction pathway 1 and dash line represents reaction pathway 2.

Scheme 4b shows the possible pathways for acylation reaction with the presence of EFAL $Al(OH)^{2+}$ located 2 Si linking atoms away from BAS. Pathway 1 involves a dehydration step similar to that of IBAS, while pathway 2 involves the formation of a bond between the acyl species and EFAL $Al(OH)^{2+}$, which stabilizes the acyl group significantly. In both pathways, the product 2-acetyl-5-methylfuran is bonded with the EFAL $Al(OH)^{2+}$, which reduces the activation energy of the C-C coupling step of pathway 2. Compared to the highest activation barrier of the reaction on IBAS, the activation barriers on BAS/$Al(OH)^{2+}$ are 32 and 41 kJ/mol lower following pathway 1 and pathway 2, respectively.



Scheme 4. Reaction pathways of acylation reaction of 2-Methylfuran with acetic acid a) on IBAS b) on BAS/$Al(OH)^{2+}$ synergistic sites.

3.5 Conclusions

Our investigation has thoroughly examined the influence of various EFAL and PFAL species on the intrinsic acid strength, thermodynamics of adsorption and kinetics of monomolecular propane cracking and dehydrogenation. The DPE values reveal that the synergistic site, in which the BAS proton and EFAL/PFAL form hydrogen bond, have weaker acidity. By contrast, the adjacent EFAL and PFAL species having no direct interaction with the proton do not significantly change the DPE of the proton.

We found that the local environments, where reactions take place, play an important role in catalytic performance of zeolite. The propane cracking reactions show significantly lower intrinsic activation energy, which ranges from 165-181 kJ/mol, among 5 distinct synergistic sites (compared to 189 kJ/mol for isolated BAS sites). The transition states of propane and hexane cracking are more stabilized on synergistic sites due to the electrostatic force between TSs and EFAL/PFAL species. The EFALs and PFAL have more influence on the activation barrier of hexane reaction than propane reaction because of the higher polarizability of hexane molecule. For the propane cracking reaction, the activation entropy is more negative than adsorption entropy. This shows early TS tightly bound to the active sites, and the spaciousness of environment surrounding active sites have less influence on this TS. The decrease of apparent free energies of cracking reactions on synergistic sites is driven by the decrease of apparent activation enthalpies, which further depends on the structures of EFAL and PFAL species in the local environment.

We also found that the activation energies of propane dehydrogenation are not significantly different on synergistic sites relative with IBAS. The charge on TS of hydrogenation is more symmetric and this TS has small dipole moments. Thus, the electrostatic interaction between EFAL/PFAL and TS of propane dehydrogenation reactions on most of active sites do not occur. On synergistic site, the activation entropies of dehydrogenation are more negative than that of

IBAS because of the decrease of confinement. The activation entropy largely determines the activation free energies of propane dehydrogenation. Finally, the trends of apparent activation barriers of the propane in pulse reaction are in line with DFT-results though the activation barriers predicted from DFT are underestimated.

CHAPTER 5: Concluding Remarks and Future Work

5.1 Dissertation summary

In chapter 2, the NMR chemical shift findings demonstrate that the ^{1}H NMR of isolated BAS is responsive to their positions. Specifically, the well-know signal at approximately 4.2 ppm is observed for the BASs at the intersection main channels (straight and sinusoidal channels). Additionally, the 5-7 ppm peak, which is not well understood, was explained as both framework BAS in small confinements and the silanol groups in silanol nests forming during the hydrolysis of framework atoms. Furthermore, the recently identified 11-19 ppm signal, which is associated with non-framework species, is attributed to the BASs that form hydrogen bonds to adjacent EFAL species.

Chapter 3 focuses on the development of mechanisms for the formation of synergistic sites. Specifically, the study shows that BAS/PFAL synergistic sites are generated through partial hydrolysis of BAS site pairs. The formations of these sites are influenced by the density of BAS in the sample and the condition of water treatment. The formation of BAS/EFAL synergistic sites can be driven by the migration of EFAL species along the zeolite framework. Additionally, the study indicates that sodium titration is more energy favorable for synergistic sites than for IBAS. These findings are valuable for the design and analysis of zeolite catalysts in hydrocarbon reactions catalyzed by zeolite.

In chapter 4, we show that the presence of EFAL and PFAL species do not change the intrinsic acid strength of BAS. Using DFT analysis, the study demonstrates that EFAL and PFAL reduce the activation barriers of propane and hexane cracking and dehydrogenation reactions by

stabilizing the TS through dipole-dipole interactions between TSs and EFAL/PFAL. Specifically, the presence of dipole moments in the molecules of TSs with less symmetrical charge distribution enables them to form stronger dipole-dipole interactions with EFAL and PFAL. Conversely, TSs with more symmetrical charge distribution are less affected by EFAL and PFAL.

5.2 Future directions

In future work, we can explore the function of broader extra-lattice species, such as rare earth and phosphorus in zeolite. Phosphorus is a well-known promoter that can enhance the hydrothermal stability of zeolite H-ZSM-5 and interacts with the acid sites of zeolite, resulting in a decrease in the number and strength of acid sites. [99, 100] Although phosphorus can be advantageous in certain reactions, for instance, in the methanol to olefin reaction where it improves selectivity towards light olefins and specifically towards propylene, [101] the exact nature of the interaction between phosphorus and zeolite has always been a topic of debate. Over time, numerous models have been proposed, suggesting possible interactions, and the primary point of contention is whether a permanent interaction between phosphorus and the framework exists or not. [99] [102] By following the method outlined in chapter 2, we can elucidate the nature and interaction of phosphorus species in zeolite by combining computational and experimental NMR chemical shifts. Once the nature of phosphorus species is determined, their role in selectivity and activity can be investigated.

Besides phosphorus species, the inclusion of rare earth elements in zeolite Y mitigates framework dealumination when exposed to hydrothermal conditions, thereby resulting in an increase in activity per unit weight of zeolite and improvement in the rate of hydrogen transfer. [103]

The specific catalytic role and nature of rare earth in alkane cracking can be studied based on the idea of the impact of EFAL on alkane cracking.

References

(1) Król, M. Natural vs. synthetic zeolites. *Crystals* **2020**, *10* (7), 622.

(2) Baerlocher, C.; McCusker, L. B.; Olson, D. H. *Atlas of zeolite framework types*; Elsevier, 2007.

(3) Barrer, R. M. 33. Synthesis of a zeolitic mineral with chabazite-like sorptive properties. *Journal of the Chemical Society (Resumed)* **1948**, 127-132.

(4) Cundy, C. S.; Cox, P. A. The hydrothermal synthesis of zeolites: history and development from the earliest days to the present time. *Chemical reviews* **2003**, *103* (3), 663-702.

(5) Moshoeshoe, M.; Nadiye-Tabbiruka, M. S.; Obuseng, V. A review of the chemistry, structure, properties and applications of zeolites. *Am. J. Mater. Sci* **2017**, *7* (5), 196-221.

(6) Argauer, R. J.; Landolt, G. R. Crystalline zeolite ZSM-5 and method of preparing the same. Google Patents: 1972.

(7) Karwacki, L.; Kox, M. H.; Matthijs de Winter, D.; Drury, M. R.; Meeldijk, J. D.; Stavitski, E.; Schmidt, W.; Mertens, M.; Cubillas, P.; John, N. Morphology-dependent zeolite intergrowth structures leading to distinct internal and outer-surface molecular diffusion barriers. *Nature materials* **2009**, *8* (12), 959-965. Yan, Y.; Davis, M. E.; Gavalas, G. R. Preparation of zeolite ZSM-5 membranes by in-situ crystallization on porous. Alpha.-Al2O3. *Industrial & engineering chemistry research* **1995**, *34* (5), 1652-1661.

(8) Olson, D.; Kokotailo, G.; Lawton, S.; Meier, W. Crystal structure and structure-related properties of ZSM-5. *The Journal of Physical Chemistry* **1981**, *85* (15), 2238-2243.

(9) van der Bij, H. E.; Weckhuysen, B. M. Phosphorus promotion and poisoning in zeolite-based materials: synthesis, characterisation and catalysis. *Chemical Society Reviews* **2015**, *44* (20), 7406-7428.

(10) Dyer, A. An introduction to zeolite molecular sieves. **1988**. Bleken, F.; Skistad, W.; Barbera, K.; Kustova, M.; Bordiga, S.; Beato, P.; Lillerud, K. P.; Svelle, S.; Olsbye, U. Conversion of methanol over 10-ring zeolites with differing volumes at channel intersections: comparison of TNU-9, IM-5, ZSM-11 and ZSM-5. *Physical Chemistry Chemical Physics* **2011**, *13* (7), 2539-2549.

(11) Biligetu, T.; Wang, Y.; Nishitoba, T.; Otomo, R.; Park, S.; Mochizuki, H.; Rondo, J. N.; Tatsumi, T.; Yokoi, T. Al distribution and catalytic performance of ZSM-5 zeolites synthesized with various alcohols. *J Catal* **2017**, *353*, 1-10. DOI: 10.1016/j.jcat.2017.06.026. Dedecek, J.;

Sobalik, Z.; Wichterlova, B. Siting and Distribution of Framework Aluminium Atoms in Silicon-Rich Zeolites and Impact on Catalysis. *Catal Rev* **2012**, *54* (2), 135-223. DOI: 10.1080/01614940.2012.632662. Di Iorio, J. R.; Gounder, R. Controlling the Isolation and Pairing of Aluminum in Chabazite Zeolites Using Mixtures of Organic and Inorganic Structure-Directing Agents. *Chem Mater* **2016**, *28* (7), 2236-2247. DOI: 10.1021/acs.chemmater.6b00181. Yokoi, T.; Mochizuki, H.; Namba, S.; Kondo, J. N.; Tatsumi, T. Control of the Al Distribution in the Framework of ZSM-5 Zeolite and Its Evaluation by Solid-State NMR Technique and Catalytic Properties. *J Phys Chem C* **2015**, *119* (27), 15303-15315. DOI: 10.1021/acs.jpcc.5b03289. Knott, B. C.; Nimlos, C. T.; Robichaud, D. J.; Nimlos, M. R.; Kim, S.; Gounder, R. Consideration of the Aluminum Distribution in Zeolites in Theoretical and Experimental Catalysis Research. *Acs Catal* **2018**, *8* (2), 770-784. DOI: 10.1021/acscatal.7b03676.

(12) Li, C. G.; Vidal-Moya, A.; Miguel, P. J.; Dedecek, J.; Boronat, M.; Corma, A. Selective Introduction of Acid Sites in Different Confined Positions in ZSM-5 and Its Catalytic Implications. *Acs Catal* **2018**, *8* (8), 7688-7697. DOI: 10.1021/acscatal.8b02112.

(13) Noh, G.; Shi, Z. C.; Zones, S. I.; Iglesia, E. Isomerization and beta-scission reactions of alkanes on bifunctional metal acid catalysts: Consequences of confinement and diffusional constraints on reactivity and selectivity. *J Catal* **2018**, *368*, 389-410. DOI: 10.1016/j.jcat.2018.03.033.

(14) Janda, A.; Bell, A. T. Effects of Si/Al Ratio on the Distribution of Framework Al and on the Rates of Alkane Monomolecular Cracking and Dehydrogenation in H-MFI. *J Am Chem Soc* **2013**, *135* (51), 19193-19207. DOI: 10.1021/ja4081937.

(15) Boronat, M.; Martínez, C.; Corma, A. Mechanistic differences between methanol and dimethyl ether carbonylation in side pockets and large channels of mordenite. *Physical Chemistry Chemical Physics* **2011**, *13* (7), 2603-2612.

(16) Boronat, M.; Martinez, C.; Corma, A. Mechanistic differences between methanol and dimethyl ether carbonylation in side pockets and large channels of mordenite. *Phys Chem Chem Phys* **2011**, *13* (7), 2603-2612. DOI: 10.1039/c0cp01996h.

(17) Silaghi, M.-C.; Chizallet, C.; Sauer, J.; Raybaud, P. Dealumination mechanisms of zeolites and extra-framework aluminum confinement. *Journal of Catalysis* **2016**, *339*, 242-255.

(18) Ravi, M.; Sushkevich, V. L.; van Bokhoven, J. A. Towards a better understanding of Lewis acidic aluminium in zeolites. *Nature materials* **2020**, *19* (10), 1047-1056.

(19) Bourgeat-Lami, E.; Massiani, P.; Di Renzo, F.; Espiau, P.; Fajula, F.; Des Courières, T. Study of the state of aluminium in zeolite-β. *Applied catalysis* **1991**, *72* (1), 139-152.
(20) Liu, C.; Li, G. N.; Hensen, E. J. M.; Pidko, E. A. Nature and Catalytic Role of Extraframework Aluminum in Faujasite Zeolite: A Theoretical Perspective. *Acs Catal* **2015**, *5* (11), 7024-7033. DOI: 10.1021/acscatal.5b02268.
(21) Bhering, D. L.; Ramírez-Solís, A.; Mota, C. J. A density functional theory based approach to extraframework aluminum species in zeolites. *The Journal of Physical Chemistry B* **2003**, *107* (18), 4342-4347.
(22) Liu, C.; Li, G.; Hensen, E. J.; Pidko, E. A. Nature and catalytic role of extraframework aluminum in faujasite zeolite: a theoretical perspective. *ACS Catalysis* **2015**, *5* (11), 7024-7033.
(23) Martin, R. M. Electronic structure. *Physik Journal* **2009**, *8* (4), 54.
(24) Resasco, D. E.; Wang, B.; Crossley, S. Zeolite-catalysed C–C bond forming reactions for biomass conversion to fuels and chemicals. *Catalysis Science & Technology* **2016**, *6* (8), 2543-2559. Corma, A. Inorganic solid acids and their use in acid-catalyzed hydrocarbon reactions. *Chemical Reviews* **1995**, *95* (3), 559-614. Huber, G. W.; Iborra, S.; Corma, A. Synthesis of transportation fuels from biomass: chemistry, catalysts, and engineering. *Chemical reviews* **2006**, *106* (9), 4044-4098. Guisnet, M.; Gilson, J.-P. *Zeolites for cleaner technologies*; Imperial College Press London, 2002.
(25) Pham, T. N.; Nguyen, V.; Wang, B.; White, J. L.; Crossley, S. Quantifying the Influence of Water on the Mobility of Aluminum Species and Their Effects on Alkane Cracking in Zeolites. *ACS Catalysis* **2021**, *11* (12), 6982-6994.
(26) Kester, P. M.; Crum, J. T.; Li, S.; Schneider, W. F.; Gounder, R. Effects of Brønsted acid site proximity in chabazite zeolites on OH infrared spectra and protolytic propane cracking kinetics. *Journal of Catalysis* **2021**, *395*, 210-226.
(27) Noh, G.; Shi, Z.; Zones, S. I.; Iglesia, E. Isomerization and β-scission reactions of alkanes on bifunctional metal-acid catalysts: Consequences of confinement and diffusional constraints on reactivity and selectivity. *Journal of Catalysis* **2018**, *368*, 389-410. Li, C.; Vidal-Moya, A.; Miguel, P. J.; Dedecek, J.; Boronat, M.; Corma, A. Selective introduction of acid sites in different confined positions in ZSM-5 and its catalytic implications. *ACS Catalysis* **2018**, *8* (8), 7688-7697.

(28) Abdolrahmani, M.; Chen, K.; White, J. L. Assessment, control, and impact of Brønsted acid site heterogeneity in zeolite HZSM-5. *The Journal of Physical Chemistry C* **2018**, *122* (27), 15520-15528.
(29) Chen, K.; Abdolrhamani, M.; Sheets, E.; Freeman, J.; Ward, G.; White, J. L. Direct detection of multiple acidic proton sites in zeolite HZSM-5. *Journal of the American Chemical Society* **2017**, *139* (51), 18698-18704.
(30) Chen, K.; Abdolrahmani, M.; Horstmeier, S.; Pham, T. N.; Nguyen, V. T.; Zeets, M.; Wang, B.; Crossley, S.; White, J. L. Brønsted–Brønsted synergies between framework and noncrystalline protons in zeolite H-ZSM-5. *ACS Catalysis* **2019**, *9* (7), 6124-6136.
(31) Pham, T. N.; Nguyen, V.; Nguyen-Phu, H.; Wang, B.; Crossley, S. Influence of Brønsted Acid Site Proximity on Alkane Cracking in MFI Zeolites. *ACS Catalysis* **2023**, *13*, 1359-1370.
(32) Zhang, Y.; Zhao, R.; Sanchez-Sanchez, M.; Haller, G. L.; Hu, J.; Bermejo-Deval, R.; Liu, Y.; Lercher, J. A. Promotion of protolytic pentane conversion on H-MFI zeolite by proximity of extra-framework aluminum oxide and Brønsted acid sites. *Journal of Catalysis* **2019**, *370*, 424-433.
(33) Maier, S. M.; Jentys, A.; Lercher, J. A. Steaming of zeolite BEA and its effect on acidity: a comparative NMR and IR spectroscopic study. *The Journal of Physical Chemistry C* **2011**, *115* (16), 8005-8013.
(34) Isernia, L. F. FTIR study of the relation, between extra-framework aluminum species and the adsorbed molecular water, and its effect on the acidity in ZSM-5 steamed zeolite. *Materials Research* **2013**, *16*, 792-802.
(35) Chen, K.; Horstmeier, S.; Nguyen, V. T.; Wang, B.; Crossley, S. P.; Pham, T.; Gan, Z.; Hung, I.; White, J. L. Structure and catalytic characterization of a second framework Al (IV) site in zeolite catalysts revealed by NMR at 35.2 T. *Journal of the American Chemical Society* **2020**, *142* (16), 7514-7523.
(36) Chen, K.; Zornes, A.; Nguyen, V.; Wang, B.; Gan, Z.; Crossley, S. P.; White, J. L. 17O Labeling Reveals Paired Active Sites in Zeolite Catalysts. *Journal of the American Chemical Society* **2022**, *144* (37), 16916-16929.
(37) Mezari, B.; Magusin, P. C.; Almutairi, S. M.; Pidko, E. A.; Hensen, E. J. Nature of enhanced Brønsted acidity induced by extraframework aluminum in an ultrastabilized faujasite zeolite: An in situ NMR study. *The Journal of Physical Chemistry C* **2021**, *125* (17), 9050-9059.

(38) Li, S.; Zheng, A.; Su, Y.; Zhang, H.; Chen, L.; Yang, J.; Ye, C.; Deng, F. Brønsted/Lewis acid synergy in dealuminated HY zeolite: a combined solid-state NMR and theoretical calculation study. *Journal of the American Chemical Society* **2007**, *129* (36), 11161-11171.
(39) Zheng, A.; Li, S.; Liu, S.-B.; Deng, F. Acidic properties and structure–activity correlations of solid acid catalysts revealed by solid-state nmr spectroscopy. *Accounts of chemical research* **2016**, *49* (4), 655-663.
(40) Jiao, J.; Kanellopoulos, J.; Wang, W.; Ray, S. S.; Foerster, H.; Freude, D.; Hunger, M. Characterization of framework and extra-framework aluminum species in non-hydrated zeolites Y by 27 Al spin-echo, high-speed MAS, and MQMAS NMR spectroscopy at B 0= 9.4 to 17.6 T. *Physical Chemistry Chemical Physics* **2005**, *7* (17), 3221-3226.
(41) Chen, K. Z.; Abdolrahmani, M.; Horstmeier, S.; Pham, T. N.; Nguyen, V. T.; Zeets, M.; Wang, B.; Crossley, S.; White, J. L. Bronsted-Bronsted Synergies between Framework and Noncrystalline Protons in Zeolite H-ZSM-5. *Acs Catal* **2019**, *9* (7), 6124-6136. DOI: 10.1021/acscatal.9b01583.
(42) Chen, K.; Gan, Z.; Horstmeier, S.; White, J. L. Distribution of aluminum species in zeolite catalysts: 27Al NMR of framework, partially-coordinated framework, and non-framework moieties. *Journal of the American Chemical Society* **2021**, *143* (17), 6669-6680.
(43) Chen, K. Z.; Horstmeier, S.; Nguyen, V. T.; Wang, B.; Crossley, S. P.; Pham, T.; Gan, Z. H.; Hung, I.; White, J. L. Structure and Catalytic Characterization of a Second Framework Al(IV) Site in Zeolite Catalysts Revealed by NMR at 35.2 T. *J Am Chem Soc* **2020**, *142* (16), 7514-7523. DOI: 10.1021/jacs.0c00590.
(44) Ghorbanpour, A.; Rimer, J. D.; Grabow, L. C. Periodic, vdW-corrected density functional theory investigation of the effect of Al siting in H-ZSM-5 on chemisorption properties and site-specific acidity. *Catalysis Communications* **2014**, *52*, 98-102.
(45) Kresse, G.; Furthmuller, J. Efficient iterative schemes for ab initio total-energy calculations using a plane-wave basis set. *Phys Rev B* **1996**, *54* (16), 11169-11186. DOI: DOI 10.1103/PhysRevB.54.11169.
(46) Perdew, J. P.; Burke, K.; Ernzerhof, M. Generalized gradient approximation made simple. *Phys Rev Lett* **1996**, *77* (18), 3865-3868. DOI: DOI 10.1103/PhysRevLett.77.3865.

(47) Grimme, S.; Antony, J.; Ehrlich, S.; Krieg, H. A consistent and accurate ab initio parametrization of density functional dispersion correction (DFT-D) for the 94 elements H-Pu. *J Chem Phys* **2010**, *132* (15), 154104. DOI: Doi 10.1063/1.3382344.
(48) Zeets, M.; Resasco, D. E.; Wang, B. Enhanced chemical activity and wettability at adjacent Brønsted acid sites in HZSM-5. *Catalysis Today* **2018**, *312*, 44-50.
(49) Watermann, T.; Scherrer, A.; Sebastiani, D. Linear response methods in quantum chemistry. *Many-Electron Approaches in Physics, Chemistry and Mathematics: A Multidisciplinary View* **2014**, 97-110.
(50) Wouters, B. H.; Chen, T.; Grobet, P. J. Steaming of zeolite Y: Formation of transient Al species. *The Journal of Physical Chemistry B* **2001**, *105* (6), 1135-1139.
(51) Li, S.; Zheng, A.; Su, Y.; Fang, H.; Shen, W.; Yu, Z.; Chen, L.; Deng, F. Extra-framework aluminium species in hydrated faujasite zeolite as investigated by two-dimensional solid-state NMR spectroscopy and theoretical calculations. *Physical Chemistry Chemical Physics* **2010**, *12* (15), 3895-3903.
(52) Nimlos, C. T.; Hoffman, A. J.; Hur, Y. G.; Lee, B. J.; Di Iorio, J. R.; Hibbitts, D. D.; Gounder, R. Experimental and theoretical assessments of aluminum proximity in MFI zeolites and its alteration by organic and inorganic structure-directing agents. *Chemistry of Materials* **2020**, *32* (21), 9277-9298.
(53) Xin, S.; Wang, Q.; Xu, J.; Chu, Y.; Wang, P.; Feng, N.; Qi, G.; Trébosc, J.; Lafon, O.; Fan, W. The acidic nature of "NMR-invisible" tri-coordinated framework aluminum species in zeolites. *Chemical science* **2019**, *10* (43), 10159-10169.
(54) Zheng, A.; Huang, S.-J.; Chen, W.-H.; Wu, P.-H.; Zhang, H.; Lee, H.-K.; de Ménorval, L.-C.; Deng, F.; Liu, S.-B. 31P chemical shift of adsorbed trialkylphosphine oxides for acidity characterization of solid acids catalysts. *The Journal of Physical Chemistry A* **2008**, *112* (32), 7349-7356. Wiper, P. V.; Amelse, J.; Mafra, L. Multinuclear solid-state NMR characterization of the Brønsted/Lewis acid properties in the BP HAMS-1B (H-[B]-ZSM-5) borosilicate molecular sieve using adsorbed TMPO and TBPO probe molecules. *Journal of catalysis* **2014**, *316*, 240-250.
(55) Dimitrijevic, R.; Lutz, W.; Ritzmann, A. Hydrothermal stability of zeolites: Determination of extra-framework species of HY faujasite-type steamed zeolite. *Journal of Physics and Chemistry of Solids* **2006**, *67* (8), 1741-1748.

(56) Ravi, M.; Sushkevich, V. L.; van Bokhoven, J. A. On the location of Lewis acidic aluminum in zeolite mordenite and the role of framework-associated aluminum in mediating the switch between Brønsted and Lewis acidity. *Chemical science* **2021**, *12* (11), 4094-4103.
(57) Van Donk, S.; Janssen, A. H.; Bitter, J. H.; de Jong, K. P. Generation, characterization, and impact of mesopores in zeolite catalysts. *Catalysis Reviews* **2003**, *45* (2), 297-319.
(58) Silaghi, M.-C.; Chizallet, C.; Raybaud, P. Challenges on molecular aspects of dealumination and desilication of zeolites. *Microporous and Mesoporous Materials* **2014**, *191*, 82-96.
(59) Dedecek, J.; Sklenak, S.; Li, C.; Wichterlová, B.; Gábová, V.; Brus, J. i.; Sierka, M.; Sauer, J. Effect of Al− Si− Al and Al− Si− Si− Al pairs in the ZSM-5 zeolite framework on the 27Al NMR spectra. A combined high-resolution 27Al NMR and DFT/MM study. *The Journal of Physical Chemistry C* **2009**, *113* (4), 1447-1458. Bordiga, S.; Ugliengo, P.; Damin, A.; Lamberti, C.; Spoto, G.; Zecchina, A.; Spano, G.; Buzzoni, R.; Dalloro, L.; Rivetti, F. Hydroxyls nests in defective silicalites and strained structures derived upon dehydroxylation: vibrational properties and theoretical modelling. *Topics in Catalysis* **2001**, *15*, 43-52.
(60) Müller, M.; Harvey, G.; Prins, R. Comparison of the dealumination of zeolites beta, mordenite, ZSM-5 and ferrierite by thermal treatment, leaching with oxalic acid and treatment with SiCl4 by 1H, 29Si and 27Al MAS NMR. *Microporous and mesoporous materials* **2000**, *34* (2), 135-147.
(61) Van Geem, P.; Scholle, K.; Van der Velden, G.; Veeman, W. Study of the transformation of small-port into large-port mordenite by magic-angle spinning NMR and infrared spectroscopy. *The Journal of Physical Chemistry* **1988**, *92* (6), 1585-1589.
(62) Agostini, G.; Lamberti, C.; Palin, L.; Milanesio, M.; Danilina, N.; Xu, B.; Janousch, M.; Van Bokhoven, J. A. In situ XAS and XRPD parametric Rietveld refinement to understand dealumination of Y zeolite catalyst. *Journal of the American Chemical Society* **2010**, *132* (2), 667-678.
(63) Ásgeirsson, V.; Birgisson, B. O.; Bjornsson, R.; Becker, U.; Neese, F.; Riplinger, C.; Jónsson, H. Nudged elastic band method for molecular reactions using energy-weighted springs combined with eigenvector following. *Journal of chemical theory and computation* **2021**, *17* (8), 4929-4945.
(64) Mills, G.; Jónsson, H.; Schenter, G. K. Reversible work transition state theory: application to dissociative adsorption of hydrogen. *Surface Science* **1995**, *324* (2-3), 305-337. Jónsson, H.; Mills, G.; Jacobsen, K. W. Nudged elastic band method for finding minimum energy paths of transitions.

In *Classical and quantum dynamics in condensed phase simulations*, World Scientific, 1998; pp 385-404.
(65) Henkelman, G.; Jónsson, H. Improved tangent estimate in the nudged elastic band method for finding minimum energy paths and saddle points. *The Journal of chemical physics* **2000**, *113* (22), 9978-9985.
(66) Henkelman, G.; Uberuaga, B. P.; Jónsson, H. A climbing image nudged elastic band method for finding saddle points and minimum energy paths. *The Journal of chemical physics* **2000**, *113* (22), 9901-9904.
(67) Ásgeirsson, V.; Jónsson, H. Exploring potential energy surfaces with saddle point searches. *Handbook of Materials Modeling: Methods: Theory and Modeling* **2020**, 689-714.
(68) Henkelman, G.; Jónsson, H. A dimer method for finding saddle points on high dimensional potential surfaces using only first derivatives. *The Journal of chemical physics* **1999**, *111* (15), 7010-7022.
(69) Voter, A. F. Hyperdynamics: Accelerated molecular dynamics of infrequent events. *Physical Review Letters* **1997**, *78* (20), 3908.
(70) Wiberg, K. B. Ab Initio Molecular Orbital Theory by WJ Hehre, L. Radom, P. v. R. Schleyer, and JA Pople, John Wiley, New York, 548pp. Price: $79.95 (1986). Wiley Online Library: 1986.
(71) Cramer, C. J. *Essentials of computational chemistry: theories and models*; John Wiley & Sons, 2013.
(72) Piccini, G.; Alessio, M.; Sauer, J. Ab initio study of methanol and ethanol adsorption on Brønsted sites in zeolite H-MFI. *Physical Chemistry Chemical Physics* **2018**, *20* (30), 19964-19970. Piccini, G.; Alessio, M.; Sauer, J.; Zhi, Y.; Liu, Y.; Kolvenbach, R.; Jentys, A.; Lercher, J. A. Accurate adsorption thermodynamics of small alkanes in zeolites. Ab initio theory and experiment for H-chabazite. *The Journal of Physical Chemistry C* **2015**, *119* (11), 6128-6137. Li, Y.-P.; Bell, A. T.; Head-Gordon, M. Thermodynamics of anharmonic systems: Uncoupled mode approximations for molecules. *Journal of chemical theory and computation* **2016**, *12* (6), 2861-2870. Piccini, G.; Sauer, J. Quantum chemical free energies: Structure optimization and vibrational frequencies in normal modes. *Journal of chemical theory and computation* **2013**, *9* (11), 5038-5045. Piccini, G.; Sauer, J. Effect of anharmonicity on adsorption thermodynamics. *Journal of chemical theory and computation* **2014**, *10* (6), 2479-2487.

(73) Grimme, S. Supramolecular binding thermodynamics by dispersion-corrected density functional theory. *Chemistry–A European Journal* **2012**, *18* (32), 9955-9964.
(74) Chai, J.-D.; Head-Gordon, M. Long-range corrected hybrid density functionals with damped atom–atom dispersion corrections. *Physical Chemistry Chemical Physics* **2008**, *10* (44), 6615-6620.
(75) Li, Y.-P.; Gomes, J.; Mallikarjun Sharada, S.; Bell, A. T.; Head-Gordon, M. Improved force-field parameters for QM/MM simulations of the energies of adsorption for molecules in zeolites and a free rotor correction to the rigid rotor harmonic oscillator model for adsorption enthalpies. *The Journal of Physical Chemistry C* **2015**, *119* (4), 1840-1850.
(76) Maxwell, I. Zeolite catalysis in hydroprocessing technology. *Catalysis Today* **1987**, *1* (4), 385-413. Vogt, E. T.; Weckhuysen, B. M. Fluid catalytic cracking: recent developments on the grand old lady of zeolite catalysis. *Chemical Society Reviews* **2015**, *44* (20), 7342-7370. Zheng, S.; Jentys, A.; Lercher, J. A. Xylene isomerization with surface-modified HZSM-5 zeolite catalysts: An in situ IR study. *Journal of Catalysis* **2006**, *241* (2), 304-311.
(77) Ong, L. H.; Dömök, M.; Olindo, R.; van Veen, A. C.; Lercher, J. A. Dealumination of HZSM-5 via steam-treatment. *Microporous and Mesoporous Materials* **2012**, *164*, 9-20. Janssen, A. H.; Koster, A. J.; de Jong, K. P. Three-dimensional transmission electron microscopic observations of mesopores in dealuminated zeolite Y. *Angewandte Chemie International Edition* **2001**, *40* (6), 1102-1104. Zhao, R.; Khare, R.; Zhang, Y.; Sanchez-Sanchez, M.; Bermejo-Deval, R.; Liu, Y.; Lercher, J. A. Promotion of adsorptive and catalytic properties of zeolitic Brønsted acid sites by proximal extra-framework Si (OH) x groups. *Nature Catalysis* **2023**, *6* (1), 68-79.
(78) Xue, N.; Vjunov, A.; Schallmoser, S.; Fulton, J. L.; Sanchez-Sanchez, M.; Hu, J. Z.; Mei, D.; Lercher, J. A. Hydrolysis of zeolite framework aluminum and its impact on acid catalyzed alkane reactions. *Journal of Catalysis* **2018**, *365*, 359-366.
(79) Li, S.; Huang, S.-J.; Shen, W.; Zhang, H.; Fang, H.; Zheng, A.; Liu, S.-B.; Deng, F. Probing the spatial proximities among acid sites in dealuminated HY zeolite by solid-state NMR spectroscopy. *The Journal of Physical Chemistry C* **2008**, *112* (37), 14486-14494.
(80) Schallmoser, S.; Ikuno, T.; Wagenhofer, M.; Kolvenbach, R.; Haller, G.; Sanchez-Sanchez, M.; Lercher, J. Impact of the local environment of Brønsted acid sites in ZSM-5 on the catalytic activity in n-pentane cracking. *Journal of catalysis* **2014**, *316*, 93-102. Chu, Y.; Yi, X.; Li, C.; Sun,

X.; Zheng, A. Brønsted/Lewis acid sites synergistically promote the initial C–C bond formation in the MTO reaction. *Chemical science* **2018**, *9* (31), 6470-6479.
(81) Kresse, G.; Furthmüller, J. Efficient iterative schemes for ab initio total-energy calculations using a plane-wave basis set. *Physical review B* **1996**, *54* (16), 11169.
(82) Perdew, J. P.; Burke, K.; Ernzerhof, M. Generalized gradient approximation made simple. *Physical review letters* **1996**, *77* (18), 3865.
(83) Kresse, G.; Joubert, D. From ultrasoft pseudopotentials to the projector augmented-wave method. *Physical review b* **1999**, *59* (3), 1758. Blöchl, P. E. Projector augmented-wave method. *Physical review B* **1994**, *50* (24), 17953.
(84) Grimme, S.; Antony, J.; Ehrlich, S.; Krieg, H. A consistent and accurate ab initio parametrization of density functional dispersion correction (DFT-D) for the 94 elements H-Pu. *The Journal of chemical physics* **2010**, *132* (15), 154104.
(85) Bader, R. F. A quantum theory of molecular structure and its applications. *Chemical Reviews* **1991**, *91* (5), 893-928.
(86) Tang, W.; Sanville, E.; Henkelman, G. A grid-based Bader analysis algorithm without lattice bias. *Journal of Physics: Condensed Matter* **2009**, *21* (8), 084204.
(87) M. J. Frisch, G. W. T., H. B. Schlegel, G. E. Scuseria, ; M. A. Robb, J. R. C., G. Scalmani, V. Barone, B. Mennucci, ; G. A. Petersson, H. N., M. Caricato, X. Li, H. P. Hratchian, ; A. F. Izmaylov, J. B., G. Zheng, J. L. Sonnenberg, M. Hada, ; M. Ehara, K. T., R. Fukuda, J. Hasegawa, M. Ishida, T. Nakajima, ; Y. Honda, O. K., H. Nakai, T. Vreven, J. A. Montgomery, Jr., ; J. E. Peralta, F. O., M. Bearpark, J. J. Heyd, E. Brothers, ; K. N. Kudin, V. N. S., T. Keith, R. Kobayashi, J. Normand, ; K. Raghavachari, A. R., J. C. Burant, S. S. Iyengar, J. Tomasi, ; M. Cossi, N. R., J. M. Millam, M. Klene, J. E. Knox, J. B. Cross, ; et al. Gaussian 09, Revision B. 01, Gaussian. *Inc., Wallingford CT* **2010**.
(88) Stephens, P. J.; Devlin, F. J.; Chabalowski, C. F.; Frisch, M. J. Ab initio calculation of vibrational absorption and circular dichroism spectra using density functional force fields. *The Journal of physical chemistry* **1994**, *98* (45), 11623-11627.
(89) Jones, A. J.; Iglesia, E. The strength of Brønsted acid sites in microporous aluminosilicates. *Acs Catalysis* **2015**, *5* (10), 5741-5755.
(90) De Moor, B. A.; Reyniers, M.-F. o.; Gobin, O. C.; Lercher, J. A.; Marin, G. B. Adsorption of C2− C8 n-Alkanes in Zeolites. *The Journal of Physical Chemistry C* **2011**, *115* (4), 1204-1219.

(91) Gounder, R.; Iglesia, E. The roles of entropy and enthalpy in stabilizing ion-pairs at transition states in zeolite acid catalysis. *Accounts of chemical research* **2012**, *45* (2), 229-238.
(92) Narbeshuber, T. F.; Vinek, H.; Lercher, J. A. Monomolecular conversion of light alkanes over H-ZSM-5. *Journal of Catalysis* **1995**, *157* (2), 388-395.
(93) Mallikarjun Sharada, S.; Zimmerman, P. M.; Bell, A. T.; Head-Gordon, M. Insights into the kinetics of cracking and dehydrogenation reactions of light alkanes in H-MFI. *The Journal of Physical Chemistry C* **2013**, *117* (24), 12600-12611.
(94) Swisher, J. A.; Hansen, N.; Maesen, T.; Keil, F. J.; Smit, B.; Bell, A. T. Theoretical simulation of n-alkane cracking on zeolites. *The Journal of Physical Chemistry C* **2010**, *114* (22), 10229-10239.
(95) Dauenhauer, P. J.; Abdelrahman, O. A. A universal descriptor for the entropy of adsorbed molecules in confined spaces. *ACS central science* **2018**, *4* (9), 1235-1243.
(96) Bučko, T.; Benco, L.; Dubay, O.; Dellago, C.; Hafner, J. Mechanism of alkane dehydrogenation catalyzed by acidic zeolites: Ab initio transition path sampling. *The Journal of chemical physics* **2009**, *131* (21), 214508.
(97) Xu, B.; Sievers, C.; Hong, S. B.; Prins, R.; van Bokhoven, J. A. Catalytic activity of Brønsted acid sites in zeolites: Intrinsic activity, rate-limiting step, and influence of the local structure of the acid sites. *Journal of Catalysis* **2006**, *244* (2), 163-168.
(98) Babitz, S.; Williams, B.; Miller, J.; Snurr, R.; Haag, W.; Kung, H. Monomolecular cracking of n-hexane on Y, MOR, and ZSM-5 zeolites. *Applied Catalysis A: General* **1999**, *179* (1-2), 71-86.
(99) Blasco, T.; Corma, A.; Martínez-Triguero, J. Hydrothermal stabilization of ZSM-5 catalytic-cracking additives by phosphorus addition. *Journal of catalysis* **2006**, *237* (2), 267-277.
(100) Caeiro, G.; Magnoux, P.; Lopes, J.; Ribeiro, F. R.; Menezes, S.; Costa, A.; Cerqueira, H. Stabilization effect of phosphorus on steamed H-MFI zeolites. *Applied Catalysis A: General* **2006**, *314* (2), 160-171. Lercher, J.; Rumplmayr, G. Controlled decrease of acid strength by orthophosphoric acid on ZSM5. *Applied catalysis* **1986**, *25* (1-2), 215-222.
(101) Liu, J.; Zhang, C.; Shen, Z.; Hua, W.; Tang, Y.; Shen, W.; Yue, Y.; Xu, H. Methanol to propylene: Effect of phosphorus on a high silica HZSM-5 catalyst. *Catalysis Communications* **2009**, *10* (11), 1506-1509.

(102) Lischke, G.; Eckelt, R.; Jerschkewitz, H.-G.; Parlitz, B.; Schreier, E.; Storek, W.; Zibrowius, B.; Öhlmann, G. Spectroscopic and physicochemical characterization of P-modified H-ZSM-5. *Journal of catalysis* **1991**, *132* (1), 229-243. Cardoso, M. J. B.; Rosas, D. D. O.; Lau, L. Y. Surface P and Al distribution in P-modified ZSM-5 zeolites. *Adsorption* **2005**, *11* (5-6), 577-580. Kaeding, W. W.; Butter, S. A. Production of chemicals from methanol: I. Low molecular weight olefins. *Journal of Catalysis* **1980**, *61* (1), 155-164. Jentys, A.; Rumplmayr, G.; Lercher, J. A. Hydroxyl groups in phosphorus-modified HZSM-5. *Applied catalysis* **1989**, *53* (2-3), 299-312. Damodaran, K.; Wiench, J.; de Menezes, S. C.; Lam, Y.; Trebosc, J.; Amoureux, J.-P.; Pruski, M. Modification of H-ZSM-5 zeolites with phosphorus. 2. Interaction between phosphorus and aluminum studied by solid-state NMR spectroscopy. *Microporous and mesoporous materials* **2006**, *95* (1-3), 296-305. Caro, J.; Bülow, M.; Derewinski, M.; Haber, J.; Hunger, M.; Kärger, J.; Pfeifer, H.; Storek, W.; Zibrowius, B. NMR and IR studies of zeolite H-ZSM-5 modified with orthophosphoric acid. *Journal of Catalysis* **1990**, *124* (2), 367-375.

(103) Woltermann, G. M.; Magee, J. S.; Griffith, S. D. Commercial preparation and characterization of FCC catalysts. In *Studies in Surface Science and Catalysis*, Vol. 76; Elsevier, 1993; pp 105-144.